PARAMETRIC MODELLING
AND STRUCTURAL ANALYSIS
OF THE BATUMI AQUARIUM

Authors:
s061943 Jens Hjorth
s061951 Lars Olesen

Supervisors:
Henrik Almegaard
Jan Karlshøj

**Technical University
of Denmark**

DTU

Preface

This project is a M.Sc. thesis of 30 ECTS points written in the period of February 13th to July 27th 2012. A M.Sc. thesis is a compulsory project in order to fulfil the requirements for the M.Sc. programme in Civil Engineering and Architectural Engineering at the Technical University of Denmark.

Associate Professors Henrik Almegaard and Jan Karlshøj have been the principal supervisors.

<div style="display:flex; justify-content: space-between;">

Jens Hjorth
s061943

Lars Olesen
s061951

</div>

Kongens Lyngby, July 2012

Acknowledgements

First of all we would like to thank our supervisors Associate Professors Henrik Almegaard and Jan Karlshøj for the weekly meetings and for their guidance and encouragement throughout the project.

A special thanks to Jaap Aanhaanen from Buro Happold (now Rambøll) for introducing us to the project and for providing us with necessary data and guidance when needed. The feedback and inputs from Jaap have been of great value.
We would also like to thank Frank Schwartz from Buro Happold for putting us in contact with Jaap.

Furthermore we would like to thank Professor Per Goltermann for his assistance in regards to the reinforced concrete calculations carried out in this project.

Last, but not least, a big thank you to our families and friends for support and encouragement.

Abstract

This thesis deals with the dimensioning and structural optimisation of pebble B in the Batumi Aquarium designed by Henning Larsen Architects and Buro Happold.

By the use of a parametric model the project will optimise the geometry of pebble B based on qualitative studies of selected shell structures and geometric analyses of the proposed geometry. From the studies it is concluded that planar and concave areas on a shell geometry are unfavourable from a structural point of view.

The original and optimised geometry will be dimensioned through linear and non-linear finite element analyses whereby the optimisation is evaluated in terms of the material consumption of the two geometries. The non-linear deflection is seen to be the dimensioning factor for both structures and the optimised structure proves to reduce the material consumption by 35,4% and 44,6% for concrete and reinforcement steel respectively.

As a preliminary investigation parametric visualisation tools are developed to assist an intuitive understanding of stresses and section forces in shell structures. Furthermore, a cross section dimensioning tool for applying reinforced concrete cross sections, of sufficient strength, to shell structures is developed.

Two conceptual proposals for a secondary structure to support the upper pebble in the Batumi Aquarium are presented, analysed and dimensioned. A secondary structure not consisting of columns proves to be an unsuitable solution.

Finally, a qualitative study of the influence of ring loads on shell structures is conducted. From the observations made, two alternative proposals to the geometry of pebble B is presented. The two geometries are developed to support the upper pebble more efficiently than the original geometry. The ring load study concludes that the angle between the applied ring load and the shell geometry highly influences the sizes of the local bending moments.

Resumé

Dette kandidatprojekt omhandler dimensionering og statisk optimering af sektion B i Batumi Akvariet designet af Henning Larsen Architects og Buro Happold.

Projektet vil via en parametrisk model af sektion B optimere geometrien på baggrund af kvalitative undersøgelser af udvalgte skalkonstruktioner, samt geometriske analyser af udformningen af sektion B foreslået af Henning Larsen Architects. Fra undersøgelserne konkluderes det, at plane og konkave områder på en skalkonstruktion er uhensigtsmæssige i et konstruktivt perspektiv.

Gennem lineære og ikke-lineære elementmetodeberegninger vil den originale geometri samt en optimeret geometri blive dimensioneret, hvorefter optimeringsprocessen evalueres ud fra en sammenligning af materialeforbruget for de to konstruktioner. For begge geometrier er de ikke-lineære deformationer dimensionerende, og det viser sig at den optimerede geometri opnår en besparelse i materialer på 35,4% og 44,6% for henholdsvis beton og armeringsstål i forhold til den originale geometri. Begge geometrier dimensioneres som skalkonstruktioner udført i armeret beton.

Som en forundersøgelse til den statiske analyse vil visuelle parametriske værktøjer til illustration og intuitiv forståelse af spændinger og snitkræfter i skalkonstruktioner blive udviklet. Ligeledes vil et lineært dimensioneringsværktøj for skalkonstruktioner i armeret beton blive præsenteret.

Yderligere vil to konceptuelle udformninger af en sekundær konstruktion, til optagelse af en stor vertikal last fra en overliggende bygningsdel, sektion A, blive dimensioneret. Det viser sig uhensigtsmæssigt at udføre de sekundære konstruktioner uden brug af søjler.

Endeligt udføres et kvalitativt studie af cirkulære linie- og fladelasters påvirkning af skalkonstruktioner, og to udformninger af sektion B foreslås til optagelse af en sådan last. Undersøgelsen konkluderer, at angrebsvinklen mellem last og skalkonstruktion er af afgørende betydning for størrelsen af de bøjende momenter i skallen for en sådan lokal påvirkning.

Contents

CHAPTER 1

Introduction

1.1 Background

1.1.1 Parametric Modelling

The initial design of an architectural model is often created with modern modelling tools where advanced capabilities allow the architect to work with complex free-form shapes that have been almost impossible to achieve previously. These models require adjustments in order to cope with structural, functional, aesthetic or cost requirements - adjustments that can result in manual rework. However, these changes can also be facilitated by a parametric modelling approach where design parameters and constraints are used to determine a range of design variations.

Parametric modelling is a generic editing approach where related parameters generate the form automatically through algorithms. There is no clear definition of parametric modelling and especially the degree of parameterisation is a subject of discussion. A fully parametric building model for instance should incorporate all aspects such as: Overall geometry, structural system, installations and include restrictions such as energy considerations, structural behaviour and more. Defining the necessary constraints for a fully parametric model is a complex task and requires a complete overview of the design process.

A parametric approach targeting the interoperability of 3D modelling tools and finite element analysis (FEA) software has great advantages when designing a structural system. A parametric variation of the structural model is exported to the FEA software in order to perform a structural analysis where loads, boundary conditions and cross sections are applied automatically. From a structural engineering point of view this fully automated link will speed up the structural analysis when parametric changes in the model is to be analysed.

In large-scale or complex projects both the architectural and structural model will go through many design variation before converging on a final design. A parametric approach facilitates this optimisation process and offers the possibility to analyse variations in the design with a high degree of detail and precision.

1.1.2   Shell Structures

Under appropriate conditions shell structures have structural advantages due to the fact that loads are carried as in-plane forces. The efficiency of shell structures is defined by curvature and thickness. If bending moments are minimised a shell structure has a high strength-to-weight ratio allowing the shell structure to obtain a very large span. Pier Luigi Nervi and Santiago Calatrava are some of the best examples of building designers who have utilised the advantages of thin shell structures (figure 1.1). The curvature of the shell structure does not only create a spatial stiffness it also has a very high aesthetic value. Combining the curvature of the shell structure with a structural material as reinforced concrete enables curved, continuous and smooth surfaces.

Figure 1.1: Auditorio de Tenerife, Canary Islands, Spain - Santiago Calatrava.[21].

A qualitative study of small shell structures is a well-documented, by Henrik Almegaard [8], approach in order to understand the effect of curvature, boundary and load conditions. Both physical paper models and parametric models can be used in the qualitative studies.

1.1.3   The Batumi Aquarium

Henning Larsen Architects have designed the new aquarium in the seaport of Batumi, Georgia. The 2.000 m^2 aquarium has the characteristics of pebbles from the Batumi beach, which create a significant expression inspired by nature. The formation constitutes five long span self-supporting structures of complex geometric shape which will support the upper pebble. The Batumi Aquarium is intended to become a modern, cultural aquarium for visitors but will also stand out as a landmark for the Batumi area.
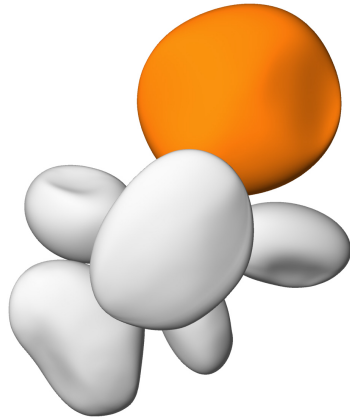
(a) The Batumi Aquarium by Henning Larsen Architects.   (b) Formation of pebbles.

Figure 1.2: The characteristic of pebbles for The Batumi Aquarium.

The formation and the complex shapes necessitate a challenging structural system of The Batumi Aquarium. The highly-sculptural surfaces all contain convex, concave and planar areas which makes it impossible to achieve in-plane forces only. Hence, bending moments will cause an increased thickness of the structure. The support for the upper pebble should contain no vertical columns and preferably not be visible at the interior surface of the lower pebbles. These restrictions regarding a secondary structure complicates an appropriate structural solution for the support of the upper pebble.

All the pebbles have similar characteristics. However, the largest pebble, referred to as pebble B, is the most complex of the lower pebbles. With an overall span 30 - 40 meters and a height of 16,5 meter makes it nearly twice the size as the second largest pebble.

1.2 Problem Statement

Based on the information presented in the introduction the parametric modelling approach is ideal for structural analysis purposes regarding complex shell structures.
The behaviour of complex shell structures can be hard to predict analytically and a parametric modelling approach offers an alternative to the traditional analytical approach by facilitating automated analysis setups for numerous investigations of varied geometries.
The main goal of this thesis is to structurally optimise the reinforced concrete shell structure of pebble B of the Batumi Aquarium through geometric changes. Addressing the following questions approaches this goal:

1. How does geometric changes affect a shell structure?

   (a) How can the parametric approach be utilised in a preliminary study of shell structures?

2. How can the geometry of pebble B be structurally optimised in continuation of the observations made in the preliminary study and what are the benefits of such an optimisation?

3. How can the upper pebble in the Batumi Aquarium be supported by pebble B?

    (a) What are the consequences and how can they be minimised?

1.3   Software Description

This section will briefly introduce the programs used in the work behind this report. This includes the 3D modelling program Rhinoceros and the parametric modelling plug-in Grasshopper. Autodesk Robot, Sofistik, Geometry Gym and Scan&Solve have been used for structural analysis purposes.

Rhinoceros

Rhinoceros[1](Rhino) is a free-form 3D modelling tool mainly used by architects and industrial designers. Especially the use of non-uniform rational b-splines also referred to as NURBS curves makes Rhino a preferred choice for intuitive free-from modelling. The extensive amount of tutorials, blogs, and free compendiums available online along with the relatively cheap licenses makes Rhino a very popular tool.

Rhino does not natively interoperate with any other BIM software but does offer the possibility of saving 3D models in about 30 different file formats including *.sat* for an indirect link to Autodesk Building Design Suite.

One of the most significant advantages of Rhino is the possibility of using the numerous third party plug-ins available online. Plug-ins[1] such as Grasshopper, Kangaroo and Galapagos are just some of the very effective and free plug-ins that intuitively optimise the free-form modelling in Rhino especially in regards to further investigation from an engineer's point of view.

Grasshopper

Grasshopper[2](GH) is a free plug-in for Rhino that makes generative modelling a possibility directly in the Rhino interface. The parameterisation of the Rhino models makes the alteration of geometries a lot faster to implement than the possibilities already offered directly in Rhino.

Unlike other generative design software such as Generative Components, GH does not require any knowledge of programming or scripting. It does offer the possibility of scripting through Visual Basic but the number of native commands available fits even the most complex demands of geometry modelling.

Again the amount of training material available online combined with the extremely intuitive interface makes the learning curve of GH very steep.

Geometry Gym

Geometry Gym[3](GG) is a plug-in for GH developed by the australian Jon Mirtschin. Among the tools offered is *StructDrawRhino* which applies structural properties to parametric geometries made in GH. User-defined or standardised section properties are applied and modelled in Rhino which improves the productivity and makes Rhino models more suitable for further structural investigations.

For this report however, the most interesting tools offered by GG are the *Smart Structural Interpreters* (SSIs) that work as direct links between GH and numerous FEA programs including Autodesk Robot, SAP2000, SOFiSTiK, Ansys and more. Some of the SSIs are more thoroughly developed than others but all include the possibility of exporting geometries directly from GH to the FEA interface of the given software. Some SSIs even include the direct transferring of loads, supports and section properties but it should be mentioned that while the SSIs do speed up the workflow of Rhino-to-FEA geometry exchange the SSIs lack stability and consistency[1].

Autodesk Robot Structural Analysis Professional

Autodesk Robot Structural Analysis Professional[4](Robot) is one of the most commonly used FEA programs available. The interoperability with other Autodesk softwares such as AutoCad and Revit Structure makes it an obvious choice in a BIM context.

Reinforced concrete and steel design solutions, along with the use of international design codes including Eurocodes and a wide extent of graphically shown results, are just some of the reasons why Robot is a widely used FEA software.

SOFiSTiK Structural Desktop

SOFiSTiK Structural Desktop (Sofistik) is a high performance software solution for civil and structural engineering. With a wide range of interfaces a direct link between modelling, meshing and further calculation steps, without having to manually convert data between different programs, has been made possible. The interoperability with Cad-software such as: AutoCad, Revit Structure and Rhinoceros enables unique modelling options. Furthermore, Sofistik contains a very powerful scripting language which provides the engineer the possibility to create macros for load or analysis tasks, which is very useful when repeating the analysis of a complex structural system.

Scan&Solve

Scan&Solve[5](SnS) is a plug-in for Rhino developed by Intact Solutions which enables a FEA working directly in the Rhino interface performing structural analyses from solid Rhino geometries. The intuitive and fast implementation of the structural behaviour of solid geometries cannot be questioned and as it will be investigated later in this report SnS is not that far off from the results found from more used and generally recognised FEA software such as Autodesk Robot and Sofistik.

---

[1]At this stage the plug-ins will cause both Rhino, GH and the FEA software to crash every now and then but this should be fixed through further development in the future according to Jon Mirtschin.

1.4   Process and Workflow

The evolution of computers and FEA software makes complex structural analyses less complicated and reduces the manual calculations. This change forces structural engineers to develop computational skills involving both modelling and analytic procedures for numerous programs. Furthermore, the verification and understanding of the analytic results is to a large degree the main objective for structural engineers today. A combination of parametric modelling and structural analysis does not only facilitate the optimisation process by a range of design variations it also has some advantages in regards to the understanding of analytic results. This section seeks to clarify the overall process and the interoperability of software used in this report.

The software described in section 1.3 has different key features and is used for different purposes in this report. In the following the software and their respective fields of application are described.

- Rhino - The 3D modelling engine where all geometries are generate.

- Grasshopper -Used for feature based parametric models. Development of analysis tools.

- Geometry Gym - Direct link for exporting models to Robot.

- Robot - FEA of secondary frame structures and simple shell structures.

- Sofistik - FEA of advanced double curved shell structures.

- SnS - Qualitative study of simple shell structures.

In addition to the commercial programs a number of free plug-ins for GH have been used. Furthermore, an interactive link between Sofistik and GH has been developed by use of Microsoft Excel. This link is the key feature for all analysis tools developed in GH specifically for this report. The tools use data exported from Sofistik to Excel such as the mesh geometry, local mesh coordinate systems and section forces. One could argue that the Excel link does not fit perfectly into the parametric approach but until now the Rhino-to-Sofistik link is a one way link that does not offer the possibility to automatically export data back to Rhino or Grasshopper. The analysis tools have been developed en route in order to visualise analysis results and hereby obtain a general understanding of these. The detail level of the analysis tools are kept to the conceptual and preliminary design phase level. Figure 1.3 illustrates the workflow and interoperability of Sofistik and Grasshopper for the structural design process carried out in this report.
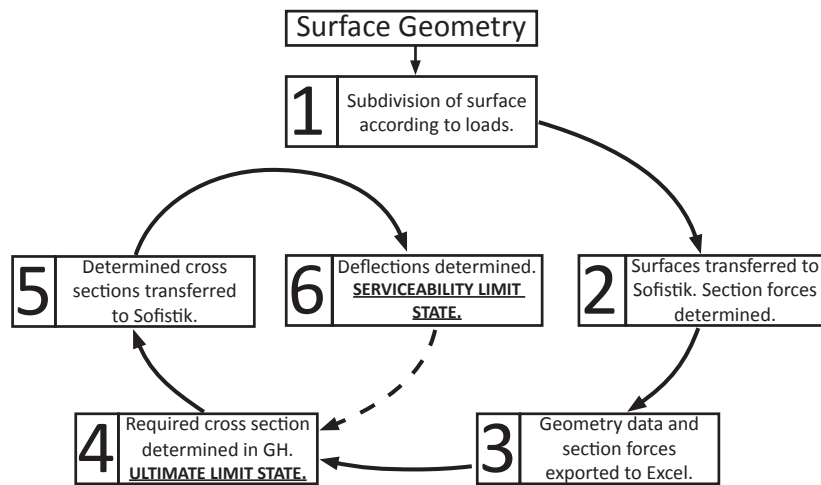
Figure 1.3: Diagram of workflow.

As a last remark it should be mentioned that the authors were only familiar with Robot at the beginning of the thesis period. This indicates the user-friendliness of the interfaces for most of the remaining programs used.

1.5 Organisation of Content

This thesis is divided into three parts including:
I   PART 1
II PART 2
III PART 3

Part I includes a series of qualitative studies where the structural behaviour of a shell of revolution is investigated. All studies have been carried out with a parametric modelling approach where the alteration of models is eased hence numerous variations of geometries can be analysed. Furthermore, section 3.3 contains an analytic verification of the used FEA software. **Part II** contains the development of a parametric model for pebble B in The Batumi Aquarium in order to create an optimised geometry. The main objective in **Part II** is a structural analysis consisting of geometry, linear and non-linear analyses for both the original and the optimised geometry. The geometries have been compared in terms of the material consumption. In **Part III** different proposals for the support of the upper pebble are presented. A secondary steel frame structure is dimensioned before the consequences of applying the load directly on the shell structure of pebble B is investigated.
Finally the conclusion sums up the observations done throughout the report.

[This page is intentionally left blank.]

Part I

Part 1

CHAPTER 2

Shell Structures

Shell structures have been used for hundreds of years in architecture and civil engineering and the technique goes as far back as to the Pantheon in Rome (figure 2.1 - the oldest known concrete shell structure in the world. Over time the level of complexity of geometries used within the architecture has increased where the tendency to use shell structures has changed from the construction of spacious buildings like domes to the construction of double curved and continuous surfaces to express an extraordinary and spatial geometric shape.
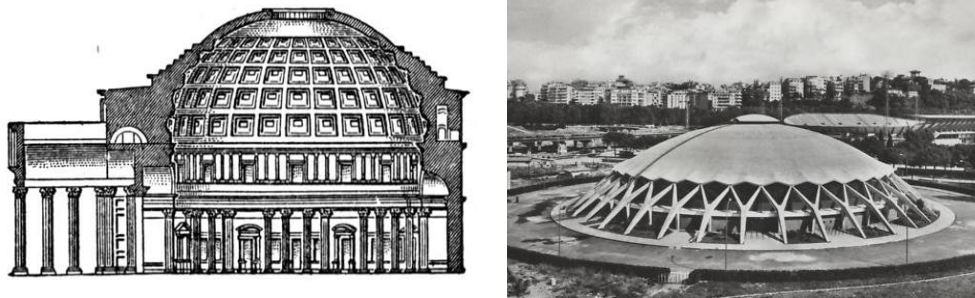

Figure 2.1: Pantheon, Rome and Palazetto dello sport, Rome. [19] and [20].

However it is not only from an architectural point of view that the boundaries for using shell structures have been extended. While beams and plates primarily have a flexural resistance mechanism, shells (disks and arches) have an in-plane resistance mechanism. Loads are resisted much more efficiently in in-plane mode than in flexural mode. This fact makes shell structures ideal in different engineering aspects.

In the following the advantages and disadvantages of using shell structures will be addressed. Furthermore, a short description of shapes and characteristics of different shell structures will be classified.

2.1   Use of Shell Structures

Different types of single curved shell structures are used for industrial purposes; oil storage tanks, in silos and in industrial chimneys. The single curved shell structures are very efficient in resisting certain types of loads, like external or internal uniform pressure. Though in some cases, it is better to take advantage of double curvature. Double curved shells can be used to build spherical gas reservoirs, roofs, outer hull structures for cars, ships and aircrafts, water towers and nuclear chimneys. Figure 2.2 shows examples of the use of double curved shell structures.
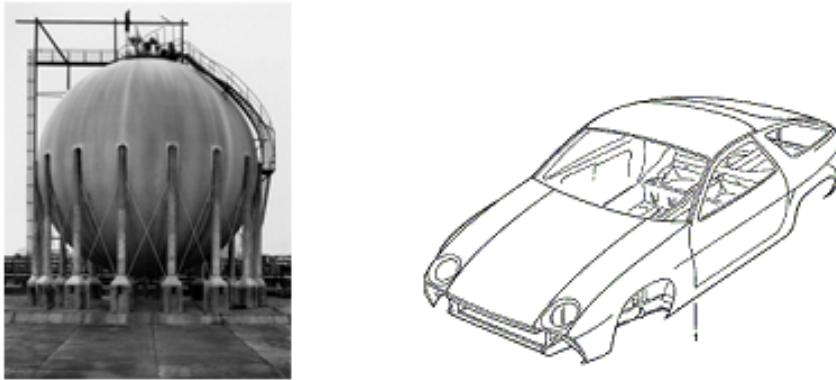

Figure 2.2: Spherical gas reservoir [25] and car bodywork[26].

Compared to plate structures shells have clear advantages from both an architectural point of view and as a structural member. The largest disadvantages when using shell structures are from a production point of view and failure regarding buckling [7]. Due to even small imperfections a thin shell will fail at a stress well below the theoretically calculated buckling stresses. Buckling can be prevented by increasing the cross section thickness hence increasing the flexural stiffness.

2.2   Classification and Mechanisms of Shell Structures

According to Ventsel and Krauthammer [6] a shell is defined as "a body bounded by two curved surfaces, where the distance between the surfaces is small in comparison with other body dimensions". The geometries of the curved surfaces initially divide the shells into different categories such as; *cylindrical, conical, spherical, ellipsoidal, paraboloidal, toroidal* and *hyperbolic paraboloidal* shells. All, except for the hyperbolic paraboloid are described as a *shells of revolution* are presented in figure 2.3.[6].
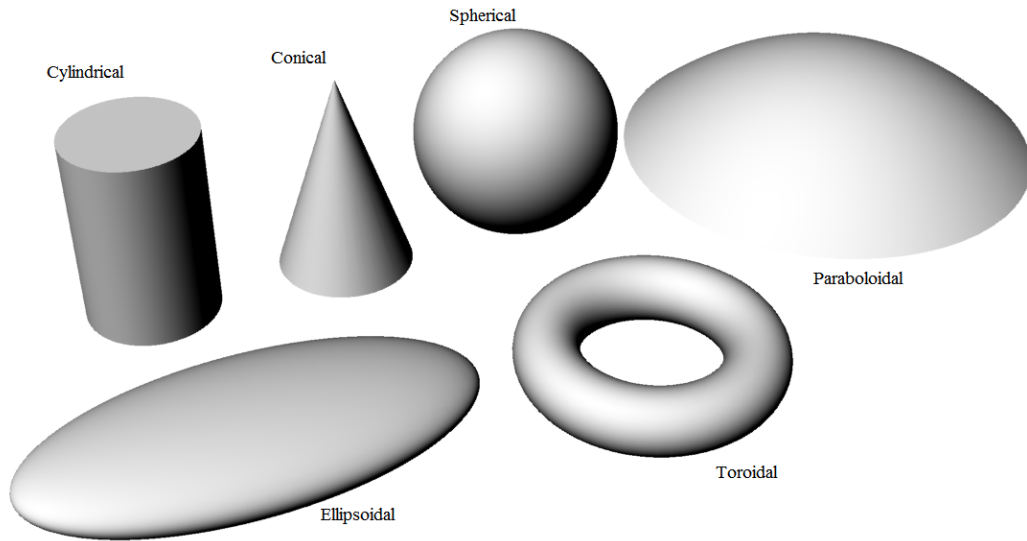
Figure 2.3: Geometric categories.

A governing presumption for all the above mentioned categories is that the shells have a *middle surface* (figure 2.4) located at an equal distance from the outer and inner surface. A distance denoted as half the thickness of the shell.
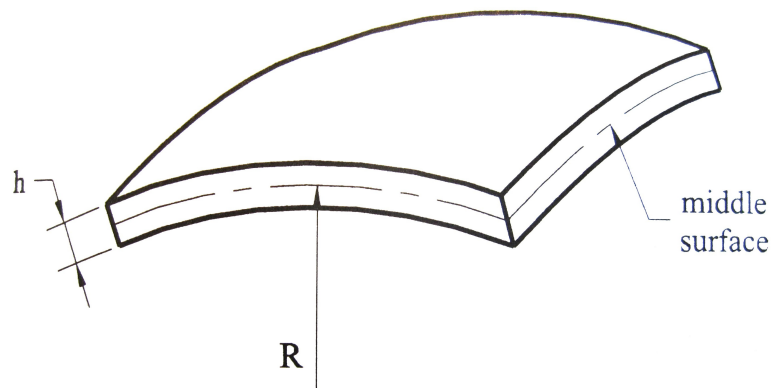
Figure 2.4: Middle surface.

As for plates, shells can be divided into two main classes according to their thickness; *thick* and *thin shells*. Where the class of thin shells is state to have the ratio[6]:

$$\frac{h}{R} \leq \frac{1}{20}$$

R is the radius of the curvature of the middle surface and h is the thickness of the shell.

The reason why shells are divided according to their curvatures and thicknesses is due to the fact that these parameters are directly associated with the efficiency of a shell [6]. The curvature of a shell surface acquires a spatial stiffness, hence a larger load carrying

capacity compared to a plate. This is due the fact that curved shell structures create a state where applied transverse loads are mainly distributed as tensile and compressive stresses and bending stresses minimized, hereby having a significant in-plane mode[1] . The curvatures of surfaces are often referred to in terms of *Gaussian curvature* with either a positive, negative or zero value.
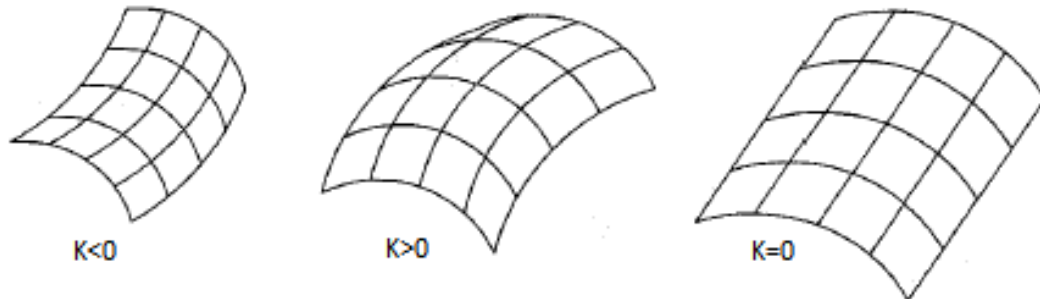

Figure 2.5: Gaussian curvatures.

The in-plane mode allow the shell structure a small thickness and therefore demonstrate a high efficiency in terms of a high strength/weight ratio. Due to the small thickness the shell possess a low strength for deformation caused by bending moments, these should therefore be avoided. However, under appropriate loading and boundary conditions[2] the bending stresses can be neglected. This state is referred to as the *membrane state of stress* and will be described in chapter 3.2.

These classifications and presumptions regarding categories, thickness, curvature and stresses all facilitate a simplification of the analytical expressions and hereby makes it possible to obtain an analytical solution for simple geometries. In the following sections only thin shell structure with a finite flexural stiffness will be considered.

---

[1]The whole cross section contribute to the load-carrying capacity

[2]Conditions for membrane theory: 1) *The boundaries of a shell are free from transverse shear forces and moments. Loads applied to the shell boundaries must lie in planes that are tangent to the middle surface of the shell.* 2) *The normal displacements and rotations at the shell edges are unconstrained: displace freely in the direction of the normal to the middle surface.* 3) *A shell must have a smoothly varying and continuous surface.* 4) *The components of the surface and edge loads must be also smooth and continuous functions of coordinates.*

Preliminaries of Shell Analysis

This chapter encompasses a brief introduction to the understanding of the *membrane theory* based on the governing *linear theory*[1] *of thin elastic shell structures* [6]. In order to simplify the extent of the introduction the membrane theory will only be clarified according to the shells of revolution category. Firstly, some of the presumptions according to the membrane theory of shells of revolution will be explained. Secondly, the membrane theory will be applied to a hemisphere for the analysis of the displacement due to an axisymmetric load. The analytic results will be conducted in order to verify the FEA software results performed in further structural analyses and design of shell structures.

3.1   The Membrane Theory of Shells of Revolution

As mentioned earlier appropriate loading and boundary conditions combined with the linear theory of thin elastic shells yield the membrane theory. The main presumption of the membrane theory is a shell resistance mechanism only due to in-plane mode, also called the *membrane state of stress*. Hereby neglecting the effects of the bending and twisting moments in the governing equations.

When investigating a shell of revolution exposed to an axisymmetrical load the membrane theory is even simpler. Due to axisymmetrical loading the external load component and displacements in circumferential direction are zero.

---

[1] Assumptions for linear theory: 1) *Normals to the undeformed middle surface remain straight and normal to the deformed middle surface and undergo extension.* 2) *The transverse normal stress is small compared with other normal stress components and may be neglected.*
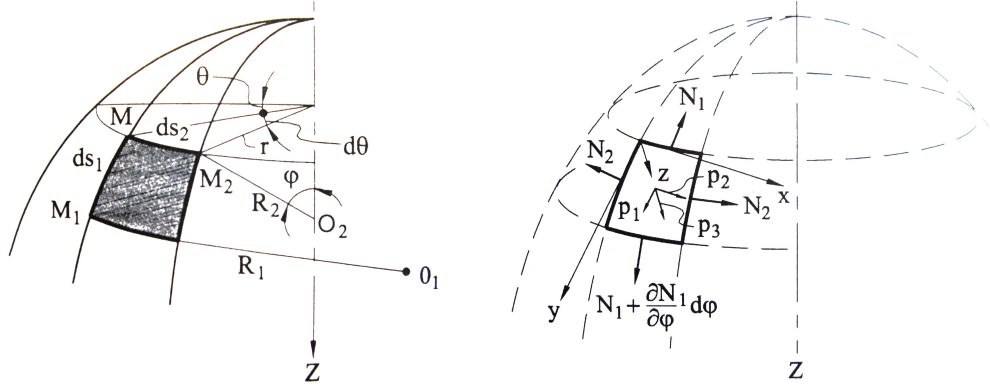
Figure 3.1: Membrane forces in an axisymmetrical loaded shell of revolution. [6]

From figure 3.1 p_2 is seen to be in the circumferential direction, hence $p_2 = 0$,as mentioned, the *kinematic*, *equilibrium* and *constitutive* equations can be simplified.

$$\frac{1}{R_1}\frac{du}{d\varphi} - \frac{w}{R_1} = \frac{1}{Eh}(N_1 - \nu N_2) = \varepsilon_1 \tag{3.1}$$

and

$$\frac{u}{R_2}\cot\varphi - \frac{w}{R_2} = \frac{1}{Eh}(N_2 - \nu N_1) = \varepsilon_2 \tag{3.2}$$

Now the displacement along the tangent u and normal to the middle surface w can be obtained from equation 3.3 and 3.4 by introducing the function $f_1(\varphi)$.

$$u = \sin\varphi \int f_1(\varphi)d\varphi + C_1 sin\varphi \tag{3.3}$$

and

$$w = \cos\varphi \int f_1(\varphi)d\varphi + C_1 cos\varphi - \varepsilon_2 R_2 \tag{3.4}$$

The function $f_1(\varphi)$ is conducted from equation 3.1 and 3.2 according to Ventsel and Krauthammer, [6], and determined in terms of the strain components and the curvature radius.

$$f_1(\varphi) = \frac{R_2}{sin\varphi}\frac{R_1}{R_2}\varepsilon_1 - \varepsilon_2 \tag{3.5}$$

$f_1(\varphi)$ can be found when N_1 and N_2 have been determined for the analytic setup. N_1 and N_2, for a hemisphere, are determined from the following equations:

$$N_1 = -\frac{1}{r sin\varphi}\int_0^{\varphi} rR_1(p_1 sin\bar{\varphi} + p_3 cos\bar{\varphi})d\bar{\varphi} \tag{3.6}$$

and

$$N_2 = -R_2\left(p_3 + \frac{N_1}{R_1}\right) \tag{3.7}$$

C_1 is a constant of integration and can be found from the boundary conditions for the shell. By applying the previous equations and functions to a certain shell problem the displacement in both u and w directions can be calculated with certain accuracy.

3.2 Application of Membrane Theory of Shells of Revolution

The application of the membrane theory will be based on a hemisphere as seen from figure 3.2 subjected to an axisymmetrical load of p per unit area acting in the global vertical direction.
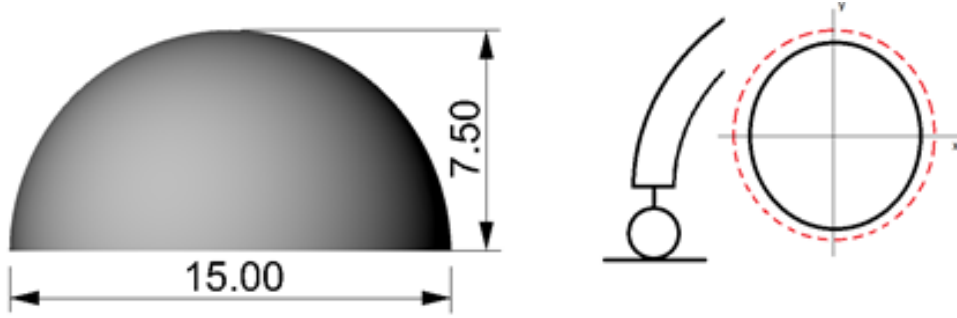

Figure 3.2: Shell dimensions, boundary conditions and deformation behaviour.

The boundary condition for the hemisphere is hinged with free movement in the normal direction (w) of the shell. The red dotted line in figure 3.2 indicates the deformation of the base. Furthermore it is noted that for a hemisphere $R_1 = R_2 = R$.

With the applied boundary conditions bending moments at the base are avoided. However, when the base of the shell is inclined a circumferential force, T, has to be obtained in the shell due to a horizontal component from the tangential force N_1. The magnitude of the force in the circumferential direction depends on the angle[2] between the origin and the boundary condition. In the case of the axisymmetrical load of p per unit area the force T can be calculated by the following equation. See appendix B.2.

$$T = pR^2 \frac{cos\varphi_1 sin\varphi_1}{1 + cos\varphi_1} \tag{3.8}$$

By the following equations the displacement of the hemisphere is expressed. Firstly, the axisymmetrical load of p per unit area is transformed into components according to figure 3.1:

$$p_1 = p\,sin\varphi \tag{3.9}$$

and

$$p_3 = p\,cos\varphi \tag{3.10}$$

Now it is possible to obtain N_1 and N_2 from equation (3.6) and (3.7):

$$N_1 = -pR \frac{1 - cos\varphi}{1 - cos^2\varphi} = -\frac{pR}{1 + cos\varphi} \tag{3.11}$$

and

$$N_2 = -pR\,cos\varphi + \frac{pR}{1 + cos\varphi} = -pR\left(cos\varphi - \frac{1}{1 + cos\varphi}\right) \tag{3.12}$$

---

[2]Below 90 degrees a tension forces and above 90 degrees a compression force has to be obtained.

The constant C_1 can now be evaluated from the boundary conditions, $u = 0 | \varphi = \varphi_1$. See figure 3.1, 3.2 and equation (3.3).

$$C_1 = \frac{pR^2(1+\upsilon)}{Eh} \, \frac{1}{1 + cos\varphi_1} - \ln(1 + cos\varphi_1) \tag{3.13}$$

The displacement u along the tangent and w in the normal direction are yielded from equation (3.3) and (3.4) and the constant C_1:

$$u = \frac{pR^2(1+\upsilon)}{Eh} \, sin\varphi \left(\ln\frac{1 + cos\varphi}{1 + cos\varphi_1} + \frac{cos\varphi - cos\varphi_1}{(1 + cos\varphi)(1 + cos\varphi_1)} \right) \tag{3.14}$$

and

$$w = \frac{pR^2(1+\upsilon)}{Eh} \, cos\varphi \left(\ln\frac{1 + sin\varphi}{1 + sin\varphi_1} + \frac{sin\varphi - sin\varphi_1}{(1 + sin\varphi)(1 + sin\varphi_1)} \right) - \varepsilon_2 R \tag{3.15}$$

The analytical deflection of the hemisphere found from 3.14 and 3.15 will serve as the reference deflection for the verification of FEA software conducted in the following section.

3.3   Verification of FEA Software

This section will verify the chosen FEA software by comparing analytical results to the results from Robot, SnS and Sofistik.
To ensure the accuracy of the chosen FEA software simple plate geometries are investigated and the maximum deflections are compared to known sizes of deflection from basic plate theory. A rectangular plate fixed in both ends and a circular plate fixed along the outer edge, as shown on figure 3.3 and 3.4, are investigated. Further the deformations of the hemisphere shown in figure 3.2 will serve as setup for the last verification.

Rectangular Plate

A plate, fixed in both ends with the properties found in table 3.1, is investigated.

Table 3.1: Rectangular plate - properties.

Length	Width	Thickness	Load	Material
10m	5m	0,3m	300kPa	S235

The maximum deflection at midspan of a plate can be found from basic beam theory and has a size of[10]:

$$u_{max} = \frac{1}{384} \frac{pl^4}{EI} \tag{3.16}$$

The analysis setup for the rectangular plate from Robot can be seen in figure 3.3:
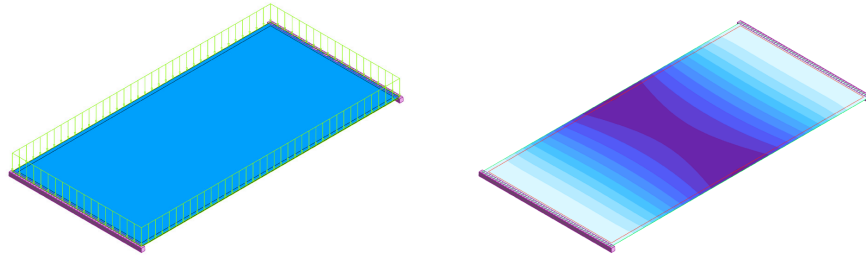
Figure 3.3: Rectangular plate - Robot.

The maximum deflections found from analyses of the rectangular plate in Robot, SnS and Sofistik are compared to the analytical deflection in table 3.2.

Table 3.2: Rectangular plate - vertical deflection.

Rectangular Plate	Maximum Deflection	Deviation
Analytical	17,98	-
Robot	18,08	0,5%
SnS	17,39	3,2%
Sofistik	18,10	0,67%

Circular Plate

A circular plate with the properties seen in table 3.3 is investigated. Again the maximum deflection is the matter of comparison.

Table 3.3: Circular plate - properties.

Radius	Thickness	Load	Material
10m	0,3m	300kPa	S235

The maximum deflection of a circular plate fixed along the boundary edge is found in the center of the plate when exposed to a uniformly distributed load. The analytical deflection is found from the following expressions[10]:

$$u_{max} = \frac{pR^4}{64D} \tag{3.17}$$

Where

$$D = \frac{Et^3}{12(1 - \nu^2)} \tag{3.18}$$

The analysis setup from Robot can be seen in figure 3.4.
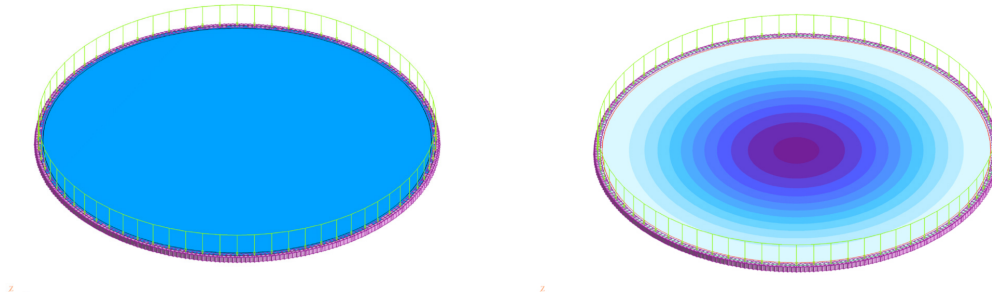
Figure 3.4: Circular plate - analysis setup.

The maximum deflections found in the center point of the circular plate with Robot, SnS and Sofistik are compared to the theoretical deflection in table 3.4.

Table 3.4: Circular plate - vertical deflection.

Circular Plate	Maximum Deflection	Deviation
Analytical	6,14	0%
Robot	6,17	0,5%
SnS	5,84	4,9%
Sofistik	6,24	1,6%

Hemisphere

Finally a verification of Robot and Sofistik[3] is carried out by the investigation of a hemi-spherical shell structure exposed to a uniformly distributed vertical load. Figure 3.2 shows the investigated geometry. The analytical deflections and membrane forces found as described in section 3.2 are used as the reference values. Table 3.5 shows geometrical and sectional properties of the hemisphere.

Table 3.5: Hemisphere properties

Radius	Thickness	Load	Material
7,5m	0,025m	1MPa	S235

The resulting deflections, membrane forces and moments at $\varphi = 0°$, $\varphi = 15°$ and $\varphi = 45°$ on the hemisphere (figure 3.1) can be found in table 3.6, 3.7 and 3.8 respectively.

Table 3.6: Robot and Sofistik deviations for the hemisphere setup. $0°$.

$\varphi = 0°$	Analytic	Robot	Deviation [%]	Sofistik	Deviation [%]
w [mm]	17,76	19,10	7,55	19,44	9,45
u [mm]	0	0	0	0	0
N_1 [kN/m]	-7500	-7579	1,05	-7510	0,13
N_2 [kN/m]	-7500	-7579	1,05	-7504	0,05
M_1 [kNm/m]	0	6,75	-	1,78	-
M_2 [kNm/m]	0	6,75	-	2,23	-

---

[3]SnS is not included in this verification since the trial version only contains clamped support conditions.

Table 3.7: Robot and Sofistik deviations for the hemisphere setup. $15°$.

$\varphi = 15°$	Analytic	Robot	Deviation [%]	Sofistik	Deviation [%]
w [mm]	16,65	18,97	13,93	18,50	11,11
u [mm]	3,59	4,21	17,27	4,13	15,04
N_1 [kN/m]	-7630	-7628	0,03	-7636	0,07
N_2 [kN/m]	-6859	-6842	0,24	-6830	0,42
M_1 [kNm/m]	0	1,31	-	0,56	-
M_2 [kNm/m]	0	1,27	-	-0,02	-

Table 3.8: Robot and Sofistik deviations for the hemisphere setup. $45°$.

$\varphi = 45°$	Analytic	Robot	Deviation [%]	Sofistik	Deviation [%]
w [mm]	8,07	8,77	8,67	8,55	5,95
u [mm]	8,65	9,35	8,09	9,13	5,55
N_1 [kN/m]	-8787	-8770	0,20	-8782	0,05
N_2 [kN/m]	-1820	-1827	0,37	-1815	0,26
M_1 [kNm/m]	0	0,97	-	0,33	-
M_2 [kNm/m]	0	0,97	-	-0,18	-

Discussion

It is seen from the investigation that the maximum deflections are almost similar for all programs tested when considering the planar structures: the rectangular plate and the circular plate. It is worth noticing though that the deflections calculated by SnS are consistently smaller than the analytical deflection used as the reference deflection in this verification. This is not the case for both Robot and Sofistik and because of the insecurity regarding the FE method[4] used in SnS and the limitations in the student version, this program is not used for quantitative studies further in this report.

The deviation of 17,27 % and 15,04 % for Robot and Sofistik seems large but it is worth noticing that the actual difference in the deflection is 0,62mm and 0,54mm respectively for a hemisphere with a radius of 7,5 m. Furthermore, the deflection found by the use of Robot and Sofistik are almost similar for the three different angles and are all conservative when compared to the analytical deflection. Even though the deviation are relatively large they are deemed acceptable and will be used for the analyses carried out in the succeeding parts of the project. Finer meshed geometries have been investigated which did not influence the deviations significantly indicating a convergence of the section forces and deflection.

Finally it is worth mentioning that all geometries were investigated with varied thicknesses in an attempt to clarify whether or not this would influence the deviations. This was not the case in any of the setups.

---

[4]Without going into too much detail about meshing methods in general; Robot was set to use the coons meshing method, Sofistik used a rectangular mesh pattern while SnS uses a meshing method that divides the given geometry into cubic shapes with planar surfaces parallel to a global coordinate system.

[This page is intentionally left blank]]

CHAPTER 4

Qualitative Study of Shells Structures

In order to obtain a better understanding of the behaviour of shell structures, subjected to comparable loading and boundary conditions, a qualitative approach based on paper and computational models is used. Hereby, an intuitive understanding and foundation for predicting the deformation behaviour of shell structures of varying curvature is possible.

The qualitative method has been divided into two steps; Firstly the deformation behaviour of simple paper models exposed to a vertical load, imitating the impact from pebble A on pebble B, has been compared with identical computational models exposed to a similar load type. Secondly the deformation behaviour of more advanced computational models exposed to different load types have been observed in order to understand the geometry of the pebble B. By comparing different models it is possible to differentiate geometric shapes in terms of stiffness[8]. Within this qualitative study the differentiation is very rough due to the fact that it is based on deformation behaviour and not exact deformation values.

4.1 Preliminary Qualitative Study of Paper and Computational Models

The Batumi Aquarium, pebble B, has four geometrical characteristics in form of:

- Roughly shaped as an hemisphere.

- Inclined base geometry.

- Planar areas.

- Concave areas.

Three paper models of shells with positive curvatures have been constructed from *the basic shell configurations* collection created by Henrik Almegaard[8]. In order to investigate physical models with similar characteristics to the pebble B. A hemisphere (*a*), a hemisphere with a vertex hole (*b*) and a hemisphere with a vertex hole and breaches at the boundary (*c*) were constructed in paper. The geometries can be seen in figure 4.1
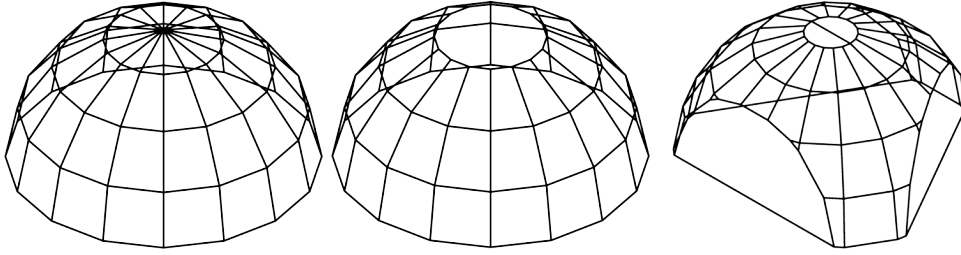
Figure 4.1: Geometry a, b and c.[8].

Faceted shell structures have been proved to have stability properties, under certain circumstances, equal to smooth shell structures [8]. Therefore the same structural behaviour would occur for a smooth shell. By approximately subjecting the different shell structures to the same vertical load it is possible to see the interrelation between the deformation behaviours.
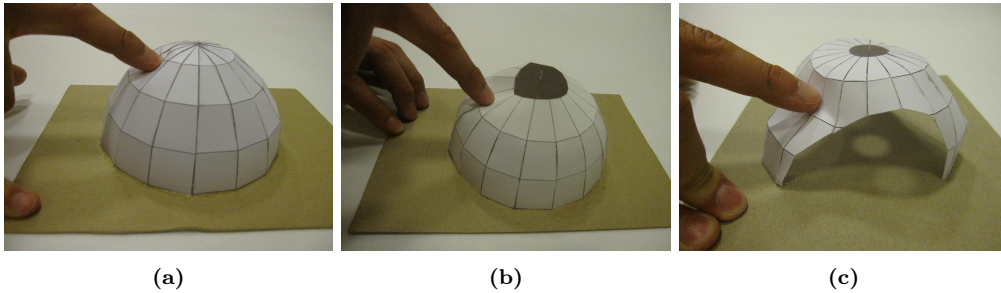

(a)	**(b)**	**(c)**

Figure 4.2: Example of paper models.

Model a only experiences a local deformation, while model b is seen to be weak, in terms of deformation, around the vertex hole, and the implementation of a hoop is necessary to reduce deformations. The least resistant model is model c where large deformations occur in both the structural "legs" and around the vertex hole.

In the following similar shell structures have been analysed by the use of Rhino and the plug-in SnS[1]. The use of SnS is justified, despite the deviation found in section 3.3, when the a deformation behaviour is only analysed visually. The models are based on a hemisphere with the properties stated in table 4.1.

Table 4.1: Hemisphere properties

Radius	Shell Thickness	Material
7,5 m	0,05 m	Concrete

Each model is subjected to a vertical load and has clamped boundary conditions, see figure 4.3.

---

[1]Due to limitations in the trial version of SnS, only clamped supports and concrete material properties are applicable.
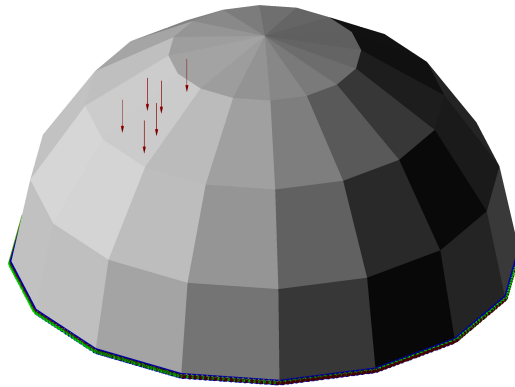
Figure 4.3: SnS - facetted hemisphere and applied load.

4.1.1 Facetted Computational Models

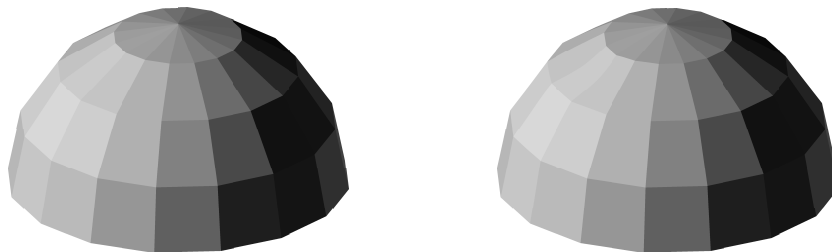The deformed facetted shell structures can be seen from figure 4.4, 4.5 and 4.6:

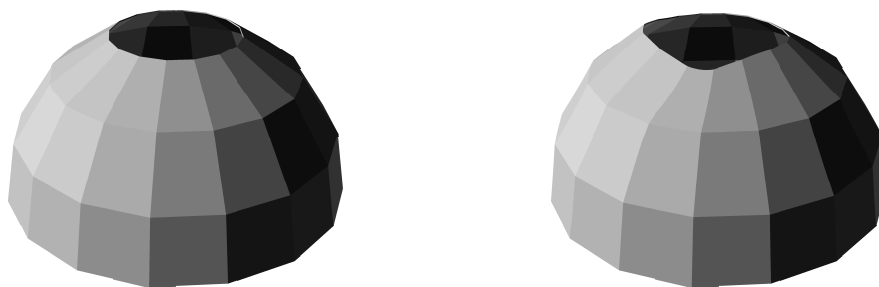**Figure 4.4:** Deformation plot of model *a*. Deformation scale 1:400.

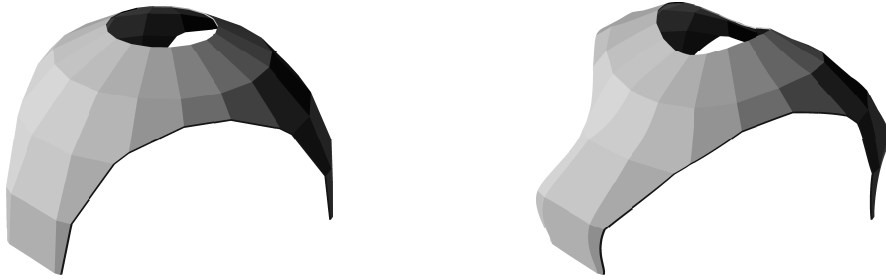**Figure 4.5:** Deformation plot of model *b*. Deformation scale 1:400.

Figure 4.6: Deformation plot of model *c*. Deformation scale 1:400.

The deformations of the shells increase as the continuity and material, hence less overall stiffness, is reduced. It is observed that the deformation behaviours are identical to the results seen from the paper models in figure 4.2. This study verifies the qualitative method and allows a further investigation of more advanced computational models as carried out in the following section.

4.2   Qualitative Study of Advanced Computational Models

Even though the 18 models contained in *the basic shell configurations* collection[8] to a very large degree may represent scaled models of actual shell structures, they are relatively time consuming to construct. New 3D modelling and FEA software however enables a simple tests of the deformation behaviour of smooth shell structures with an arbitrary geometric shape.

As it will be seen later in this report pebble B supports the upper pebble A and is therefore exposed to a point load relatable to the point loads investigated in this section. The investigation of the smooth shells is conducted under the same load and boundary conditions as the faceted shell structures.

4.2.1   Smooth Computational Models

To expand the understanding of the deformation behaviour, in regards to the before mentioned four characteristics of pebble B, five different shell structures has been investigated. All geometries are modelled parametrically through GH. The GH script can be found in appendix D1. The overall parameters of the geometries are the variations of the upper part going from convex to concave curvature as well as the base geometry going from an inwards to an outwards direction. The geometries are modelled as one polyline curve, which is revolved around the z-axis as illustrated on figure 4.7.
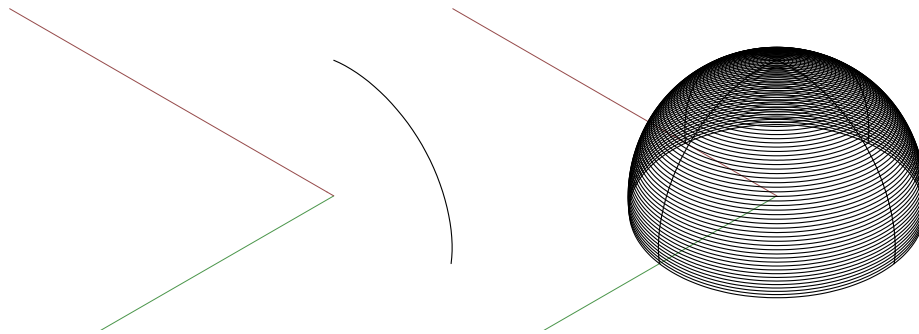
Figure 4.7: Revolved shell structure.

All deformation plots have the same scaling factor in order to compare the results. The red arrows indicate the deformation direction of the most exposed areas.
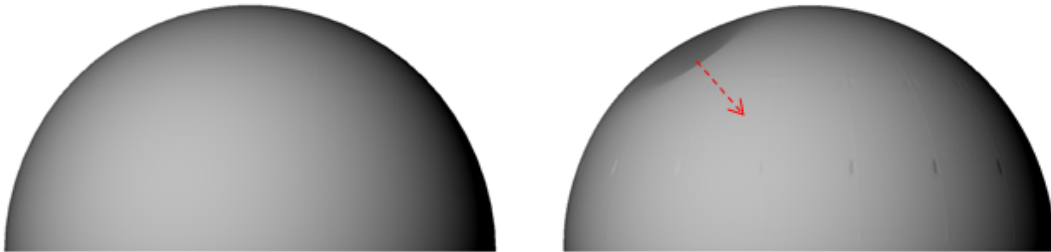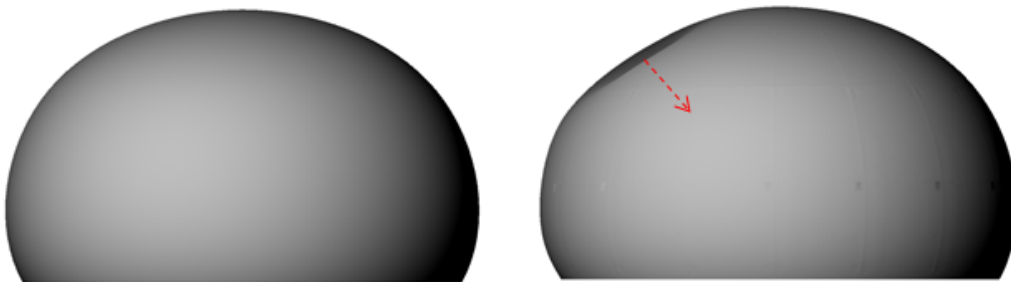

Figure 4.8: Deformation plot. Hemisphere.

Figure 4.9: Deformation plot. "Legs" directed inwards.

Figure 4.10: Deformation plot. "Legs" directed outwards.

From the previous three figures it is seen that the change of the lower part of the shell, going from inwards to outwards, does not influence the overall deformation behaviour. However, the shells experience large local deformations. From the conclusion that the geometry of the "legs" has an insignificant influence on the deformation behaviour, when exposed to a vertical point load, only model *e*, figure 4.9, will be further investigated as the inwards directed base geometry resembles pebble B. To investigate how planar and concave areas on the shell geometry influence the deformation behaviour, when exposed to a vertical point load, the following two figures have been analysed.
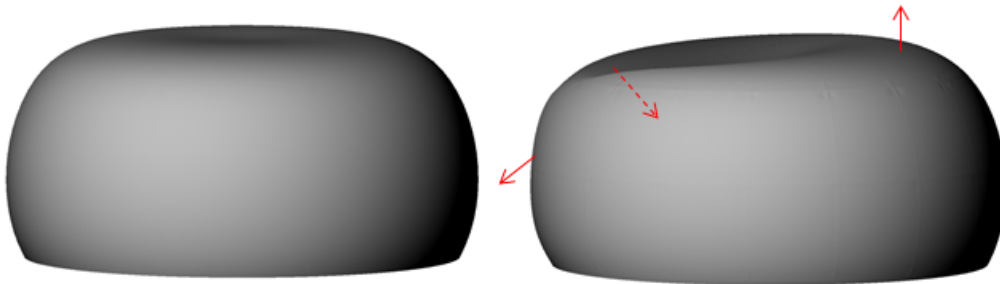

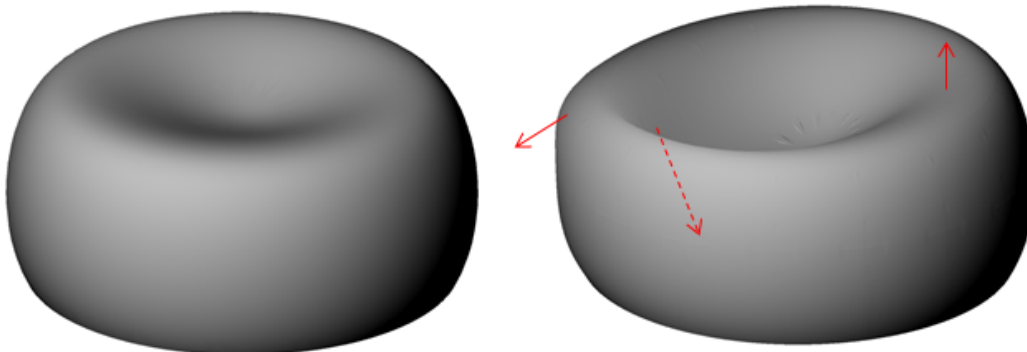**Figure 4.11:** Deformation plot. Planar upper geometry.

Figure 4.12: Deformation plot. Concave upper geometry.

Having a planar area at the vertex of the hemisphere, as seen in figure 4.11, generates a more comprehensive deformation. The same tendency is seen in figure 4.12 although the deformation of the concave area is best expressed as a total collapse.
By comparing figure 4.8 to figure 4.11 and 4.12 it is seen that a planar or concave area influences the overall stiffness of a shell structure when exposed to a point load even though the areas are not directly exposed to the load. This indicates the consequences of geometric discontinuities within a shell structure.

4.3   Summary

It is seen from figure 4.4 and 4.8 that the deformation behaviours of a smooth and faceted shell are identical. This is also stated by Henrik Almegaard [8]. The base geometry has an insignificant influence on the deformation behaviour compared to planar and concave areas

when exposed to a vertical point load. The planar and concave areas of a shell structure are very sensitive in regards to a point load even when the areas are not directly exposed to the load.

It can be concluded that obtaining a point load from pebble A on pebble B will have a high impact at any area with geometric discontinuities even located at some distance from the load point.

[This page is intentionally left blank.]

Geometric Comparison of Shell Structures

In this chapter the importance of general alterations of the overall geometry of an axisymmetric shell structure will be clarified in regards to two different load types. The hemisphere from the previous section is used as reference geometry and the maximum deflections are compared in an attempt to clarify the influence of convex and concave geometries respectively but also the influence of a varying base geometry.

Finally a detailed investigation of the vertical deflection, when the upper part of a hemisphere is changed towards a planar and finally concave geometry, will be carried out.

5.1 Analysis Setup

Based on the analysis setup from section 4.2.1 nine geometries are exposed to two cases of a uniformly distributed load: Vertical and horizontal. The geometries have been chosen in accordance to the different characteristics of pebble B as mentioned in section 4.

Both loads are based on a 1 MPa load distributed on the reference geometry - the hemisphere. Illustrations of the various loads acting on the geometries can be found in the respective result sections in this chapter. All geometries are modeled as S235 steel with a thickness of 25 mm. Both loads are uniformly distributed loads - vertical and horizontal respectively.

The geometries are constructed as explained in section 4.2.1 and are *baked* to Robot by GG with section properties applied. Supports are assigned in Robot and loads are applied to the surfaces. Once the GH script is created the whole process from geometry to finite element model in Robot is significantly faster than creating the geometry from scratch directly in Robot.

5.2 Vertical Load Comparison

Deflections, membrane forces and bending moments in figure 5.1 are found at the vertex of the geometries which is also where the maximum vertical deflection is found for the shell structures exposed to a uniformly distributed vertical load. It should be mentioned that the nine different structures are all exposed to the same resulting vertical force since the distributed loads have been adjusted to the given surface areas of the nine geometries.
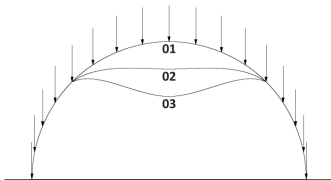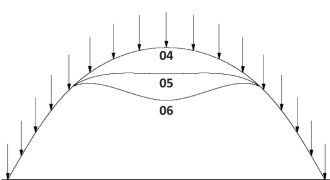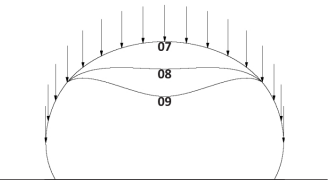
Structure 01-03	Structure 04-06	Structure 07-09

Structure 01

Loaded Surface Area:
352 m²
Membrane force, N1=N2:
-3530 kN/m
Bending moment, M1=M2:
3,35 kNm/m
Vertical deflection:
19,1 mm

Reference Deflection Factor:
1,0

Structure 04

Loaded Surface Area:
399 m²
Membrane force, N1=N2:
-3508 kN/m
Bending moment, M1=M2:
2,19 kNm/m
Vertical deflection:
13,2 mm

Relative Deflection Factor:
0,7

Structure 07

Loaded Surface Area:
242 m²
Membrane force, N1=N2:
-4008 kN/m
Bending moment, M1=M2:
3,24 kNm/m
Vertical deflection:
27,8 mm

Relative Deflection Factor:
1,5

Structure 02

Loaded Surface Area:
345 m²
Membrane force, N1=N2:
24721 kN/m
Bending moment, M1=M2:
-586,04 kNm/m
Vertical deflection:
1590,2 mm

Relative Deflection Factor:
83,3

Structure 05

Loaded Surface Area:
392 m²
Membrane force, N1=N2:
25030 kN/m
Bending moment, M1=M2:
-537,83 kNm/m
Vertical deflection:
1495,2 mm

Relative Deflection Factor:
78,3

Structure 08

Loaded Surface Area:
230 m²
Membrane force, N1=N2:
31017 kN/m
Bending moment, M1=M2:
-263,05 kNm/m
Vertical deflection:
1703,4mm

Relative Deflection Factor:
89,2

Structure 03

Loaded Surface Area:
346 m²
Membrane force, N1=N2:
2003 kN/m
Bending moment, M1=M2:
6,36 kNm/m
Vertical deflection:
1112,0 mm

Relative Deflection Factor:
58,2

Structure 06

Loaded Surface Area:
394 m²
Membrane force, N1=N2:
1963 kN/m
Bending moment, M1=M2:
5,65 kNm/m
Vertical deflection:
1106,0 mm

Relative Deflection Factor:
57,9

Structure 09

Loaded Surface Area:
226 m²
Membrane force, N1=N2:
1898kN/m
Bending moment, M1=M2:
7,11 kNm/m
Vertical deflection:
1001,8 mm

Relative Deflection Factor:
52,5

Figure 5.1: Deflection table - uniformly distributed vertical load

Interestingly the shell structures with outwards directed base geometry (structure *04-06*) secures a smaller deflection than the structures with vertical supports (structure *01-03*). Structure *07* with inwards base geometry experiences an increase in the vertical deflection of about 50%. All structures with zero curvature at the vertex and concave curvature at the vertex (*02*, *03*, *05*, *06*, *08* and *09*) result in deflections of relative sizes that are too large to even consider implementing in an actual construction without supporting the shell structures by secondary structural systems. For structure *02*, *04* and *06* the large deflections are directly related to the large bending moments while the large deflections for structure *03*, *06* and *09* are related to the discontinuity in curvature at the edge of the concave areas. Comparing the membrane forces of the convex and concave geometries shows that the upper part of the convex geometries are in compression as opposed to the tension found at the vertex of the concave geometries hence a the Gaussian curvature controls the operational sign of the membrane forces.

Since not only perfectly convex shell structures will be used further on in this project the convexity and concavity-investigation in section 5.4 will seek to investigate how the deflection develops when going from a convex to a planar upper part of the hemisphere in greater detail than done in figure 5.1.

5.3 Horisontal Load Comparison

Nine geometries similar to the ones investigated in the previous section have been analysed in regards to horisontal loading - imitating a wind load pressure on the geometries. More specifically a uniformly distributed horizontal load of 1MPa. All geometries have been applied section properties with a thickness of 25 mm and S235 steel as the section material. Figure 5.2 on the following page shows the deformation shapes, the maximum total deflections and presents the relative deflection factor of the various geometries. The hemisphere is the reference geometry in this regard.

[See next page for illustration]

Again it must be concluded that the structures with concave curvature at the vertex are less suitable for load carrying purposes when exposed to a horisontal load though the relative deflection factors in this section are not as large as found for the vertically distributed load. However, the geometries with planar areas around the vertex are quite stiff when exposed to a horisontal distributed load. By comparing the deflections from 5.1 it seens that the load direction towards the planar areas is of great importance when considering the stiffness of these geometries.
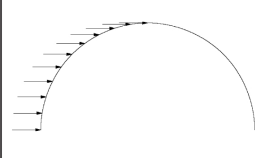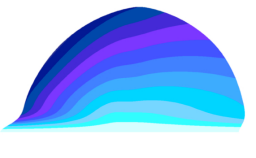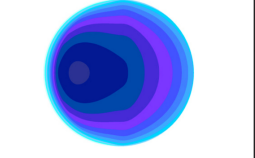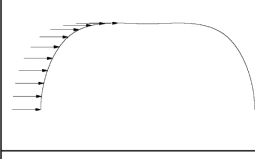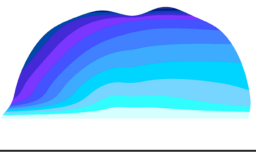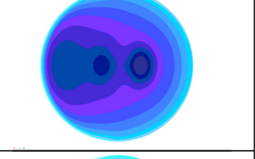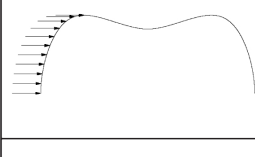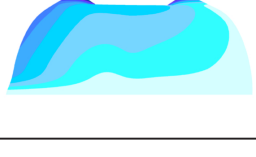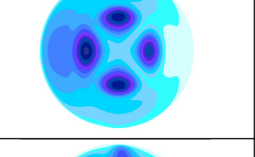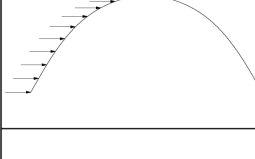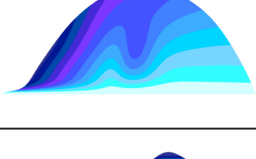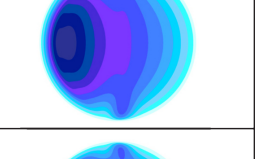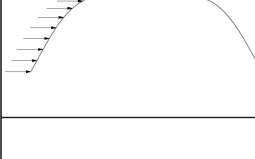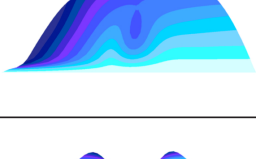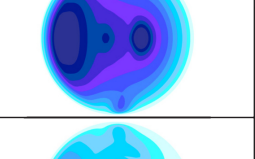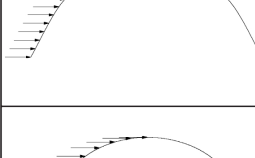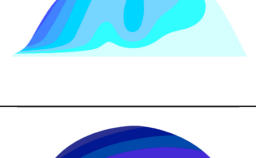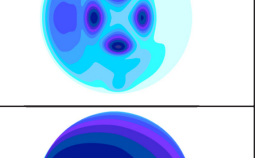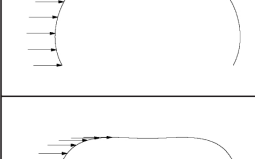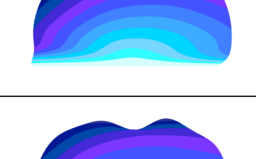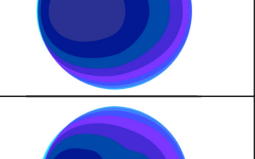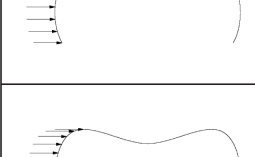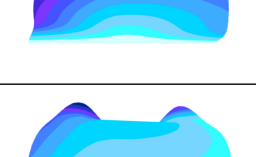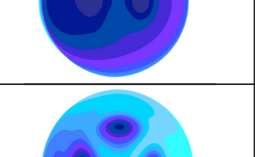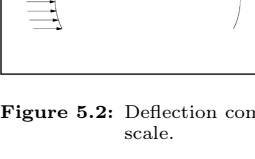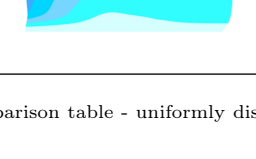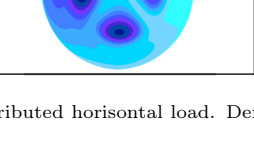
Figure 5.2: Deflection comparison table - uniformly distributed horisontal load. Deformartion figures of varying scale.

5.4   Convexity and Concavity Investigation

From the previous investigations it was concluded that the curvature of the shell structure is of great importance when it comes to the overall stiffness. In continuation of these first steps a more detailed investigation of the behaviour of the structure in regards to a convex and concave upper part is carried out. Due to the interoperability between Rhino, Grasshopper and Robot by the use of GeometryGym the finite element models are generated faster than otherwise possible directly in the Robot interface. A total number of 22 shell structures, generated parametrically from the script described in section 4.2.1 have been investigated. The nature of the alteration of the geometry is shown in figure 5.3[1].
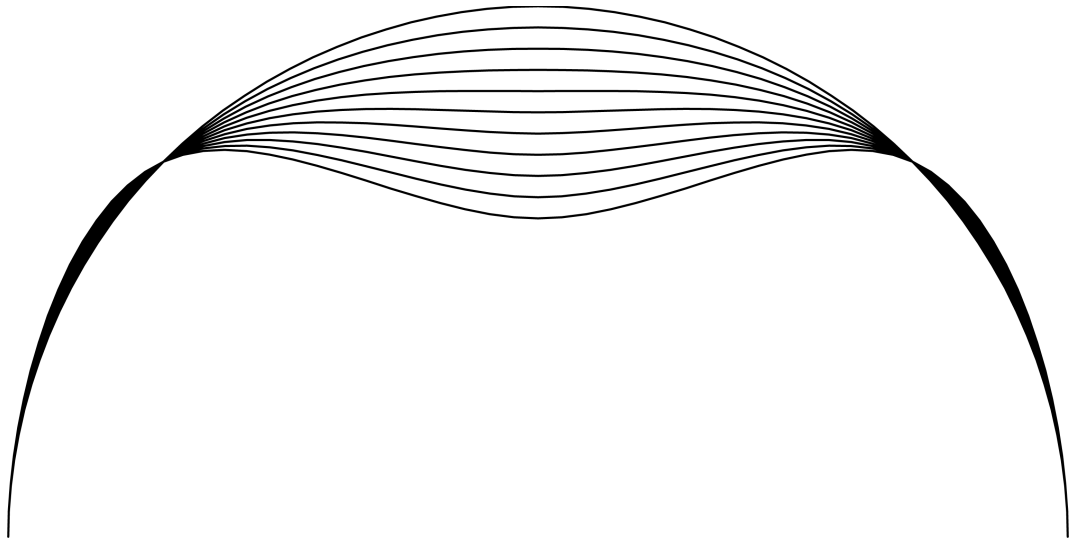
Figure 5.3: Convex and concave geometries.

The vertex of the geometry in the investigation goes from a concave geometry with a center height of 4,5 m to a convex geometry with a center height of 7,5 m in 22 steps. All geometries are exposed to a uniformly distributed vertical load of 1 MPa and have been applied with a 25 mm S235 steel cross section. Exact values of the deflections, membrane forces and bending moments can be found in appendix C.1.

---

[1]Please note that more geometries than the ones shown in figure 5.3 have been investigated.

5.4.1 Results

To investigate how the upper geometry of the shell structures influence the section forces and hence the deflection the two following diagrams have been generated. The diagrams illustrate the maximum deflection compared to the membrane forces and bending moments respectively at the vertex of the geometries.
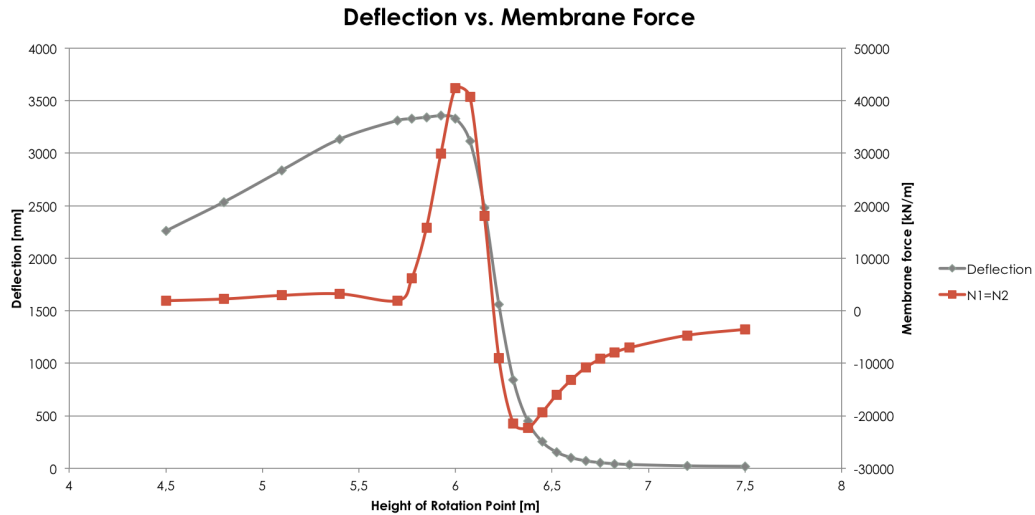
Figure 5.4: Deflection vs. membrane force.
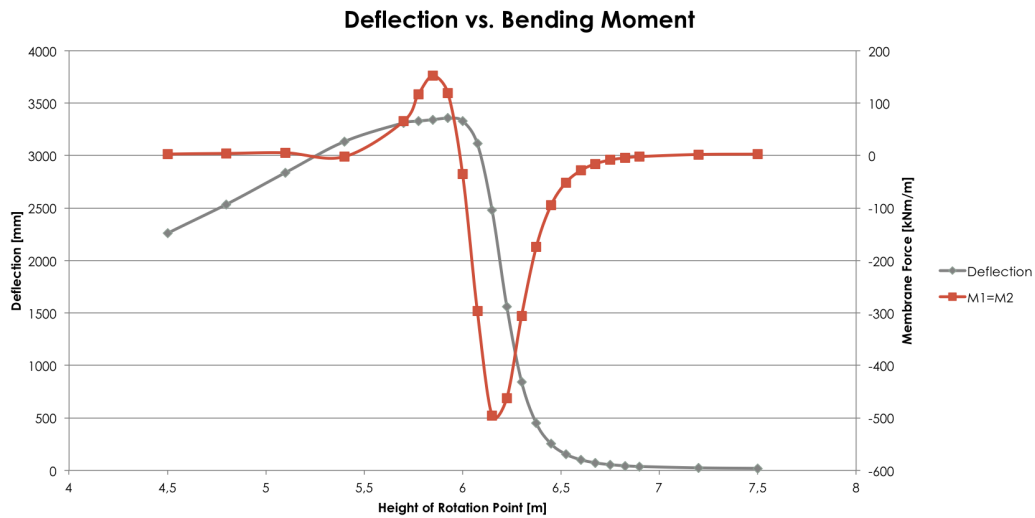
Figure 5.5: Deflection vs. bending moment.

It is seen from figure 5.4 and 5.5 that the deflection escalates when the upper part of the structure is flattened. As mentioned earlier in this report the stiffness of the shell structure is relative to the curvature of the shell geometry. The curvature at the vertex is approximately zero when the height of the rotation point is between 6,0 m and 6,3 m which is also where the structure reaches the largest vertical deflections. When the upper part of the

shell structure is flattened the structure behaves as a plate which means that the bending moments are increased and the membrane forces are reduced. Large bending moments will result in large deformation for a thin shell like this.

Interestingly the shell structure still experiences large deformations when the bending moments are reduced for the concave geometries (height of centre of rotation: 4,5m to 5,5m). From the above argumentation the shell structure regains its stiffness when the curvature is increased for the concave structures. However, the explanation for the large deflections can be found at the curvature discontinuity around the edge of the concave area where the tangent of the shell curvature is perpendicular to the load direction. This is where the shell deflects for the concave geometries which results in a vertical deformation of the upper part of the shell as a whole.

To sum up neither planar and concave areas on the shell structure are unfavourable in regards to the overall deflection of the structure. The hemisphere is the stiffest of the investigated structures while the convex, but not perfectly hemispherical structures, experience deflections not too far from the optimal hemisphere. A more detailed deflection curve for the convex geometries can be found in figure 5.6.
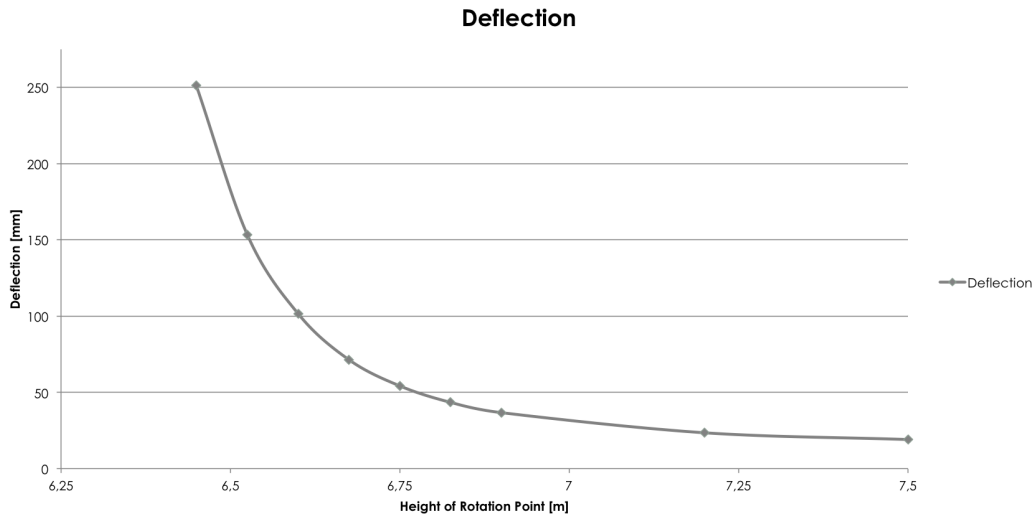
Figure 5.6: Deflection of convex geometries.

[This page is intentionally left blank.]

Part II

Part 2

CHAPTER 6

The Batumi Aquarium

Inspired by the characteristic pebbles of the Georgian Black Sea coastline the Batumi Aquarium will stand out as an iconic rock formation visible from both land and sea.

The Batumi Aquarium is designed by Henning Larsen Architects in collaboration with Buro Happold and Blu Technologies and holds four exhibition areas all representing different marine biotypes - the Mediterranean, the Black Sea, the Aegean Sea and the Indian Ocean. The four exhibition areas are connected by a centrally located atrium well suited for presentations and workshops. The atrium will also hold a café and retail functions along with playing areas for children.

The aquarium has a size of 2000 m^2 and will become a modern, cultural aquarium serving both exploration and education that will stand out as a new Georgian landmark.

6.1 Structural Overview

The complex shapes of the pebbles make the design of the aquarium distinctive and elegant. This complex shape however, is also what makes the structural aspects of the dimensioning process challenging.

The proposal for the structural system of each pebble - if considered separately - could be shell structures, but the fact that the lower pebbles support the upper pebble might result in a different approach.

The client has expressed a wish to use reinforced concrete for the structure and a number of different approaches to this is listed:

- Formwork-cast concrete.

- Sprayed concrete (shotcrete).

- Steelwork frame with concrete fill-in.

In the material selection process factors such as availability, cost and local labour must be considered. It has been expressed from the client that skills in sprayed concrete are locally available.

The aquarium is located directly on the Black Sea coastline in Georgia which means that considerations in regards to corrosion of materials, in this case mainly the reinforcement, must be taken. Sufficient concrete cover in accordance with the Eurocode 2, [16], must be applied.

This report focuses on the structurally complex pebble B highlighted in figure 6.1. The large span and concave parts of this pebble makes it the most complicated structure of the six pebbles when considered separately. All loads acting on this structure are considered including the self-weight and imposed load from the upper pebble. The contact area between pebble A and B is a natural point of weakness and considerations into how the load is transferred through this area will be expressed in part III.
Figure 6.1 highlights the location of pebble B in relation to the remaining building sections of the aquarium.

(a) Top view.

(b) Elevation view.

(c) Perspective.
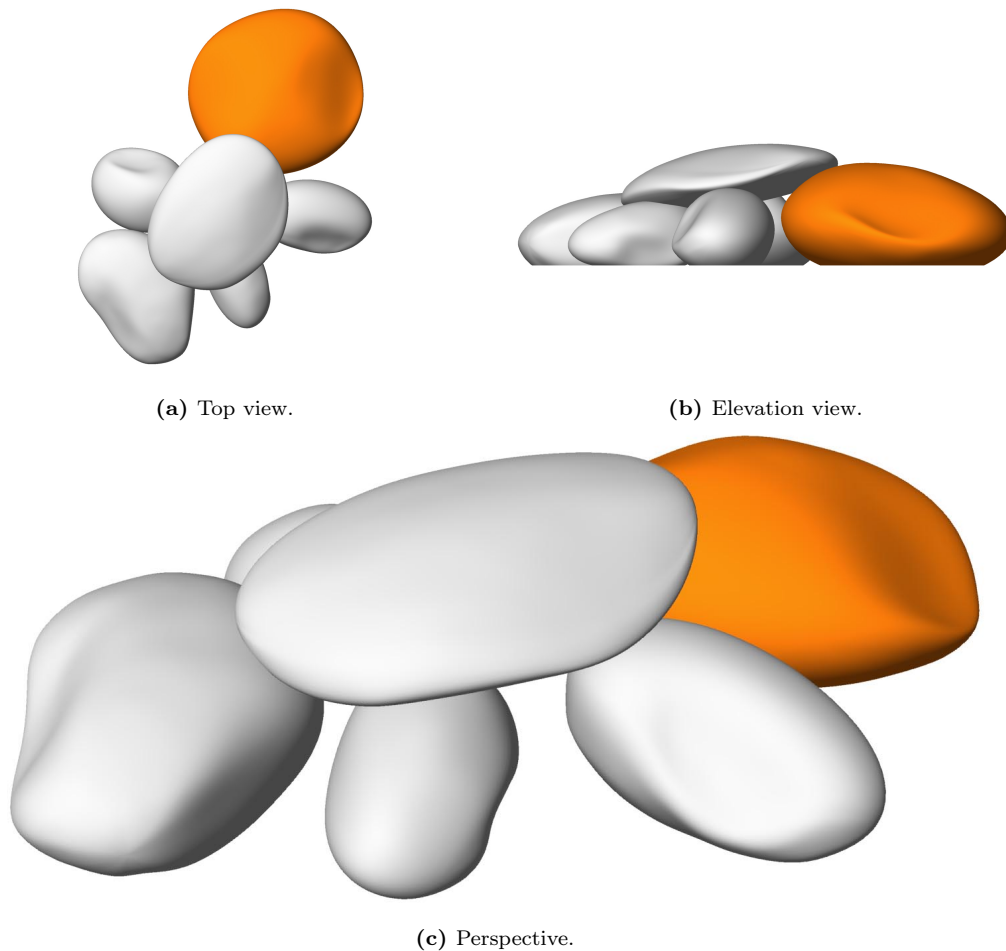
Figure 6.1: Pebble B highlighted.

Pebble B has an approximately circular footprint with a diameter of 30m - 40m and a height of 16,5m. The geometry of pebble B will be examined in greater detail later in the report.

6.2 Project Restrictions

The investigations carried out in the remaining part of this report is subject to the following restrictions:

1. No columns
   It is decided that columns will not be included as a structural solution. This is mainly because of aesthetic reasons but also because this report focuses on shell theory and investigates the thin shell behaviour, which is of less importance if supporting columns are included.

2. Foundation and installations not considered
   The report will not go into detail with the foundation of the construction just as mechanical, electrical and plumbing considerations are left out of the scope of the project.

3. No pretensioning
   Pretensioning is ruled out as a solution in this report mainly as a result of the project description where it is stated that flexural reinforcement is preferred.

4. Entrances not investigated
   Pebble B has two entrances in the surface geometry but these are not included in the investigation and the pebble is treated as a smooth surface. This decision is made mainly to simplify the various investigations but also because it is estimated that the given membrane forces and bending moment around the entrances can be counterbalanced by a strengthening of the cross section around the entrances. A solution to a strengthening of this kind could be hidden steel beams/frames within the concrete cross section. The rendering in figure 6.2 shows the nature of the entrances to the different pebbles.

Figure 6.2: Rendering from the interior of The Batumi Aquarium by Henning Larsen Architects.

[This page is intentionally left blank.]

CHAPTER 7

Tools

The following sections will present six different tools developed in this project in an attempt to clarify the behaviour of the force and stress flow in shell structures. All tools are developed in Grasshopper and can be used for any given shell structure with the output data from Sofistik mentioned in section 1.3. To make the comparison of the different scripts easier all examples of plots from the scripts in the following sections is kept to the case of a hemisphere exposed to a downwards vertical uniformly distributed load over the entire shell surface as illustrated in figure 7.1.
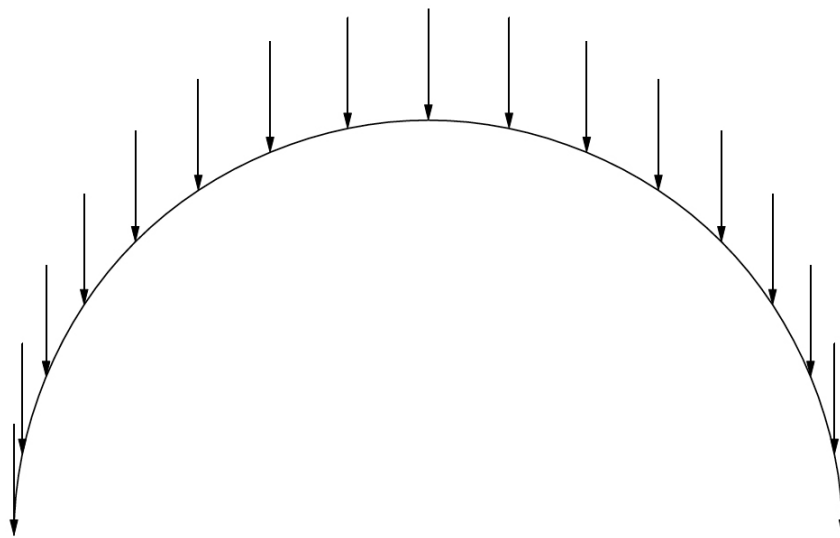
Figure 7.1: Geometry and load distribution for script examples.

7.1 The Geometry Analysis Tool

By dividing a given geometry into a rectangular grid of surface points it is possible to calculate the principal osculation circles in each point. The radius of each circle is evaluated with an adjustable lower limit, all points where both radii exceeds the limit are then represented on the surface.

(a) Rectangular grid of surface points   **(b)** Points where both radii exceeds the limit
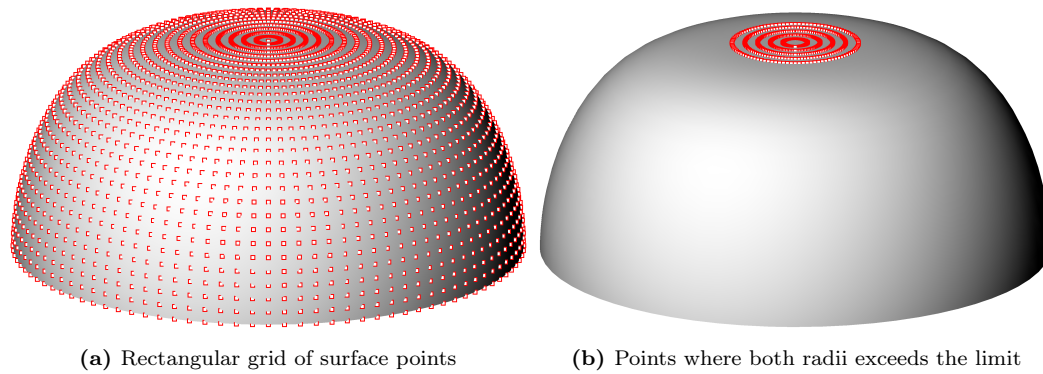
Figure 7.2: The Geometry Analysis Tool

In order to discover planar areas the lower limit for the radii should always be set according to the overall size of the evaluated geometry. In figure 7.2b the lower limit is set to two times the base diameter and therefore relatively planar areas are discovered.

7.2   The Quad Colouring Tool

In an attempt to get a clear overview of the stresses in a given shell structure a tool that differs between quads in tension and quads in compression is developed. The tool needs the geometry data for all quads from Sofistik as well as the local stresses for every quad. Figure 7.3 shows the output of the quad colouring script when set to illustrate the first principal stress σ_I for the top layer of the hemisphere.

(a) Top view.   **(b)** Perspective.
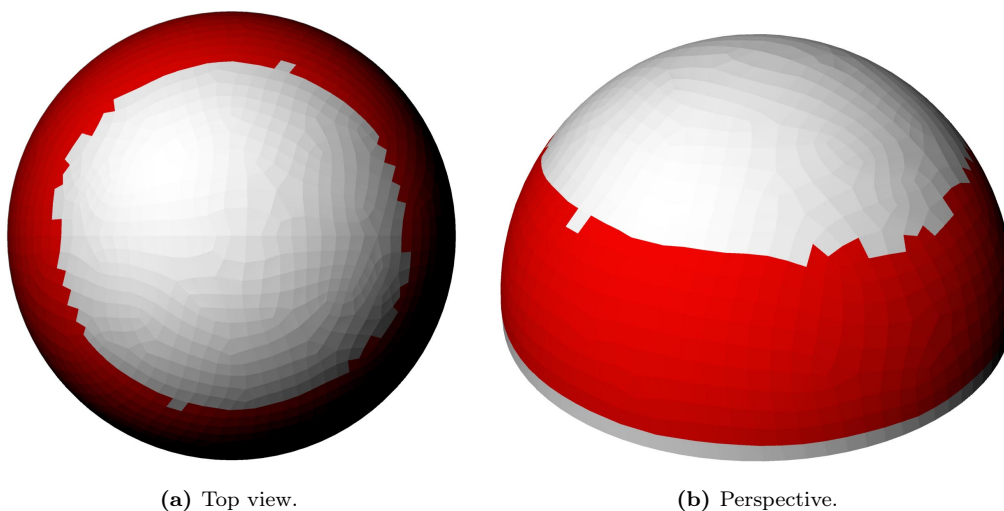
Figure 7.3: The Quad Colouring Tool. σ_I. Top layer.

7.3   The Stress Vector Tool

In continuation of the quad colouring tool it was regarded necessary to have a better overview of the directions of the stresses in addition to the tension/compression differentiation. The inputs are still the geometry data along with the local stresses. The local stresses, σ_X and σ_Y, always act in the local x-direction and the local y-direction respectively while the directions of the principal stresses needs to be calculated according to equation (7.1).

$$tan(2\theta_p) = \frac{2\tau_{XY}}{\sigma_X - \sigma_Y} \tag{7.1}$$

From which the principal stresses can be determined.

$$\sigma_{I,II} = \frac{\sigma_X + \sigma_Y}{2} \pm \sqrt{\left(\frac{\sigma_X - \sigma_Y}{2}\right)^2 + (\tau_{XY})^2} \tag{7.2}$$

It is noted that θ_p is the angle between the local x-direction and the direction of σ_I.
The Stress Vector Tool offers the possibility of choosing between plotting the direction vectors as unit vectors with no regard to the actual size of the stresses and plotting the direction vectors with amplitudes related to the size of the stresses. The two variations are illustrated in figure 7.4 and figure 7.5. Again the case illustrated is the first principal stress, σ_I, for the top layer of the hemisphere.

(a) Top view.

(b) Perspective.
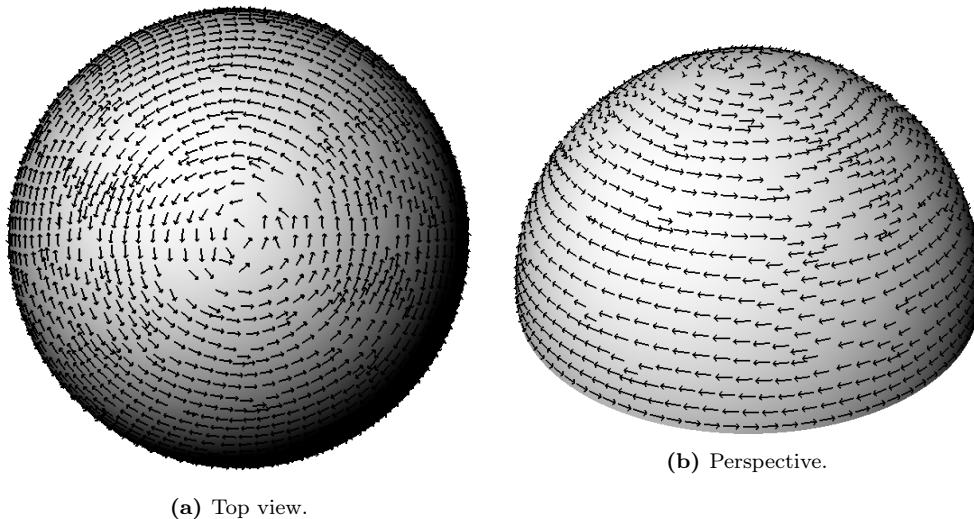
Figure 7.4: The Stress Vector Tool - Unit Vectors. σ_I. Top layer.

(a) Top view.

(b) Perspective.
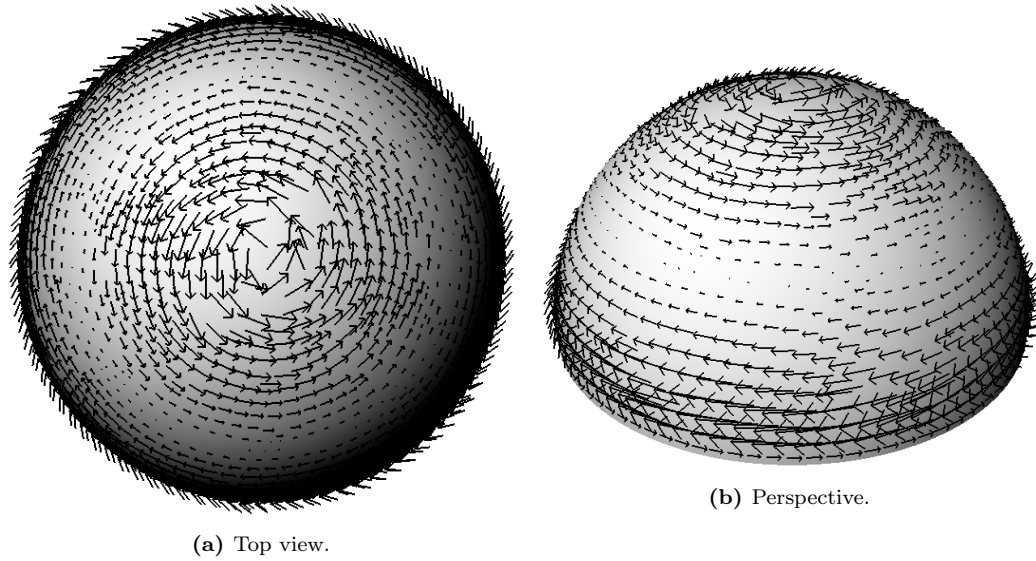
Figure 7.5: The Stress Vector Tool - Amplitude Vectors. σ_I. Top layer.

7.4 The Stress Vector Amplitude Tool

It was found that the stress vector tool introduced in the previous section was informative but confusing and not very clear in differing between tension and compression stresses. A combination of the two tools already introduced was sought resulting in the development of the Stress Vector Amplitude Tool. The tool illustrates the chosen stress as a coloured rectangle perpendicular to the quads on the hemisphere surface. A red rectangle means that the quad is in tension while a green rectangle means the quad is in compression. The height of a given rectangle corresponds to the size of the stress in that quad - relatively compared to the sizes of the remaining stresses in the structure. Figure 7.6 illustrates the graphical output from the Stress Vector Amplitude Tool.

(a) Top view. **(b)** Perspective.
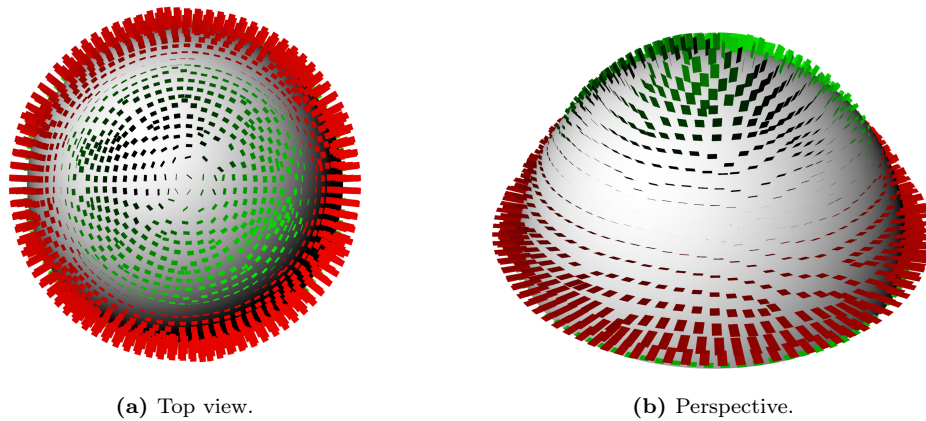
Figure 7.6: The Stress Vector Amplitude Tool. σ_I. Top layer.

7.5 The Principal Stress Trajectory Tool

Finally an attempt to illustrate the so-called principal stress trajectories was carried out. Principal stress trajectories can be described as a contraction of a vector field into paths or lines that illustrate the direction of the sum of the principal stress vectors. Practically in the case of reinforced concrete the principal stress trajectories of a structure describe the optimal path or mesh of reinforcement bars in the structure - if the stress trajectories are reduced to illustrate the contraction of principal tension stresses. A thorough study of principal stress trajectories is not within the scope of this report but the script developed still illustrates the paths of the principal stress and works for any given shell structure that has been investigated in Sofistik. The script offers the possibility of choosing between stress trajectories for tension and/or compression stresses. The target spacing between the trajectories can also be altered within the script. Figure 7.7 shows the stress trajectories for the same hemisphere, load and concrete layer as in the scripts presented earlier in this chapter.
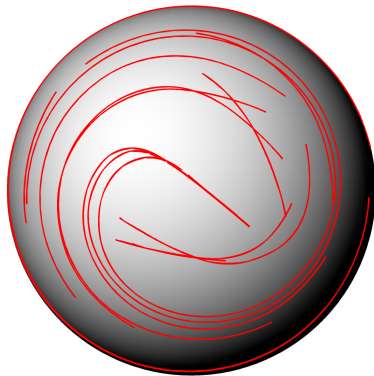
(a) Top view.
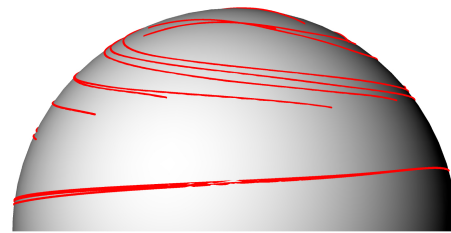
(b) Elevation view.
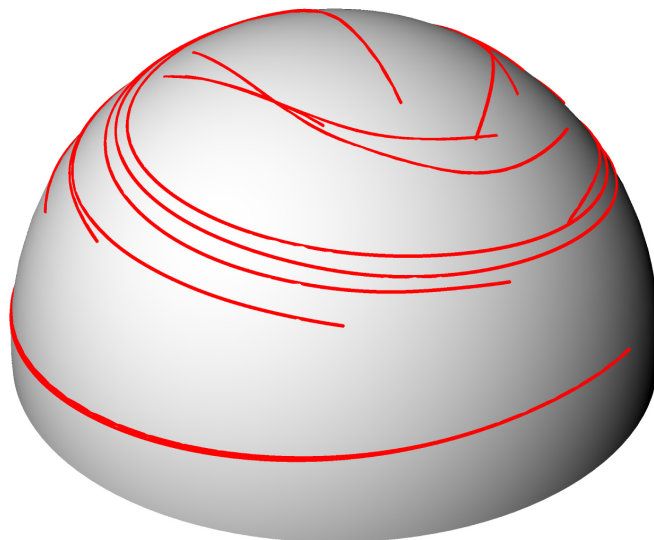
(c) Perspective.

Figure 7.7: The Principal Stress Trajectory Tool. σ_I. Top layer.

7.6   The Cross Section Design Tool

From the previous tools a good indication for placing the flexural reinforcement in an optimum manner is obtained. However, the plot achieved from the principal trajectory tool only indicates a solution for placing the reinforcement in the principal stress direction. In practical the reinforcement is often placed regarding a more uniform mesh, for instance in a orthogonal mesh. This is primary done to ease the structural design and the construction phase. From this assumption the design of the cross sections have been conducted regarding the local cross section forces.

In order to ease the design and construction of a concrete structure as few cross-sections as possible, and still obtain an economical material consumption, is favourable. Therefore, a parametric cross section design tool is developed. The design principals are based on the approach described in section 10.2. The cross-section design is conducted according to design variables such as: *thickness*, *steel yield strength*, *concrete compression strength*, *reinforcement diameter*, *concrete cover* and *minimum* and *maximum reinforcement*.

In figure 7.3 it was seen that almost the bottom half of the reference hemisphere is subjected to tension in the circumferential direction which indicate a need for reinforcement. The cross section design tool calculates, for each quad, the needed numbers of reinforcement bars per meter for both top and bottom layers in local directions. The interval of bars in each direction is divided into four equally segments and the quads are coloured according to the segments.
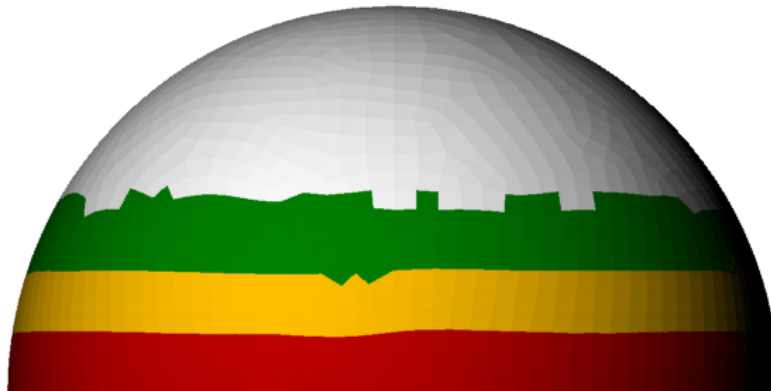
(a) Elevation view.

Figure 7.8: Number of reinforcement bars in local x direction. Top layer.

In figure 7.8 each color represent a minimum of reinforcement bars. White indicates ω_{min} and red indicates the area with the largest needed number of reinforcement bars. Furthermore, indicate the tool if the needed compression zone of the concrete exceeds half of the cross-section thickness.

Hereafter, the design variables and the number of bars in each direction are adjusted to optimise both reinforcement mesh and cross-section thickness.

7.7   Summary

The six different tools are developed en route in order to visualise analysis results and hereby obtain a better understanding of the results. All tools have evolved from different analysis problems within the studies of shell structures. In the remaining sections three tools will be used: The Geometry Analysis Tool, The Principal Stress Trajectory Tool and The Cross Section Design Tool. The remaining tools however, are still included in this chapter due to the fact that they act as predecessors for the three mentioned tools.

[This page is intentionally left blank.]

Structural Optimisation

The main criterion for all engineers or designers hired to execute a task is to come up with at least one feasible design or solution. Traditionally the first idea for a solution or design originates from experience or personal intuition. However it is very rare that this procedure in general will lead to the best solution or design [13].

Over the past 50 years [13] different methods and techniques have been developed in order to obtain the best (optimal) design according to a specific task. Both computational algorithms such as Genetic Algorithms (GA) [17], which has shown to be a very efficient tool for complex problems with many variables, and management procedures such as an integrated design process can be mentioned as improvements to achieve the optimal design. However an optimisation process can often be intangible for the involved parties. Design variables are often many and can be constrained by each other. In figure 8.1, Arora, has tried to summarise the steps of an optimisation design process and the traditional design process.

Step zero, four and five are different from the traditional design process. At first the design variables according to the target optimisation area are identified and sorted by dependencies. A very important step in the optimisation process is number four. At this point the design has to satisfy a target criteria and no longer just a feasible design. The optimisation method in step five is normally based on the target optimisation area, constraints and the overall optimisation process and is facilitated by techniques ranging from a single spreadsheet to involving whole organisations [13].

The optimisation process is often termed as a *sequential search* and characterized by the fact that future trial designs may be generated by using the results of the previous designs [13]. In such a process designers and engineers are dependent on a flexible and reliable method which enables the study of different designs in a relatively short timespan. A method, which from the authors point of view, can be facilitated by parametric modeling techniques and data interoperability between software packages.

However, in practice these different techniques do not always lead to a *global* optimum given that design variables can be governed by subjectivity. Optimising one target area in a system can lead to a negative effect on others. Therefore one could always question a chosen design by the omission of design variables. In the following section the optimisation process in figure 8.1 is applied on the Batumi pebble B in order to conduct an optimisation method.
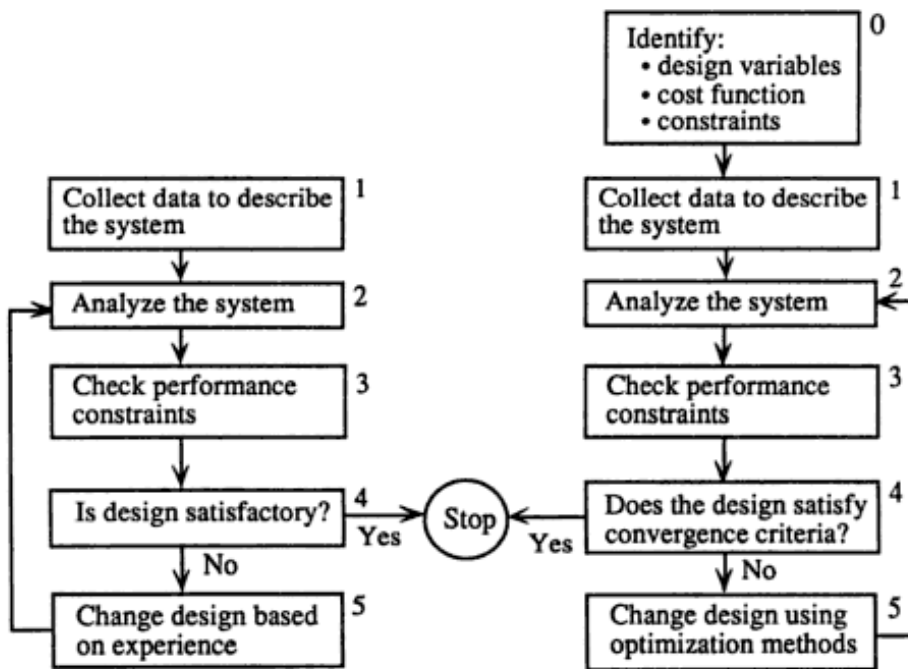
Figure 8.1: Arora's optimisation process [13].

8.1 The Optimisation Process for Batumi Pebble B

As mentioned the design variables for a global optimal design are almost infinite. The case is no different for the Batumi pebble B where different optimisation areas such as: *constructability, modularity, material consumption, design and aesthetics, functional requirements, cost* and *structural performance* all require a set of different design variables. However, even with a set of different design variables, none of the mentioned optimisation areas are independent and therefore can not be optimised without having a potential consequence elsewhere in the design. In figure 8.2 an imaginary and simplified optimisation sequence for pebble B is illustrated.
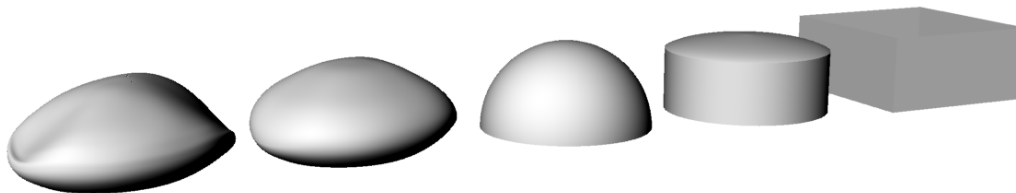
Figure 8.2: Imaginary optimisation trials for pebble B.

The five steps from the initial design to a cube illustrated in 8.2 indicate the extreme case of an optimisation process, where the cube would be picked as the optimal design regarding most optimisation areas except for design and aesthetics and perhaps functional requirements. However, from a clients and architects perspective the design and aesthetics are normally of great importance and should not be neglected. Based on this assumption optimisation areas such as *constructability, modularity, cost* and *functional requirements* will not

be examined. This is done in order to limit the scope of the optimization process conducted in this report.

The target optimisation area in this report will instead be the structural performance of pebble B. The structural performance should be seen in relation to the geometrical shape and preferably result in a shape that facilitates shell structures and still maintains a unique design. The structural performance will be quantified in terms of material consumption of concrete and reinforcement steel. In figure 8.3 the constraints of the optimisation process[1] regarding structural performance and design are illustrated.
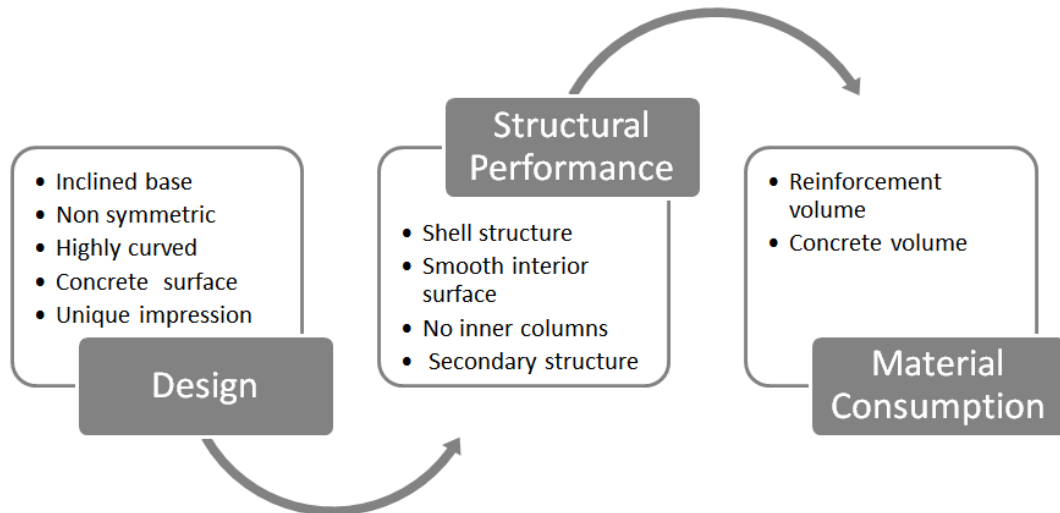
Figure 8.3: Constraints for the different design variable.

The main design variable is hereby the geometry of pebble B whereas the design criteria is the material consumption. By developing an optimisation method where a parametric modelling technique of the geometry is interactive and automated to a large degree with the structural analyses the sequential search is smoothened. A description of the parametric model will be conducted in section 8.2.

8.2 Parametric Model of Pebble B

In accordance with the observations done in part I the optimisation will aim to reduce the concave and planar areas in the upper part of pebble B while the base geometry will remain unchanged. This approach ensures that the optimised geometry is kept close to the aesthetic expression of the originally proposed geometry by Henning Larsen Architects.

To reduce the concavity of the original geometry or even get rid of the concave areas completely a parametric Grasshopper script is developed. The full script can be seen in appendix F.1.

The first step of the script is to make the surface manipulable. This can be done in many ways but for this particular geometry it is estimated that a suitable approach is to make a number of vertical planes cut the geometry and use the resulting intersection curves for further altering. The intersection curves can be seen from figure 8.4.

---

[1]The arrows indicate the flow of the optimisation process.
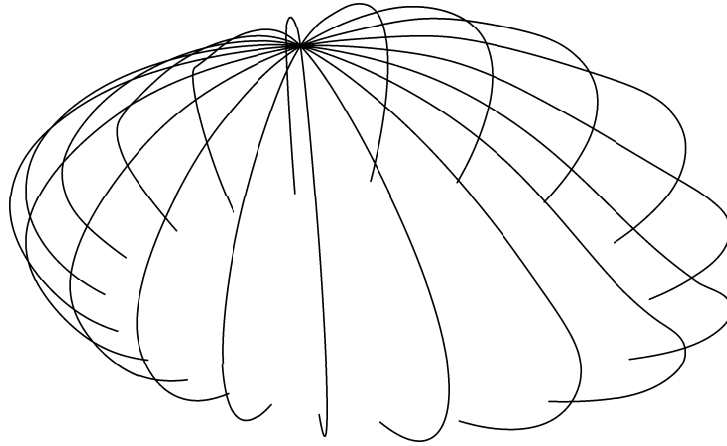
Figure 8.4: Intersection curves for the original geometry.

To fulfil this requirement to keep the optimized geometry close to the original design one of the intersection curves from figure 8.4 is chosen as the reference curve for the further changes made to the surface. In this example the curve seen in figure 8.5 is chosen.
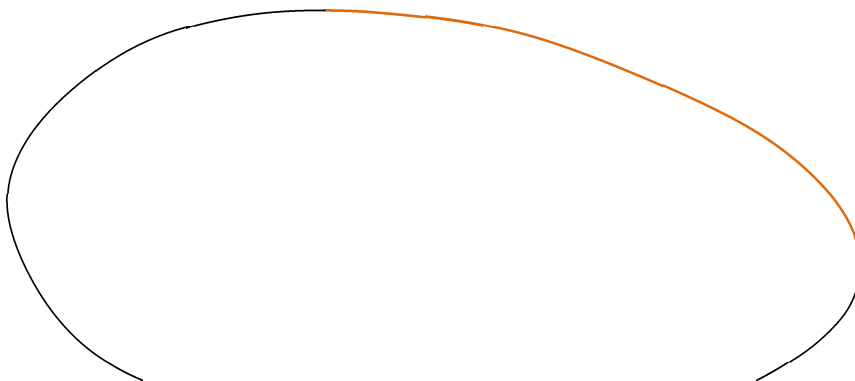
Figure 8.5: Chosen reference curve.

The coloured section of the reference curve will be the reference for the optimisation of the upper part of the pebble B geometry. The part is chosen since it does not contain any concave sections and has a relatively constant curvature along its length. The lower part will not be targeted in this investigation but could be manipulated in the same way as it is the case for the upper part.

When the reference curve is selected the degree of similarity between the upper part of all intersection curves from figure 8.4 and the reference curve from figure 8.5 can be altered. The script works within the input range of zero to one where zero will return the original geometry while one will apply the same curvature as upper part of the reference curve to all upper parts of the intersection curves. Four steps[2] from the concave intersection curve towards the reference curve can be seen in figure 8.6.

Figure 8.6: Varying curve geometries in steps towards the reference curve from figure 8.5.

When all intersection curves are changed into having the same curvature as the reference curve the script can not alter the geometry further. The curves of this geometry - the optimised geometry - can be seen from figure 8.7

---

[2]Input values of *0,25*, *0,50*, *0,75* and *1,00* respectively.
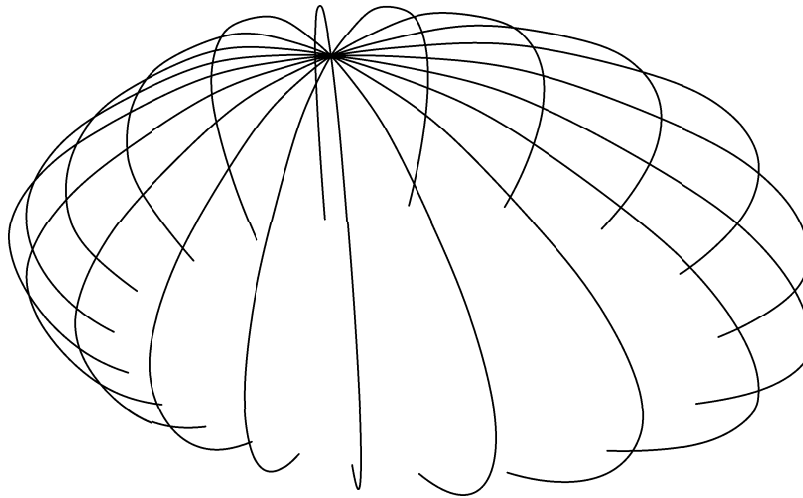
Figure 8.7: Intersection curves for the original geometry.

To compare the two geometries - the original and the optimised geometry - the curves are *lofted*[3] to make continous surfaces ready to export to Sofistik.
The two shell surfaces can be seen from figure 8.8.

(a) Original geometry.   **(b)** Optimized geometry.
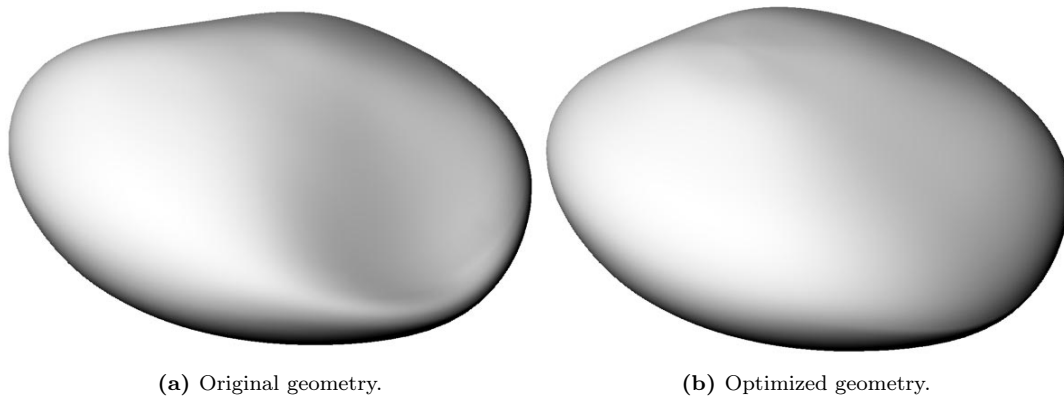
Figure 8.8: The original and optimised geometry.

It is seen from figure 8.8 that the optimisation was successful in regards to minimising the concave and planar areas in the upper part of the structure. The following chapter will verify analytically whether or not this optimisation has resulted in a more efficient shell structure in regards to curvature.

---

[3]A Grasshopper/Rhino command that "drags" a surface over various curves.

CHAPTER 9

Geometry Analysis

As seen from section 5.4 the efficiency of a double curved shell structure is highly related to its curvature. From the investigation in chapter 5 it was observed that small adjustments of the curvature of a shell structure will have a large influence on the membrane forces and bending moments in the shell structure. Figure 5.4 and 5.5 in section 5.4.1 indicate that especially planar areas[1] on a shell structure will experience an increase of bending moments, hence areas with large curvature can be characterised as plates.

In the following sections a method for discovering planar areas on a geometry is presented. The analysis is based on the same conditions as in the investigations of hemispheres in part I and applied on the Batumi pebble B under the assumption that it can be treated as a hemisphere.

9.1   Curvature Analysis

The most common way to perform curvature analyses of geometies is in terms of *Gaussian* curvature where the three classifications; negative, positive and zero makes it possible to classify a geometry or just areas of a geometry as double curved (convex or concave) or single curved (cylindrical). Hereby, the Gaussian curvature makes it possible to analyse the change in curvature of a geometries seen in figure 9.1 where a Gaussian plot of three geometries from section 5.4, hemispheres with a vertex height of 4,5 m, 6,3 m and 7,5 m, has been performed in Rhino. The colour scaling indicates a curvature going from convex (positive) to concave (negative).
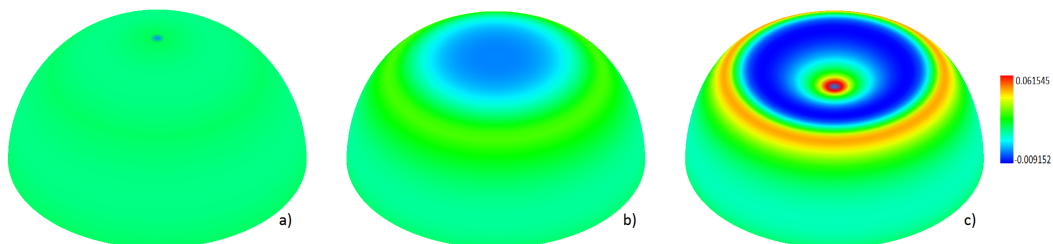
Figure 9.1: Gaussian curvature analyses in Rhino.

[1]Vertex area of geometries with a center height around 5,7 m to 6,3 m.

As seen from figure 9.1 the 'perfect' hemisphere, a, has a positive uniform Gaussian curvature all over the geometry. From the hemisphere with a planar area at the vertex, b, it is seen that the Gaussian curvature is approximately zero at the vertex. The third figure, b, shows all three Gaussian curvature classifications, going from single curved through convex to concave. Besides the change in curvature the plot also shows a quite significant level of discontinuity at the vertex seen as sharp colour changes. This is however due to the revolve technique used in Rhino.

By comparing geometry b and c it is noticed that the light blue area $(K \approx 0)$ appears at both geometries, this is due to the fact that both single curved and planar areas will possess the same Gaussian curvature value as long as the product of the two principal radii are the same. However, a planar area has no spatial stiffness due to the zero curvature. Therefore such areas have the same characteristics as a plate in regards to resisting transverse loads mainly by means of bending and with a flexural stiffness depending greatly upon the thickness of the plate. A reduction of the planar areas is therefore of great value when working with double curved shell structures. Nevertheless it can be very difficult, if not impossible, to predict planar areas only from a Gaussian curvature analysis.

From the previous observations it can be stated that there is a need for a method where both planar areas and geometrically discontinuities are discovered. In the following section a geometrical analysis method will be conducted from the results obtained through the investigation of a hemisphere performed in section 5.4.1.

9.2 Method for Analysing Planar Areas

The principal radii of a planar area is defined as being infinite:

$$R_{C1} = R_{C2} \approx \infty$$

However, from figure 5.4 and 5.5 the deflection increases greatly even before the principal radii have reached an infinitely large value. Therefore the curvature at the vertex of the different geometries is analysed in relation to the deflection at the vertex. By making such a relation it is possible to analyse the maximum principal radii for approximately planar areas and still obtain a reasonable stiffness of the area.
In figure 9.2 the relation between the deflection and the principal radii[2] have been plotted. Only the sequence going from a convex towards a planar upper geometry has been plotted.

---

[2]Due to symmetry R_{C1} and R_{C2} are equal.
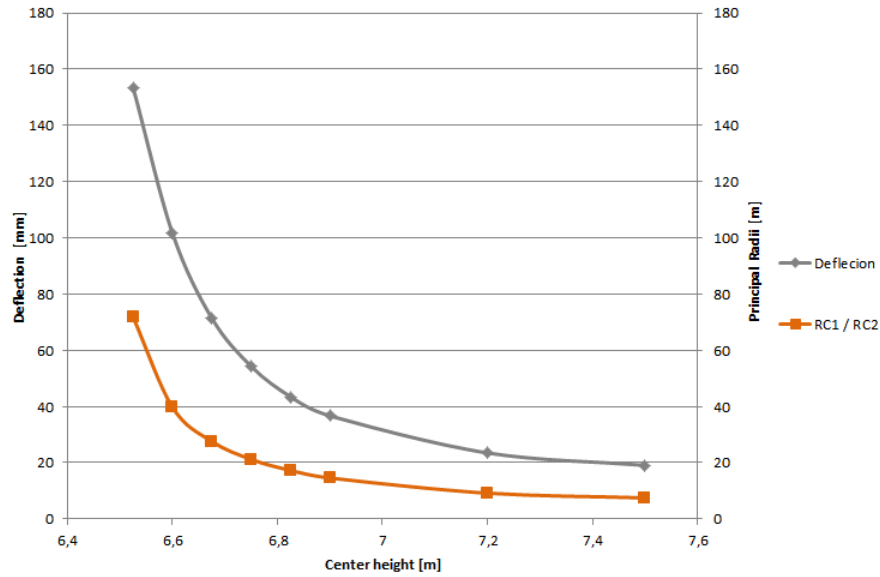
Figure 9.2: Deflection and principal radii for the different hemispheres.

It is seen that the deflection and the principal radii are increased with an almost equal ratio. This observation is only valid for a hemisphere exposed to a transverse loading hence the relation is not valid for a geometry like c in figure 9.1 where both convex and concave areas are present. In this case the deflection of the concave area is governed by the large changes in curvature surrounding the concave area. In table 9.1 the ratios[3] between the principal radii and the deflections are calculated.

Table 9.1: Principal radii and vertical deflection.

Height [m]	$R_{C1}/R_{C2}[m]$	Ratio	Deflection [mm]
7,5	7,5	1	19,09
7,2	9,19	1,2	23,51
6,9	14,6	1,9	36,73
6,825	17,3	2,3	43,45
6,75	21,2	2,8	54,25
6,675	27,6	3,7	71,40
6,6	39,7	5,3	101,58
6,525	71,7	9,6	153,37

Table 9.1 provides an indication of the maximum principal radii of an area in order to obtain a satisfying stiffness. For instance if an area with fairly large principal radii is exposed to a large deflection the stiffness of this area can be improved by reducing the principal radii with a ratio indicated in table 9.1. This statement is as mentioned based on investigations of hemispheres, therefore only valid for geometries that are comparable to the shape of a hemisphere!
From the investigation a maximum principal radii is qualitatively set to 20 meters for a geometry with a shape relatively similar to a hemisphere with a radius of 7,5 meter. Hereby, making it possible to analyse the geometry for relatively planar areas before a structural

---

[3]$R_{1C1}/R_{2C1} = 7, 5/9, 19 = u_1/u_2 = 19, 09/23, 51 = 1, 2$. The hemisphere with a height of 7,5 m is set as the reference geometry.

analysis is carried out. In the following figure the planar areas at the four lowest geometries from table 9.1 and geometry c from figure 9.1 can be seen. The planar areas are visualized by red dots and indicate an area with principal radii exceeding 20 meters.
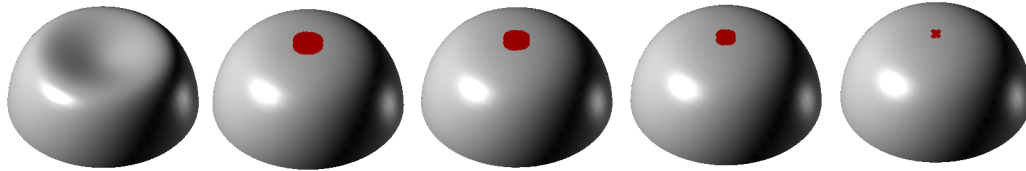
Figure 9.3: Planar areas for different geometries.

Figure 9.3 shows that the planar area around the vertex is increased as the center height is reduced. By combining the method for planar areas and the changes in curvature in terms of Gaussian curvature, figure 9.4, it is possible to perform a detailed geometry analysis and identify areas of special focus before the structural analysis is carried out.
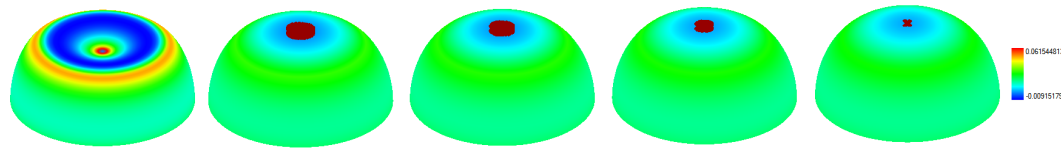
Figure 9.4: Planar areas and Gaussian curvature analysis for different geometries.

A preliminary geometry analysis as in figure 9.4 indicates a discontinuity in the upper part of the first geometry and planar areas in the rest. Both being unfavourable for a shell structure and can result in high bending moments. In the following section the method for analysing planar areas is combined with a Gaussian curvature analysis in order to perform a geometrical analysis of pebble B in the Batumi Aquarium.

9.3   Geometry Analysis of The Original Geometry

The method developed in the previous section is only valid for geometrical shapes comparable to a hemisphere. Figure 9.5 illustrates that pebble B is approximately shaped as a hemisphere with a radius of 17.5 meter.
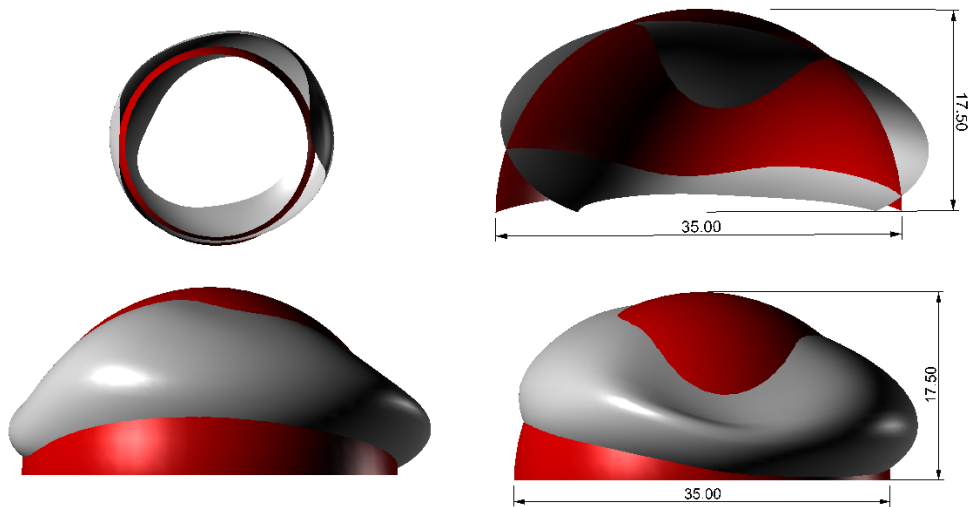
Figure 9.5: Pebble B compared to a hemisphere.

By making the assumption that pebble B has an overall shape of a hemisphere it is possible to analyse the geometry for planar areas. The ratio between the radius of the reference hemisphere (7,5 m) and pebble B (17,5 m) is 2,33. The maximum principal radii for pebble B is then qualitatively determined as:

$$20 meter * 2,33 \approx 47 meter$$

In figure 9.6 areas on the pebble B geometry with principal radii of 47 meter or more is indicated along with the Gaussian curvature analysis.
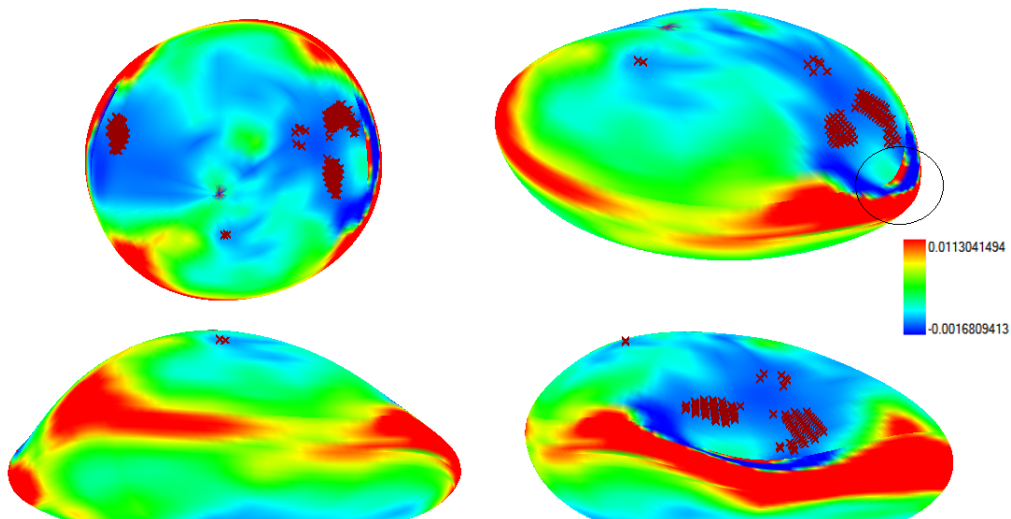
Figure 9.6: Planar areas and Gaussian curvature analysis of the original geometry.

From figure 9.6 the planar areas are located in the two concave areas and in a small area on top of the geometry. Under a transverse loading these areas will experience large bending moments and therefore be unfavourable terms of the stiffness of the shell structure. The Gaussian analysis uncovers changes in curvature around the *belt* of the geometry and especially around the black area where relatively convex and concave areas are located side by side. These areas will affect the overall efficiency in regards to material the consumption

of the shell structure. The optimised geometry is analysed under the same conditions as in section 9.4.

9.4 Geometry Analysis of The Optimised Geometry

As seen from figure 8.8 the upper part of the optimised geometry appears to be convex at first sight. Compared with the original geometry, where unfavourable areas are obvious, no areas at the upper part can visually be determined as weak areas. Therefore, in order to obtain a more detailed evaluation of the optimised geometry it has been analysed with The Geometry Analysis Tool where both planar areas and curvature discontinuity has been investigated. The analysis will be performed under the same conditions as the original geometry, hence a principal radii of 47 meter or larger is indicated together with the Gaussian curvature analysis.
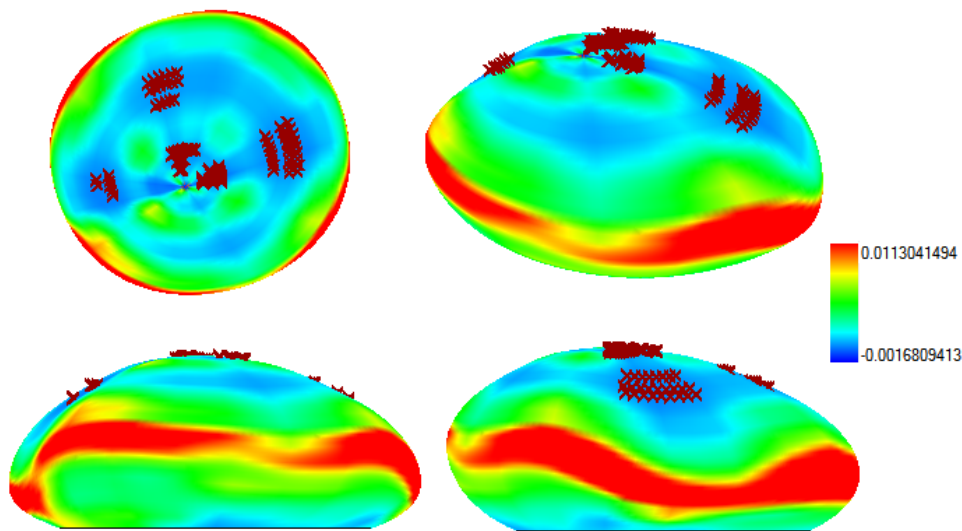
Figure 9.7: Planar areas and Gaussian curvature analysis of the optimised geometry.

In figure 9.7 the geometry analysis uncovers four areas which could not have been predicted by a visual inspection. The upper part still contains some areas which are unfavourable for the shell structure even though it has been modelled based on a reference curve with no discontinuity. This observation indicates some of the difficulties encountered when modelling an ideal geometry in terms of structural performance for a project as The Batumi Aquarium. By comparing figure 9.6 and 9.7 it is seen that two of the planar areas are located almost identically on the two geometries. This indicates that the earlier concave areas are still weak areas at the optimised geometry. The planar area found at the vertex is caused by the used *revolved curve* modelling method if the reference curve has a horisontal tangent at the vertex.

A clear reduction in the change of curvature has been made for the upper part of the geometry. No areas are concave[4] which induce a uniform change in curvature. It is hard to predict from the analysis if the planar areas will have the same consequences for both geometries due to the difference in the curvature of the two geometries. In chapter 12 a structural analysis will be carried out, hereby making it possible to verify the conclusions made in this geometry analysis.

---

[4]Area of dark blue colour.

Theory of Dimensioning

The dimensioning of the shell structure will be conducted by the limit state method, where the two principal states are the ultimate limit state (ULS) and the serviceability limit state (SLS). The design of the reinforced concrete is based on the ULS and the loading corresponding to this state and followed by a check to ensure that the structure is adequate for the SLS. The ULS is carried out under conditions according to a linear elastic behavior whereas the SLS is under conditions according to non-linear plastic behavior. In the following sections the general analysis parameters will be described.

10.1   General Analysis Parameters

In the present section the different analysis parameters such as boundary conditions, local coordinate system, material properties and design requirements for both the linear and non-linear analysis are described. Each analysis will be conducted according to identical conditions and executed in Sofistik. The design requirements will cover both the ULS and SLS analysis and will be determined according to the Eurocode 2, [16].

10.1.1   Boundary Conditions

The boundary conditions have been chosen from the assumption of a degree of movement at the supports in order to obtain the thermal expansions in the concrete. Therefore boundary conditions identical with the boundary conditions for the analytical hemisphere are used, see figure 3.2, and can be described as hinged with free movement in the normal direction of the shell. As mentioned in section 3.2 these boundary conditions facilitate that bending moments at the base are avoided to a large degree. However, a large circumferential force is generated at the base. In Sofistik the boundary conditions are modelled as restraining the finite elements in the local x-direction and the global z-direction.
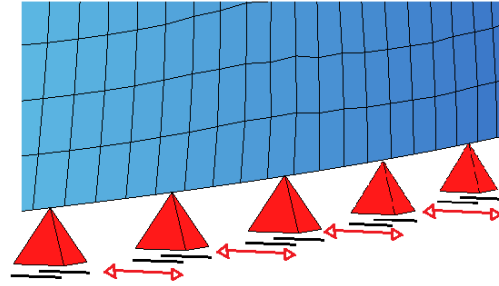
Figure 10.1: Illustration of boundary condition in Sofistik.

Figure 10.1 illustrates the boundary conditions in Sofistik - the dark lines represent restrictions in the local x-direction and free movement (red arrow) in the normal direction.

10.1.2   Material Properties

The main materials for the shell structure are concrete and reinforcement steel. Additionally structural steel is used for the secondary structure. In order to ease the construction phase of the shell structure shotcrete was mentioned as a possible substitute for conventional concrete. In the further analyses conventional concrete will be used since it has similar properties to shotcrete regarding strength, creep and shrinkage[18]. The material properties are listed in table 10.1.2, 10.1.2 and 10.1.2.

Table 10.1: Concrete properties.

Concrete C35		Value
Compression strength	f_{ck}	35 MPa
Tension strength	f_{ctm}	3,2 MPa
Elastic modulus	E	34 GPa
Poissons ration	ν	0,2
Temperature coeff.	ε_t	1e-5 1/K
Self weight		25 kN/m^3
Safety factor	γ_c	1,45

Table 10.2: Steel reinforcement properties.

Reinforcement S550		Value
Yield strength	f_{yk}	550 MPa
Elastic modulus	E	200 GPa
Poissons ration	ν	0,3
Temperature coeff.	ε_t	1,2e-5 1/K
Self weight		78,5 kN/m^3
Safety factor	γ_c	1,2

Table 10.3: Structural steel properties.

Steel S235		Value
Yield strength	f_{yk}	235 MPa
Elastic modulus	E	210 GPa
Poissons ration	ν	0,3
Temperature coeff.	ε_t	1,2e-5 1/K
Self weight		78,5 kN/m^3
Safety factor	γ_c	1,2

10.1.3 Local Coordinate System

It is verified that the local coordinate systems of the meshed shell structure is in accordance with the theoretical local coordinate systems of a shell of revolution - horizontal x-axis and vertical y-axis.
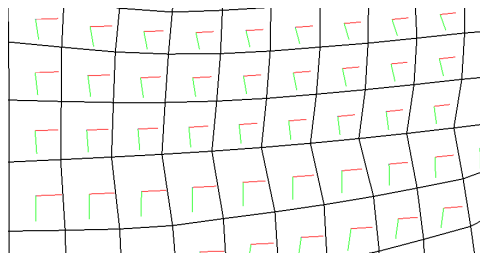
Figure 10.2: Close-up of local coordinate systems (Red arrow: local x-direction. Green arrow: local y-direction).

10.1.4 Design Requirements

According to Eurocode [16] the basic requirements, besides *structural resistance*, are adequate resistance in: *Serviceability, durability, exposure to fire* and events such as: *Explosion, impact* and *human errors*. Furthermore the structure should have a working life in accordance with the usage of the structure. Due to the limitations of the report and a main focus on the geometrical and structural optimisation only, some of the requirements have been examined. Table 10.4 shows the different requirements considered for the structure.

Table 10.4: Design requirements for The Batumi Aquarium.

Requirement	Criteria
Structural resistance	$\sigma_{Ed} \leq \sigma_{Rd}$
Maximum deflection	30mm
Crack width in concrete	0,3 mm
Concrete cover	35 mm

Finally, The Batumi Aquarium is categorised as CC3, High Consequence Class, due to the fact that it is used for exhibitions and possibly holds a lot of people. Regarding requirements for durability, fire and robustness no further considerations will be made.

10.2   The Linear Analysis Approach

For the shell structure a linear analysis will be conducted in Sofistik according to the loads and load combinations described in chapter 11. Regarding the secondary structure a linear analysis will be performed in Robot. The initial reinforcement design will be performed by the *Cross Section Design Tool* presented in chapter 7 according to the section forces from Sofistik. The design is based on the principle of traditional orthogonal plate reinforcement. A rectangular stress-strain relationship is used to idealise the actual stress distribution and the use of the simple stress-strain relationship will result in an extra conservative solution, hence higher consumption of resources. The amount of reinforcement is calculated under the circumstance of pure bending with a cracked cross-section, hereby ignoring the tension zone in the concrete. Furthermore, any compression reinforcement is ignored which eases the calculations and gives an extra safety margin. In the case of membrane tension forces the contribution is added by superposition. The needed reinforcement is calculated for each quad element in the geometry. Design equations implemented in the tool are listed below.

$$\mu = \frac{M_{Ed}}{bd^2 f_{cd}} \tag{10.1}$$

$$\omega = 1 - \sqrt{1 - 2\mu} \tag{10.2}$$

$$A_s = \omega \frac{bd f_{cd}}{f_{yd}} \tag{10.3}$$

$$A_{s.tot} = A_s + \frac{N_{Rd.tension}}{fyd} \tag{10.4}$$

Requirements regarding a minimum reinforcement is determined by the maximum spacing ($s_{max,slabs}$) of the reinforcement and is *2h* or *250mm* in both directions, this is due to the assumption that the shell structure is categorised as a two-way slab. The upper boundary for a maximum amount of reinforcement in the cross section is set to ω_{bal}[1] . Under this condition the failure occurs with yielding of the tension steel and crushing of the concrete at the same time and is described as a *balanced failure*. Both requirements have been implemented as restrictions in the design tool.
The shear capacity of the shell structures will be performed conservatively under the assumption of a non-reinforced concrete cross section. The shear stresses should fulfil:

$$v_{Ed} \le 0,5 \cdot v_v \cdot f_{cd} \tag{10.5}$$

Where v_{Ed} is the shear stress and v_v is the shear efficiency factor[10].

10.3   The Non-Linear Analysis Approach

A non-linear analysis of the structure, based on the materials non-linearity, has been performed in Sofistik. The analysis is based on an iteration process where every step determines

---

[1]$\omega_{bal} = 0,483$ for f_{yk} =550MPa and C35 concrete.

the displacement and stresses. It is checked whether plasticising, cracks or any other non-linear effects have occurred in any of the quad elements. The stiffness of quad elements where second-order effects have occurred are reduced in the following step and the initial loading is increased with a load referred to as the *residual forces*[2] of the structure in Sofistik. The analysis is performed according to the standard setup in Sofistik and the different parameters are listed in table 10.5.

Table 10.5: Design parameters for non-linear analysis.

Design Parameter	Value	
Creep Factor	ε_c	2
Shrinkage Coefficient	ε_s	3e-4
Tensile Strength Concrete	f_{ctd}	1.55 MPa
Tensile Strength Reinforcement	f_t	620 MPa
Iterations	90	

For the non-linear analysis in SLS the following requirements are examples of what can be of interest:

- Deformation.

- Crack width.

- Concrete compressive stresses.

- Reinforcement steel stresses.

However, only in a complete analysis all factors will be examined and specified in detail. In this case the analysis of the structure will be carried out only according to the requirement of a maximum deflection of 30 mm. Results in regards to the remaining requirements will be specified but not further targeted.

---

[2]The residual forces are the forces which have not been balanced by the internal forces.

CHAPTER 11

Loads

This chapter will present the loads acting on pebble B and explain how the shell geometry is subdivided into areas according to these loads in an attempt to simplify the following finite element analysis. Finally the basic load combinations according to [15] will be explained and a simplified load combination for the remaining structural dimensioning in this report will be presented.

11.1 Self Weight

The self weight is based on [15] and acts in the global z-direction along the geometry of pebble B. The self weight is applied through Sofistik where the standardized density of reinforced concrete is set to $25\mathrm{kN/m}^3$.

11.2 Imposed Load

The analysis setup for this assignment will not include any imposed load on the shell structure. Imposed loads from i.e. ventilation, lighting and other installations are not considered. The reaction from the self weight and imposed load from pebble A that is supported by pebble B will be treated in Part 3.

11.3 Snow Load

The snow load is based on [15]. The assumptions presented in the Danish National Annex are used and the characteristic snow load is set to a value of $0{,}9kN/m^2$. The snow load is only applied to the section of the roof where the slope is less or equal to an angle of 60 degrees. The Danish National Annex proposes two different load distributions as illustrated on figure 11.1: An evenly distributed load and a triangulated load distribution. The snow load in this analysis is simplified to only incorporate the evenly distributed load.
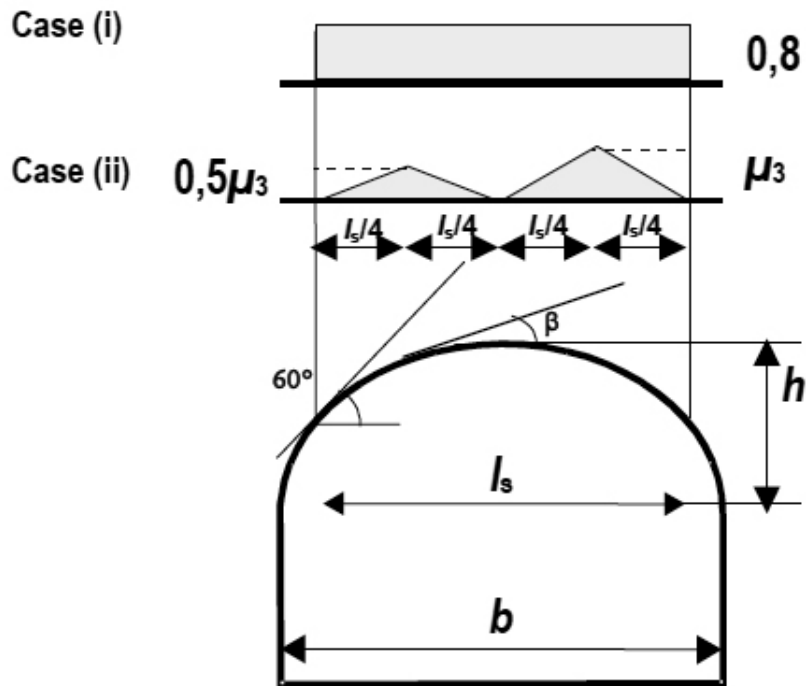
Figure 11.1: Illustration of snow load on cylindrical roofs. [15]

The resulting snow load is then found from the following expression:

$$S = \mu \cdot C_e \cdot C_t \cdot s_k \tag{11.1}$$

C_e is chosen to be 0,8 for windswept topography, since The Batumi Aquarium is on the coastline, as well as the thermal coefficient C_t.

$$S = 0,8 \cdot 0,8 \cdot 1 \cdot 0,9 kN/m^2 = 0,58 kN/m^2 \tag{11.2}$$

Figure 11.2 shows the zone where the snow load is acting on the geometry of Pebble B.
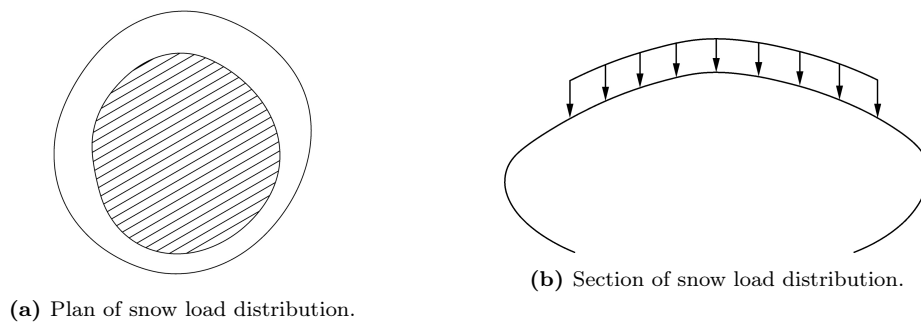
(b) Section of snow load distribution.

(a) Plan of snow load distribution.

Figure 11.2: Distribution of snow loads.

11.4   Wind Load

The wind load is applied in accordance with the [15] section 7.2.8 regarding vaulted roofs and domes. The geometry of pebble B is treated as an axisymmetrical dome roof supported by vertical walls. This is a very rough assumption but the best possible analytical solution to the wind load acting on the geometry presented in the Eurocodes. Conservatively the wind is assumed to act from all directions neglecting the area of pebble B covered by the atrium in the center of all pebbles.
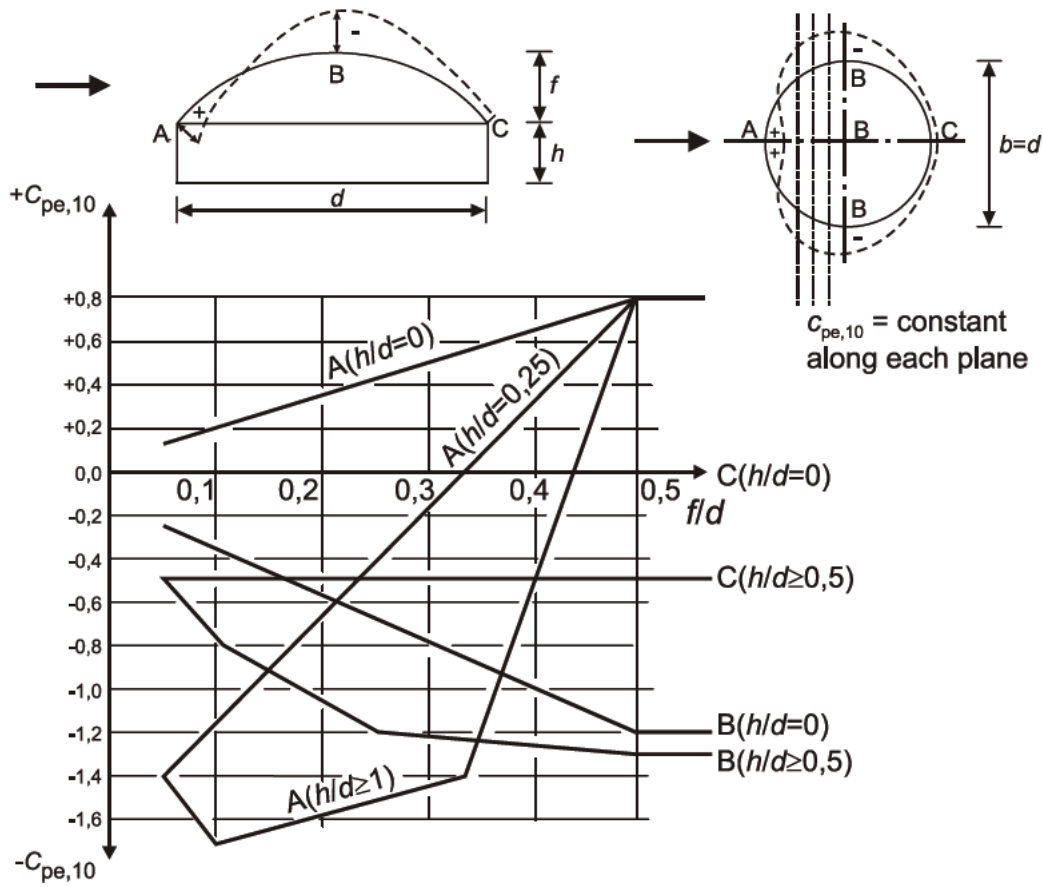
Figure 11.3: Illustration of snow load on cylindrical roofs. [15]

The external wind pressure acting on the different zones of pebble B are found from the expression:

$$w_e = q_p(z) \cdot c_e \tag{11.3}$$

The peak wind velocity is found to be 1,5 kPa. Figure 11.4 shows an overview of the varying external pressure coefficients for the wind load acting on the different zones on the structure.

(a) Vertical section of distribution of wind loads.

(b) Plan of wind load distribution - upper part of Pebble B.

(c) Plan of wind load distribution - lower part of Pebble B.
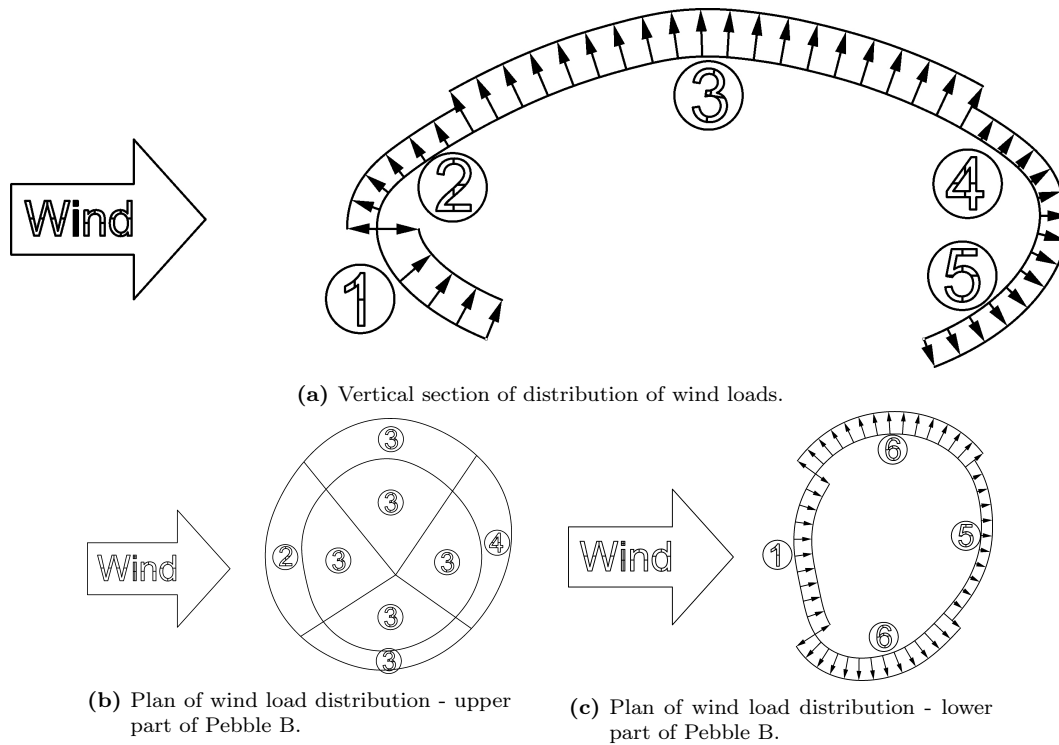
Figure 11.4: Distribution of wind loads.

Table 11.1 presents the values of the wind pressure coefficients:

Table 11.1: Wind pressure coefficients - directions are seen from figure 11.4

Zone	1	2	3	4	5	6
Coefficient [C_{pe}]	1,2	0,85	1,35	0,7	0,75	1,5

11.5   Thermal Expansion

Finally temperature changes will cause the concrete to contract and expand resulting in additional normal stresses in the cross sections. The strains experienced are calculated from the following expression.

$$\varepsilon = 10^{-5} \cdot \Delta T \tag{11.4}$$

Where ΔT is the difference in temperature to which the structure is exposed. The temperature difference is conservatively set to 40 degrees.

11.6   Subdividing the Shell Surface

To apply the above mentioned loads the shell geometry of pebble B needs to be subdivided into relevant zones. In an attempt not to make the division of zones too comprehensive a

generalized approach with nine zones as shown on figure 11.5 has been carried out. The nine zones comply with the application of snow and wind loads as described above to an acceptable degree.

(a) Top View

(b) Perspective

(c) Front View

(d) Right View
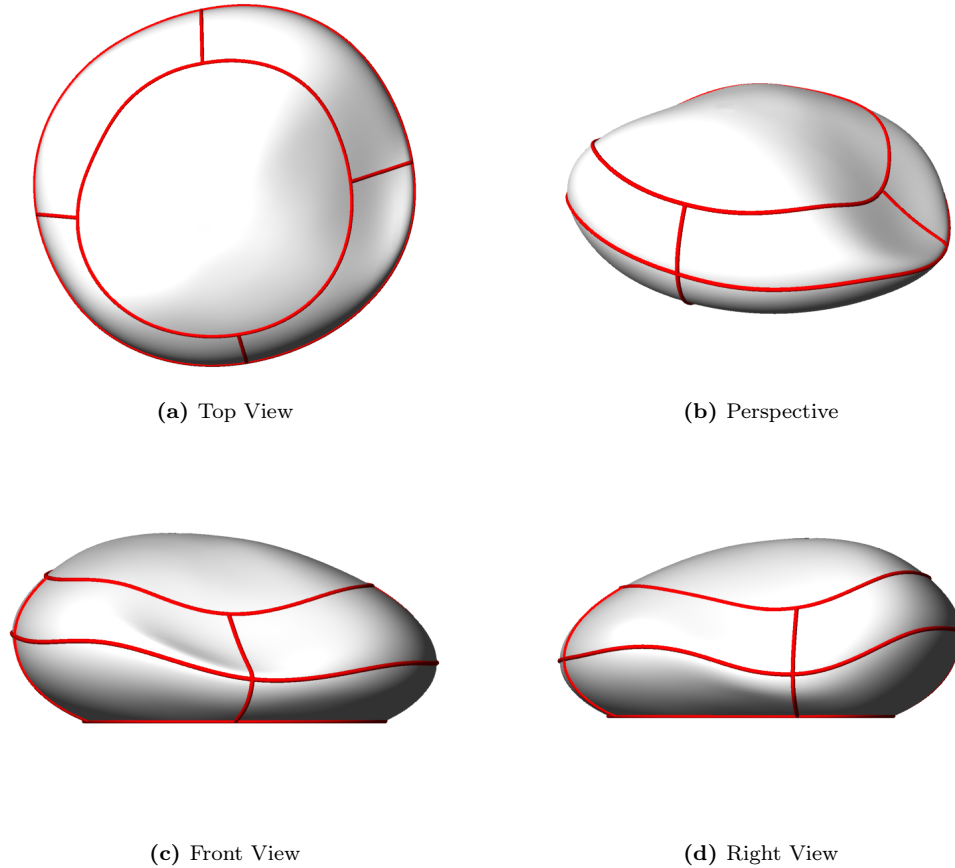
Figure 11.5: Subdivision of shell surface.

11.7 Load Combinations

Since no imposed loads are applied in this analysis the three main load combinations are dominating snow load, dominating wind load and dominating self weight. Since the wind load acts as both pressure and suction along the geometry the load combinations with dominating snow load and dominating self weight should also be investigated in the case where the wind load is left out.

Table 11.2: Load Combinations

	Permanent Loads		Snow Load	Wind Load
	$[G_{k,sup}]$	$[G_{k,inf}]$	$[S_k]$	$[V_k]$
Snow Load Dominating	$1{,}0K_{FI}$	$0{,}9$	$1{,}5 \cdot K_{FI}$	$1{,}5 {\cdot} 0{,}3 \cdot K_{FI}$
Wind Load Dominating	$1{,}0K_{FI}$	$0{,}9$	0	$1{,}5 \cdot K_{FI}$
Self Weight Dominating	$1{,}2$	$1{,}0$	-	-

Of course numerous load combinations could be thought of including asymmetrical loads

and imposed loads as mentioned earlier.

11.8 Simplified Dimensioning Load Combination

As mentioned before the wind load will in all cases result in an upwards suction on the upper part of the shell. This upwards surface load will always act favourably in combination with the self weight, but never change the direction of the resulting distributed loads when the self weight and the wind load is combined. Therefore the wind load on the upper part of the structure is left out of this simplified load combination which will work as a guideline for dimensioning the structure. This approach is a very rough generalization but will be used as a reference example for the analysis and graphical tools developed and described later in the report. This approach is considered acceptable since a more detailed approach to the wind load would require testing the structure in a wind tunnel (or another practical approach) which is not within the scope of this report.

By the use of the favourable/unfavourable argumentation the simplified dimensioning load combination which will be used throughout the remaining part of this report will be the combination of dominating snow load with the downwards suction from the wind load all along the lower part of the structure as illustrated on figure 11.6. Realistically the wind load would never work in all directions at the same time but again in combination with the snow load the pressure on the side of the structure where the wind acts would act favourably against the self weight and the snow load.
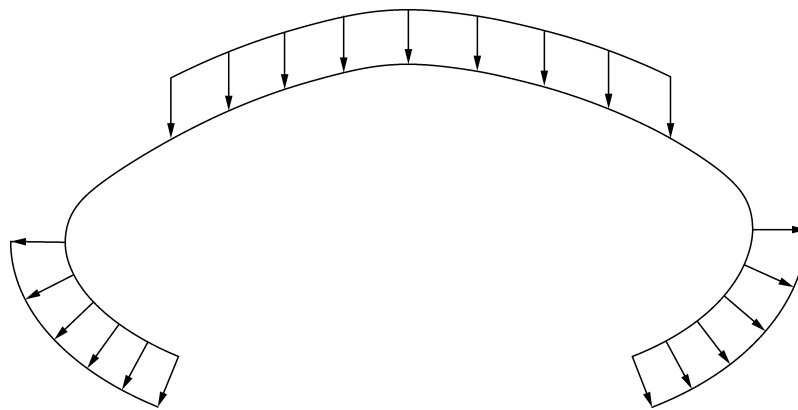
Figure 11.6: Section illustrating the simplified wind distribution and snow load which work as the reference load combination for the remaining part of the report.

CHAPTER 12

Structural Analysis

This chapter presents an analysis of the original geometry and the optimised geometry of pebble B. The structural analysis will be conducted in regards to the loads and load combinations presented in chapter 11. Section 12.1.2 of this chapter contains a linear analysis performed in Sofistik and The Cross Section Design Tool. The section force distributions, theoretical cross section areas and corresponding cross section attributes will be presented. In section 12.1.4 a non-linear analysis is carried out according to the approach described in section 10.3, the deflection plot and results for the SLS requirements will be presented. The optimised geometry will be dimensioned by the same procedure in section 12.2.2 and section 12.2.4 respectively. Finally in section 12.3 results of the structural analysis will be compared according to the design criteria of material consumption.

The shear capacities of the shell structures are not exceeded. The shear capacity check can be found in appendix B.1.

12.1 Dimensioning the Original Geometry

The undeformed and deformed meshed geometry from Sofistik can be seen in figure 12.1. The deformation shape is scaled and can only be used as an intuitive representation of the behavior of the structure.

(a) Undeformed mesh.   (b) Deformed mesh.
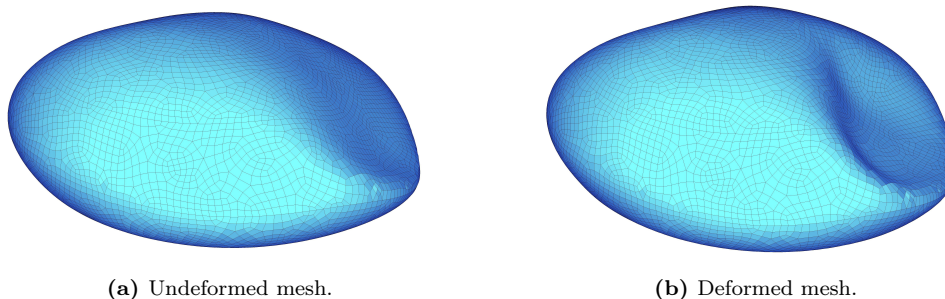
Figure 12.1: The original geometry meshed. Deformation scale factor: 100.

As expected the largest deflection occurs in concave areas and in areas of large curvature discontinuity on the geometry. The meshed geometry shown in figure 12.1 contains 8920

quad elements.

12.1.1 Applied Loads

The shell structure is exposed to self weight, snow load and wind load. The areas where snow loads and wind loads are applied are illustrated on figure 12.2 along with the respective load values. The behaviour of the snow and wind load is described in further detail in chapter 11.
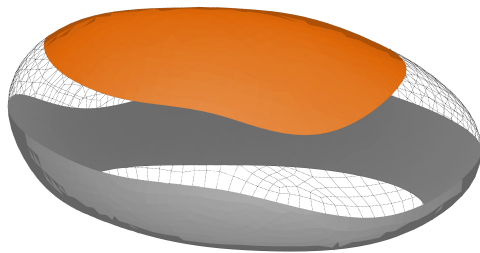
Load	Intensity	Area
Snow Load	0,58 kN/m^2	723 m^2
Wind Load	1,5 kN/m^2	900 m^2
Self Weight	3,75 kN/m^2	3056 m^2

Figure 12.2: Load zones and values.

The size of the self weight stated in the table above is based on an estimated uniform cross section height of 0,15 m and a density of the reinforced concrete of 25 kN/m^3.

12.1.2 Linear Analysis Results

The following section will present the section forces in the structure when exposed to the above stated loads and conclude whether or not the distributions are in accordance with what could be expected from a geometric analysis as conducted in section 9.3. The section forces are obtained from a linear analysis in Sofistik.

The section force distributions and especially the understanding of these is important when implemented in the *The Cross Section Design Tool* to apply appropriate cross sections to the structure in ULS.

12.1.2.1 Bending Moment - X

The bending moment distribution in the local x-direction can be seen from figure 12.3. Values are averaged within the respective quad elements.
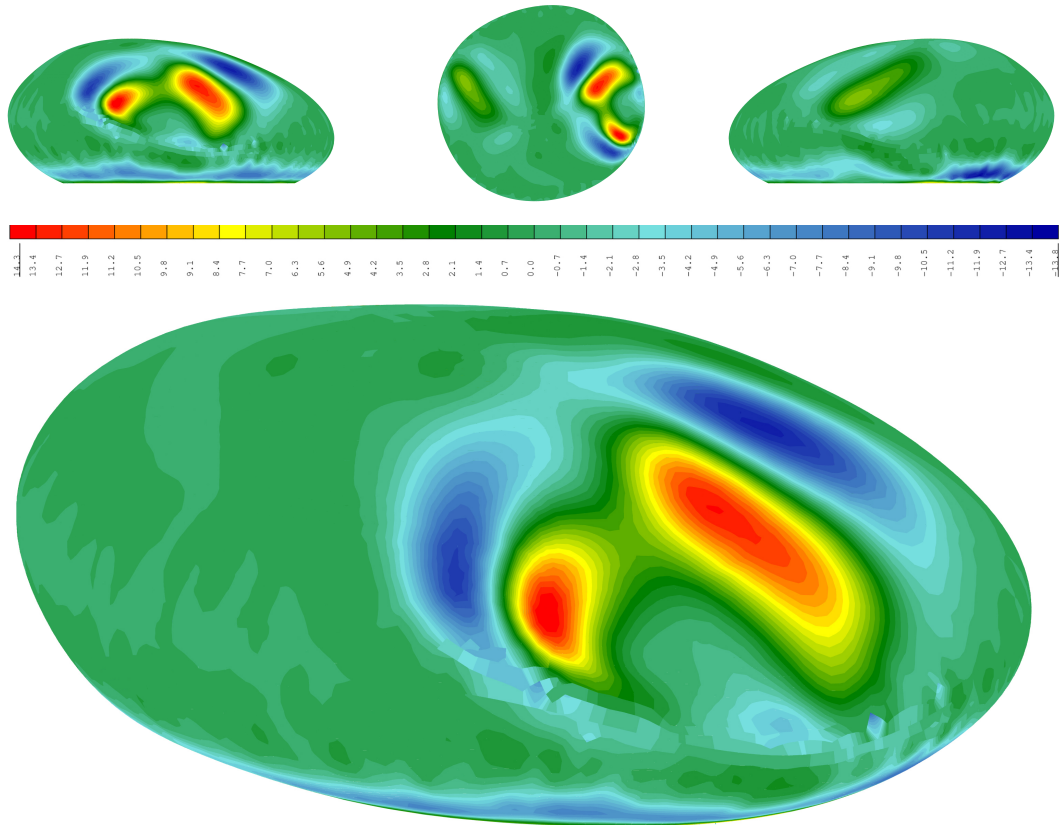
Figure 12.3: Distribution of bending moments. X-direction.

The largest bending moments in the local x-direction occur in the same areas as for the deflection of the structure due to the low flexural stiffness of a thin shell. It should be noted from figure 12.3 that the largest bending moments are located in relatively small areas - the concave areas. However, by comparing figure 9.6 and figure 12.3 it is seen that positive bending moments occur in three areas as predicted in section 9.3. Previous investigations showed that such areas affect the overall efficiency of the shell structure negatively. The negative moment at the edge and the positive moment in the center of the planar area is also in accordance with what could be expected from a traditional plate/beam theory approach. Large bending moments are found around the lower boundaries due to the inclination of the lower part of the structure.

12.1.2.2   Bending Moment - Y

The bending moment distribution in the local y-direction can be seen from figure 12.4. Values are averaged within the respective quads elements.
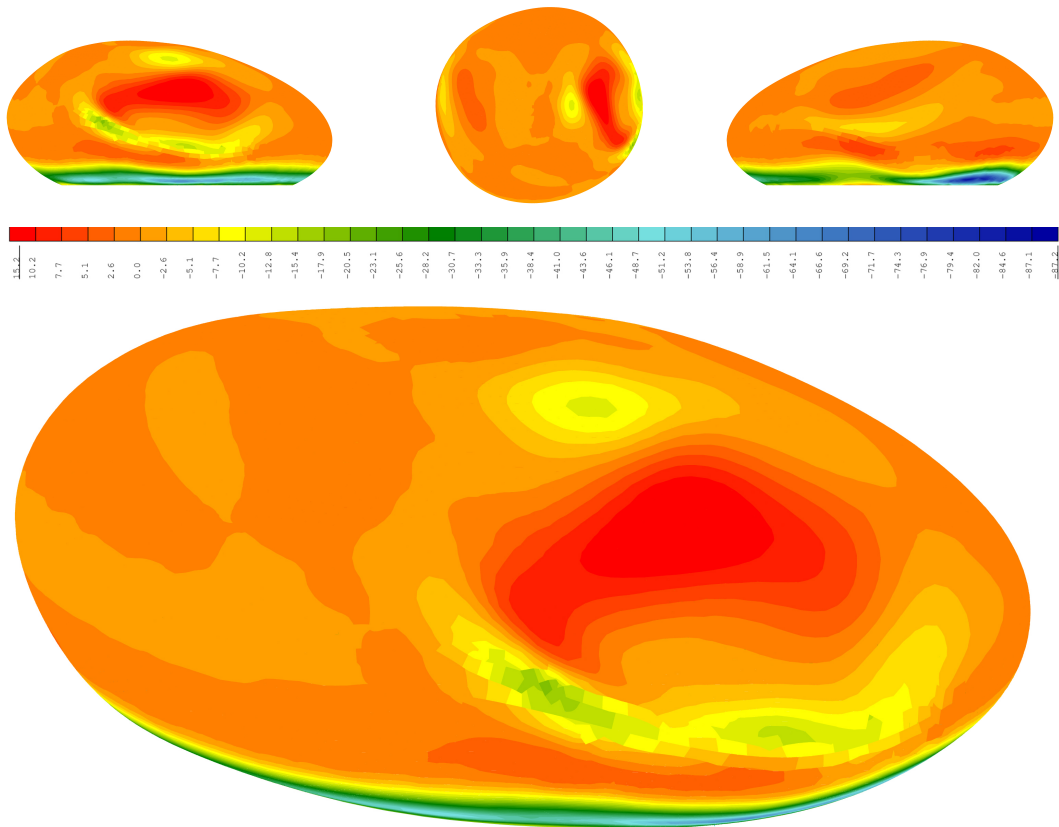
Figure 12.4: Distribution of bending moments. Y-direction.

As seen in figure 12.4 the bending moments in the local y-direction follow the same pattern as observed for the x-direction. Maximum values occur in the concave areas and around the base. It is interesting to compare the distribution of M_x and M_y to see that the negative values of both directions cover complementary areas at the edge of the large concave area which means that the second principal moment should cover the entire edge of the concave areas, which is actually the case as seen in appendix A.1.5. The planar areas in the middle of the concave areas are again subjected to positive bending moments - verifying the plate characteristics.

12.1.2.3   Membrane Forces - X

The membrane force distribution in the local x-direction can be seen from figure 12.5. Values are averaged within the respective quad elements.
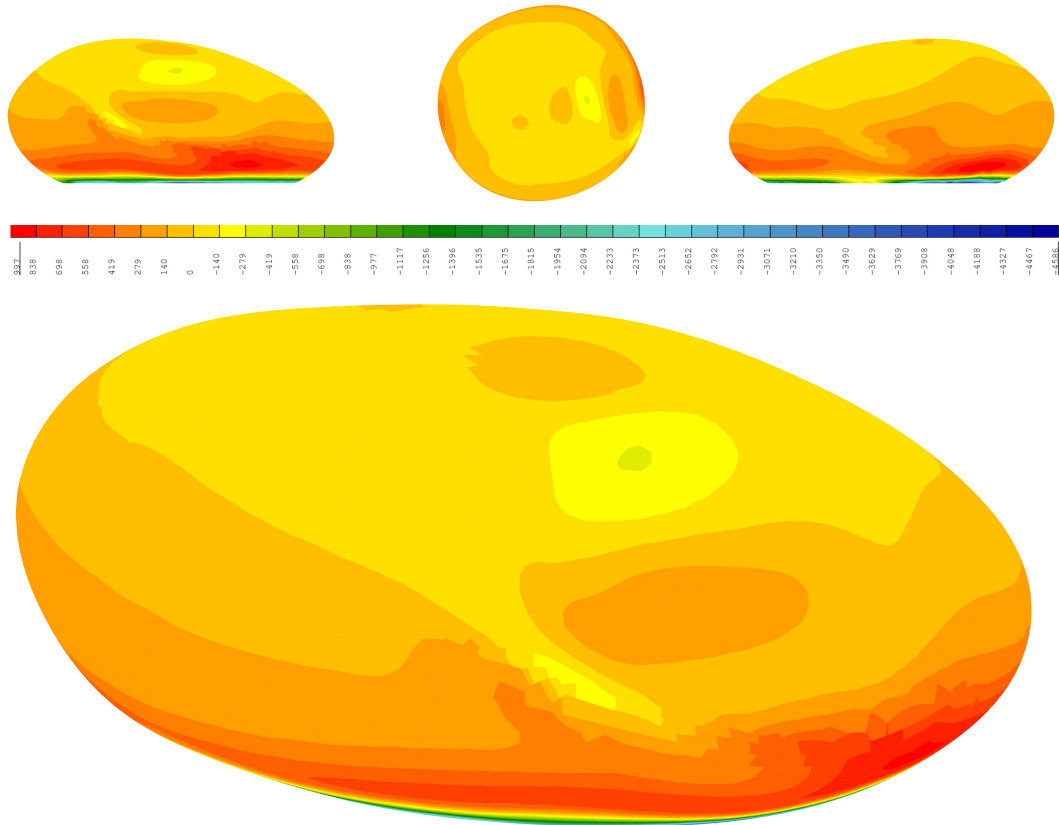

Figure 12.5: Distribution of membrane forces. X-direction.

The compression force in the circumferential direction at the supports might seem extremely large in comparison with the values of the remaining section forces but is actually in accordance with the membrane theory presented in section 3.2.
The proportion between the very large compression force and the remaining membrane forces in the local x-direction presented in figure 12.5 distorts the distribution plot but if studied closely it is seen that the structure experiences negative membrane forces in the upper part of the structure and a positive membrane force in the lower part which is also in accordance with the hemisphere theory. The horisontal component caused by a change in direction of the in-plane membrane forces at the *belt* generates large tension forces in the lower part of the geometry as seen in the figure 12.5.

12.1.2.4   Membrane Forces - Y

The membrane force distribution in the local y-direction can be seen from figure 12.6. Values are averaged within the respective quad elements'.
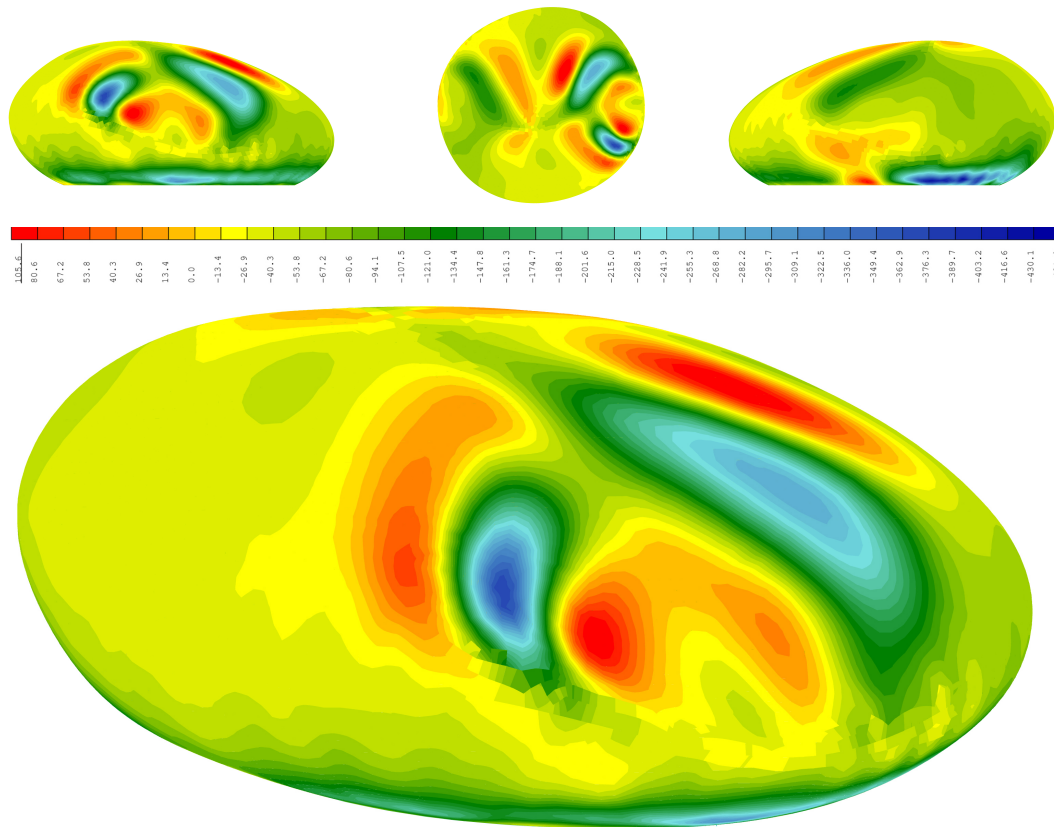

Figure 12.6: Distribution of membrane forces. Y-direction.

The membrane force distribution in the local y-direction should theoretically[1] be negative and decrease going from the supports to the vertex. However, it is also observed that the membrane forces are highly related to the curvature discontinuity especially going from convex to concave. By comparing figure 9.6 and 12.6 it can be stated that when the operational sign of the Gaussian curvature changes, the membrane forces in the y-direction is affected.

---

[1]Axisymmetrically loaded hemisphere.

12.1.2.5 Extreme Section Forces

Table 12.1 sums up the extreme values of the bending moments for the original geometry as seen from the previous section force distributions.

Table 12.1: Extreme values of the bending moments - original geometry.

$M_{x,max}$	$M_{x,min}$	$M_{y,max}$	$M_{y,min}$
14,3 kNm	-13,8 kNm	15,2 kNm	-87,2 kNm

Furthermore the extreme values of the membrane forces are listed in table 12.2

Table 12.2: Extreme values of the membrane forces - original geometry.

$N_{x,max}$	$N_{x,min}$	$N_{y,max}$	$N_{y,min}$
997 kN	-4586 kN	105,6 kN	-432,9 kN

By comparing the previous figures the extreme values are located around the concave areas and in an area at the base. These areas will be dimensioning in the following reinforcement design. Large tension forces are unfavourable for the concrete - and a strongly reinforced ring beam in the circumferential direction is necessary around the *belt*.

12.1.2.6 Cross Section Determinition

By use of *The Cross Section Design Tool* introduced in section 7.6 the geometry has been divided into five zones. Figure 12.7 shows this subdivision.
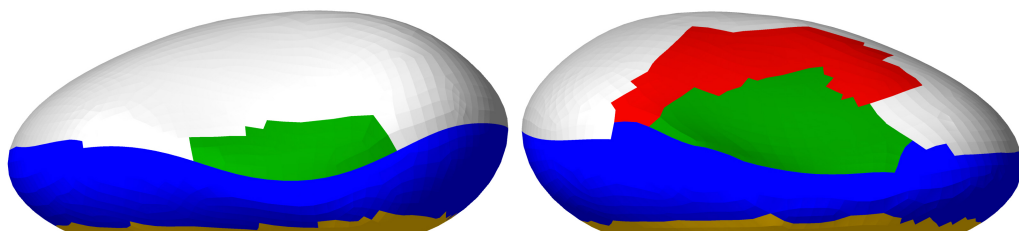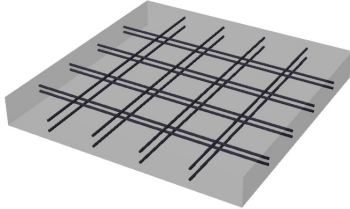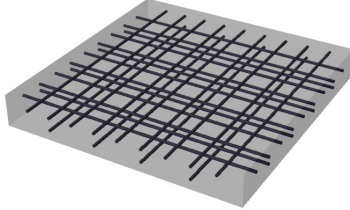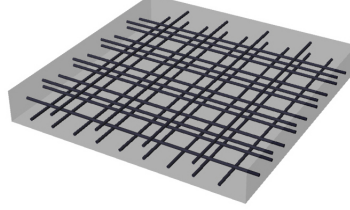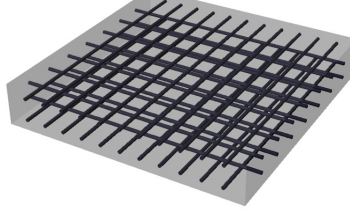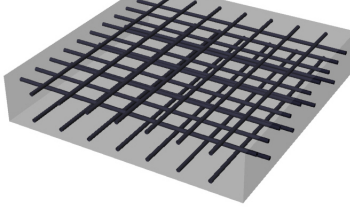
Figure 12.7: Original geometry divided into zones of determined cross sections.

Table 12.3 presents the cross section parameters for the five given areas shown in 12.7.

Table 12.3: Cross section parameters.

Concrete Layer	
Thickness	125 mm
Top Layer Reinforcement	
X-direction	4 x Ø10
Y-direction	4 x Ø10
Bottom Layer Reinforcement	
X-direction	4 x Ø10
Y-direction	4 x Ø10

Concrete Layer	
Thickness	135 mm
Top Layer Reinforcement	
X-direction	9 x Ø12
Y-direction	9 x Ø12
Bottom Layer Reinforcement	
X-direction	4 x Ø12
Y-direction	4 x Ø12

Concrete Layer	
Thickness	135 mm
Top Layer Reinforcement	
X-direction	4 x Ø12
Y-direction	4 x Ø12
Bottom Layer Reinforcement	
X-direction	9 x Ø12
Y-direction	9 x Ø12

Concrete Layer	
Thickness	175 mm
Top Layer Reinforcement	
X-direction	11 x Ø14
Y-direction	7 x Ø14
Bottom Layer Reinforcement	
X-direction	11 x Ø14
Y-direction	7 x Ø14

Concrete Layer	
Thickness	200 mm
Top Layer Reinforcement	
X-direction	7 x Ø16
Y-direction	10 x Ø16
Bottom Layer Reinforcement	
X-direction	7 x Ø16
Y-direction	4 x Ø16

From table 12.3 the cross sections for the red and green areas have been designed to obtain a negative and positive bending moment respectively. The blue area acts as the before mentioned tension ring around the *belt* of the structure. The yellow area has been designed especially in order to cope with the extremely stressed area at the base as mentioned earlier.

12.1.3 Linear/Non-Linear Deflection Ratio

Non-linear analyses are time consuming and a simple approach to estimate appropriate cross sections to satisfy the deflection limit of 30 mm is investigated in this section. By determining the ratio between the deflection found through a linear analysis and a non-linear analysis a generalisation can be made. Table 12.4 lists the linear and non-linear deflections found for the cross sections presented in the previous section exposed to characteristic dead load only.

Table 12.4: Deflection ratio.

Linear Deflection	Non-Linear deflection	r_u
31,6 mm	182,7 mm	5,78 height

Now that the ratio is determined the target deflection of the linear calculation can be determined as:

$$\frac{u_{limit}}{r_u} = \frac{30mm}{5,78} = 5,19mm \tag{12.1}$$

So to sum up: The cross sections are strengthened in the linear deflection calculations until the deflection found is below 5,19 mm. The strengthened structure is then used for the following non-linear calculation where the deflection found will be in the area of 30 mm though the cross section areas are simplified in an attempt to make the areas more realistic from a buildability point of view.

12.1.4 Non-Linear Analysis Results

The original geometry has been subdivided according to figure 12.6 - a modest change has been made around the *belt* where the ring beam has been straightened out. This is done from a modelling and buildability point of view. The subdivision can be seen in figure 12.8.

Figure 12.8: Subdivision of the original geometry.

The base and the ring beam have been modelled with a thickness of 1,5 meter, the concave areas have a thickness of 0,45 meter and the top area has a thickness of 0,4 meter. All areas have a reinforcement mesh respectively as the cross sections in table 12.3. However, a larger amount of reinforcement has been used. In the following figure the deflection of the structure can be seen. FE values of crack widths, stresses and strains for both concrete and reinforcement steel can be seen in appendix E.1.
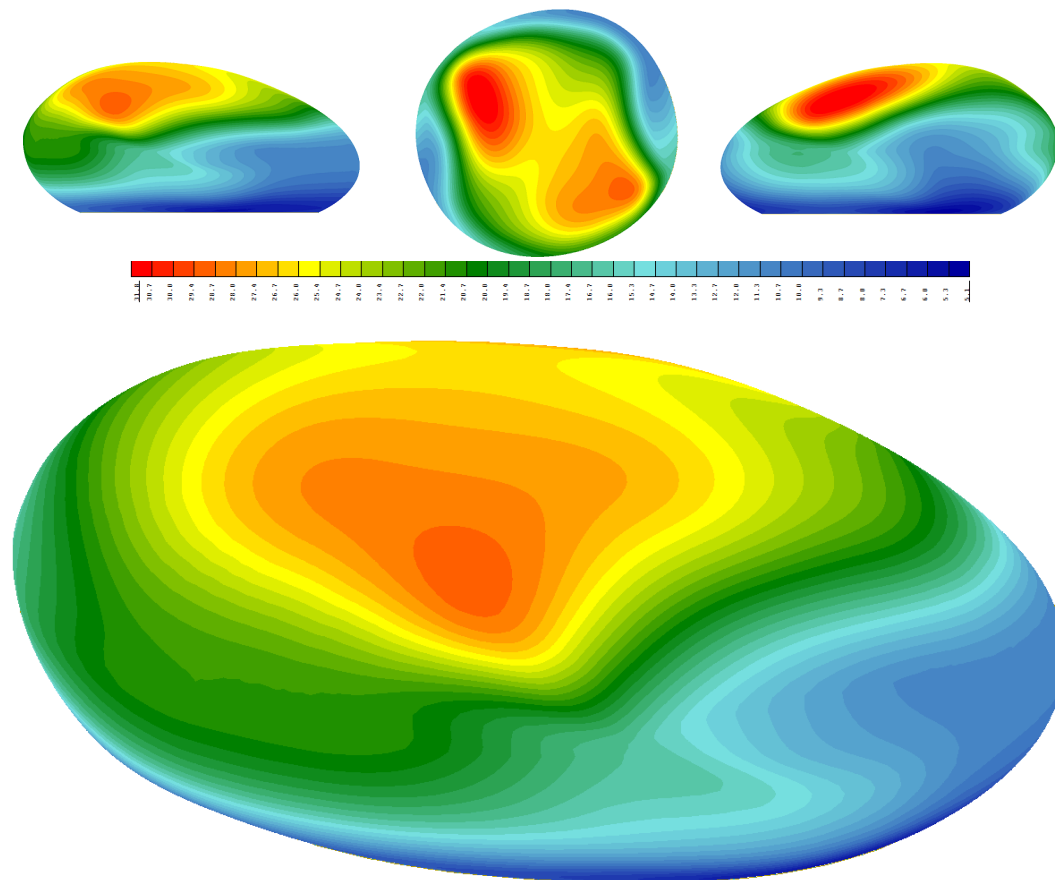
Figure 12.9: The non-linear deflection of the original geometry.

From figure 12.9 it is seen that the largest deflection occur at the boundary of the subdivision of the upper part. Whereas the thickness of the concave area is 0,45 m the convex area is only 0,4 m, therefore when the concrete cracks in this area the upper part has a smaller moment of inertia. Besides the cracking the concave areas are stronger reinforced than the upper part. In the following table the results from the non-linear analysis of the original geometry has been summarised.

Table 12.5: Non-linear analysis results for the original geometry.

Non-Linear Results	Value
Max Deflection	31,8 mm
Max Top Crack Width	0,405 mm
Max Bottom Crack Width	0,352 mm
Max Concrete Compressive Stress	6,78 MPa
Max Reinforcement Stress	276,6 MPa
Concrete Volume	2132,5 m^3
Reinforcement Volume	32,5 m^3

Information on the cross section for the different areas can be found in appendix E.1. As seen from table 12.5 the maximum deflection and maximum crack width is not fully satisfied. However, the deviation is at an acceptable level. Furthermore, it is seen that the coefficient of utilisation is quiet poor for the reinforcement. A maximum stress of 276.6 MPa indicates

that the reinforcement design to a large degree is determined by the maximum crack width. In the following section the optimised geometry has been analysed by the same procedure. In section 12.3 results for the two geometries will be compared.

12.2 Dimensioning the Optimised Geometry

Figure 12.10 shows the meshed optimised geometry undeformed and deformed when exposed to dead load. The meshed optimised geometry consists of 9232 elements.

(a) Undeformed mesh.   **(b)** Deformed mesh.
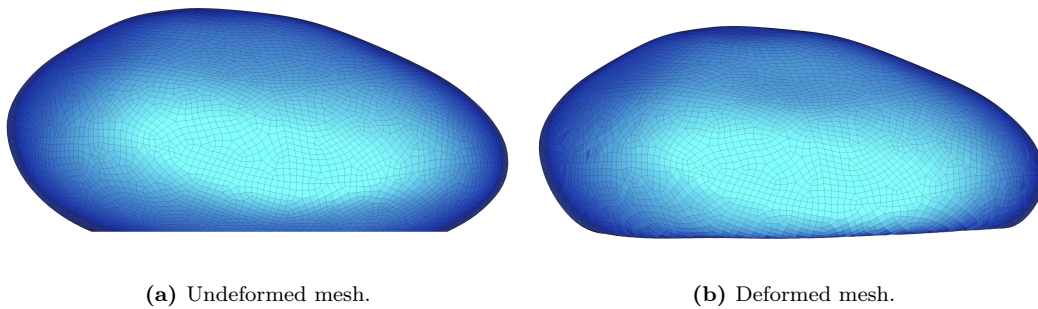
Figure 12.10: The optimised geometry meshed. Deformation scale factor: 100.

As seen in figure 12.10 the large deformation does not occur in the upper part of the structure after this part has been parametrically modelled as described in section 8.2. The overall deflection is now a result of the inclination of the lower part of the structure which has not been the subject of any geometric optimisation in this report.

12.2.1 Applied Loads

The shell structure is exposed to loads similar to the ones applied to the original geometry. Load parameters can be seen in table 12.6.

Table 12.6: Applied loads - optimised geometry.

Load	Intensity	Area
Snow Load	0,58 kN/m^2	742 m^2
Wind Load	1,5 kN/m^2	900 m^2
Self Weight	3,75 kN/m^2	3095 m^2

Again the self weight stated in the table above is based on an estimated uniform cross section height of 0,15 m and a density of the reinforced concrete of 25 kN/m^3.

12.2.2 Linear Analysis Results

The resulting section force distributions are presented before appropriate cross sections are applied in ULS as it was the case for the original geometry in section 12.1.2.

The section force distributions in the local directions are presented in figure 12.11 to 12.14. Values are averaged values within the respective "quads".
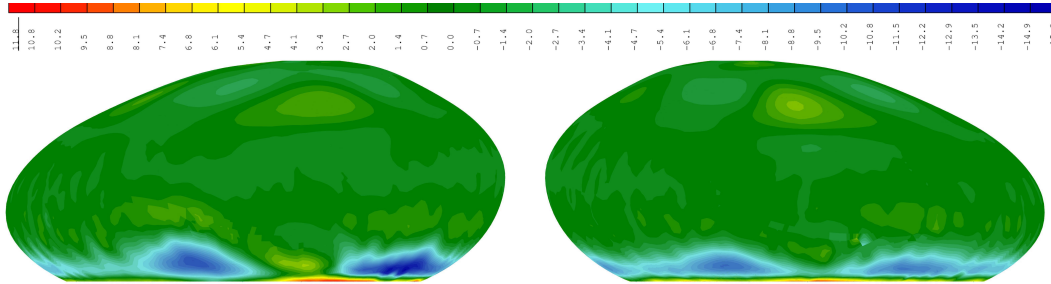
Figure 12.11: Distribution of bending moments. X-direction.
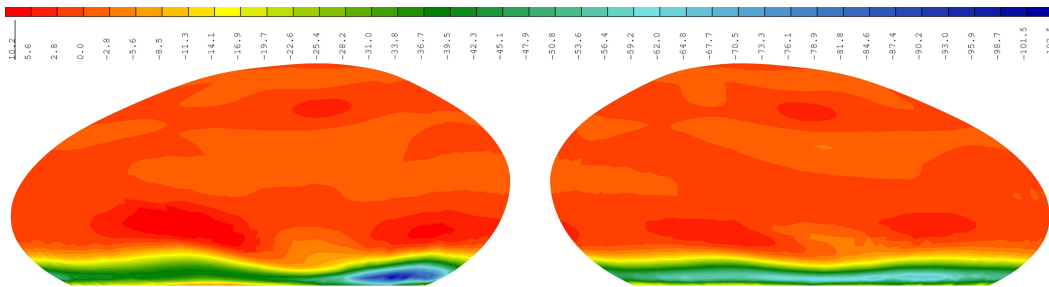
Figure 12.12: Distribution of bending moments. Y-direction.
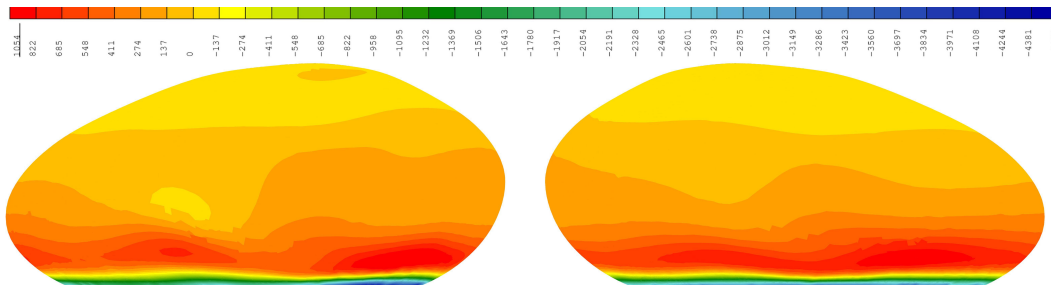
Figure 12.13: Distribution of membrane forces. X-direction.
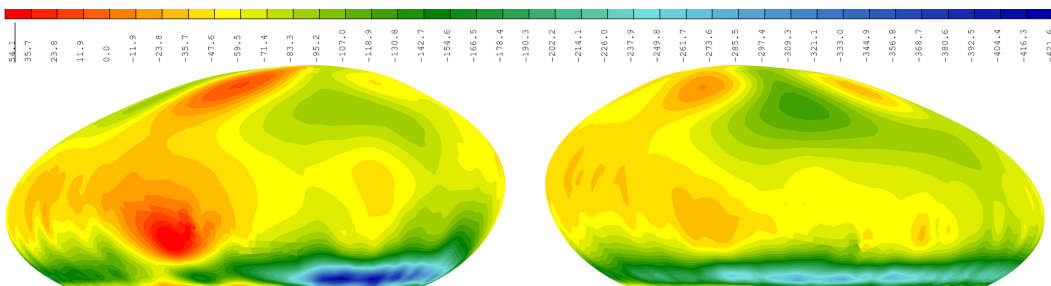
Figure 12.14: Distribution of membrane forces. Y-direction.

From figure 12.11 to 12.14 the initial conclusion would be that the distributions of the section forces in the local directions are more homogenous for the upper part of the optimised structure than for the original structure. However, the extreme values at the supports makes it hard to conclude how the section forces act in the upper part. Only the membrane force in

the y-direction experiences a degree of inhomogeneity in the upper part and as the upper part is the most interesting area since it was the subject of the geometry optimization process a more detailed evaluation of the section force distributions will be conducted in section 12.2.2.1. Besides a clearly more uniform upper part the base is exposed to section force distributions identical to the original geometry. Especially the previous mentioned weak area at the base occurs in all figures[2]. This area will be dimensioning in the reinforcement design for the whole lower part of the structure.

12.2.2.1   Section Forces Upper Part

As the previous investigation showed an extra study of the upper part of pebble B isolated from the lower part is needed in order to clearly see the section force distributions. The overall uniformity in the distributions at the upper part mentioned earlier is in contrast to the geometrical analysis of the optimised geometry in section 9.4. Here four planar areas (Fig. 9.7) were discovered which should be reflected in the section force distributions for the upper part. In the following four figures the section force distributions of the upper part is seen.

(a) Bending moment. X-direction

(b) Bending moment. Y-direction

(c) Membrane forces. X-direction

(d) Membrane forces. Y-direction

Figure 12.15: Cross section distributions for upper part

---

[2]The dark blue area in figure 12.11 and 12.12 indicate large negative moments. In figure 12.13 as a dark red area (tension force) and in figure 12.14 as a dark blue area (compression).

The four weak areas on the upper part are now clearly identified in figure 12.15. As predicted these areas will act with plate characteristics. The bending moment in both directions are positive and fairly larger compared to adjacent moments in all four ar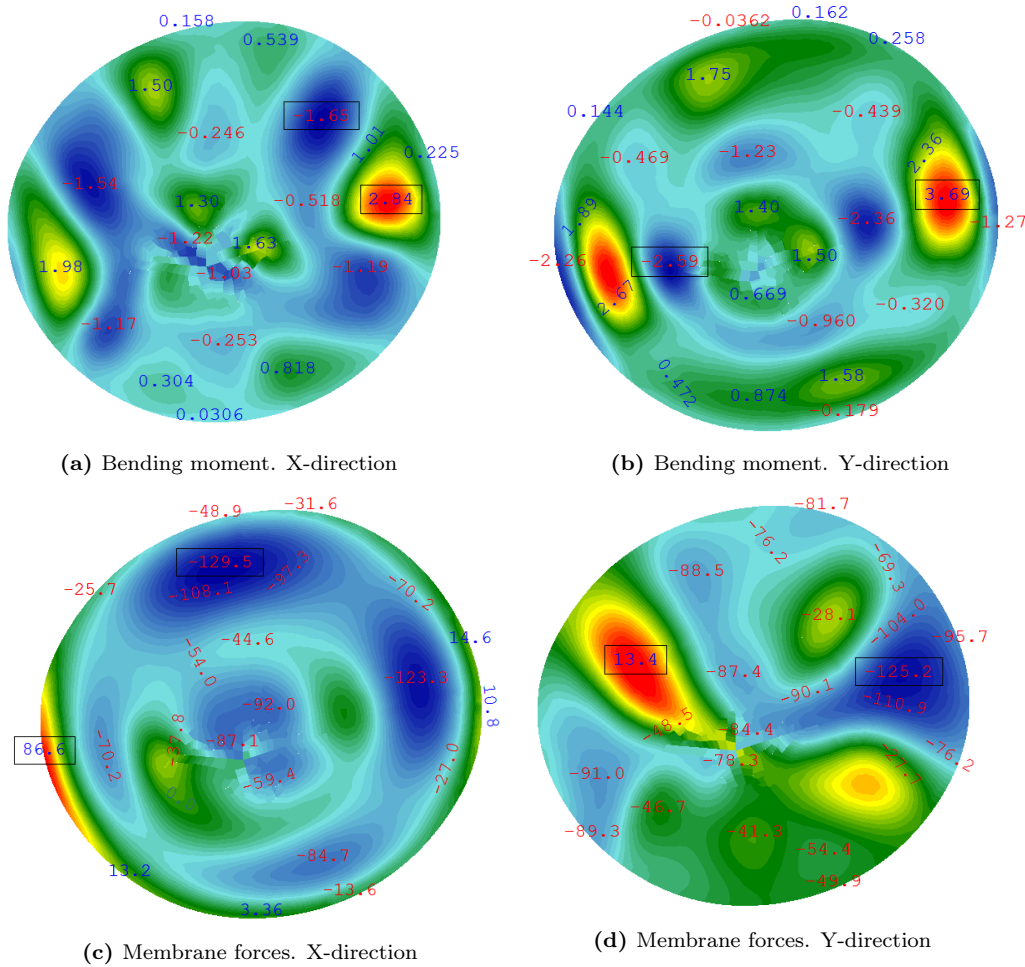eas. Furthermore, are the surrounding areas exposed to a negative moment just as in the case of planar/concave areas on the original geometry. For the membrane forces however, the tendency is the same around the planar areas as the forces are increased - this indicate an in-plane mode resistance. This is due to the fact that the areas are not completely flat.

12.2.2.2 Extreme Section Forces

Table 12.7 sums up the extreme values of the bending moments for the optimised geometry as seen from the section force distributions in figure 12.11 to 12.14.

Table 12.7: Extreme values of the bending moments - optimised geometry.

$M_{x,max}$	$M_{x,min}$	$M_{y,max}$	$M_{y,min}$
11,8 kNm	-15,3 kNm	10,2 kNm	-102,5 kNm

Furthermore the extreme values of the membrane forces are listed in table 12.8

Table 12.8: Extreme values of the membrane forces - optimised geometry.

$N_{x,max}$	$N_{x,min}$	$N_{y,max}$	$N_{y,min}$
1054 kN	-4423 kN	54,1 kN	-421,6 kN

The extreme values are not located in the upper part of pebble B as opposed to the original geometry. In terms of membrane moments in the upper part of the structure the optimisation has been successful but the extreme values have not been reduced significantly when considering the overall structure.

12.2.2.3 Cross Section Determinition

By use of The Cross Section Design Tool introduced in section 7.6 the following division into three different cross sections have been made. Figure 12.16 illustrates the subdivision of the optimised geometry into areas of the determined cross sections.
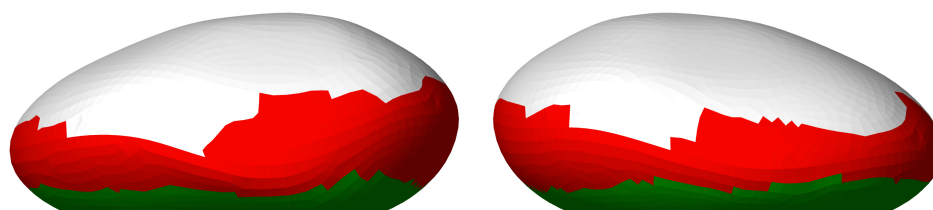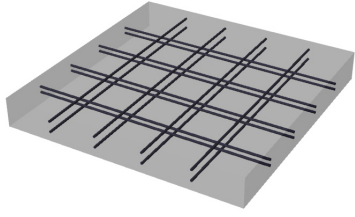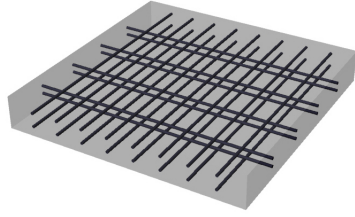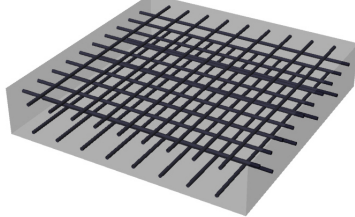

Figure 12.16: Optimised geometry divided into zones of determined cross sections.

Table 12.9 lists the cross section parameters.

Table 12.9: Cross section parameters.

Concrete Layer	
Thickness	125 mm
Top Layer Reinforcement	
X-direction	4 x Ø10
Y-direction	4 x Ø10
Bottom Layer Reinforcement	
X-direction	4 x Ø10
Y-direction	4 x Ø10

Concrete Layer	
Thickness	140 mm
Top Layer Reinforcement	
X-direction	8 x Ø12
Y-direction	4 x Ø12
Bottom Layer Reinforcement	
X-direction	8 x Ø12
Y-direction	4 x Ø12

Concrete Layer	
Thickness	200 mm
Top Layer Reinforcement	
X-direction	9 x Ø14
Y-direction	10 x Ø14
Bottom Layer Reinforcement	
X-direction	8 x Ø14
Y-direction	4 x Ø14

Compared to the subdivision of the original geometry the upper part now consists of one cross section. The red area acts as the tension ring with increased reinforcement in the x-direction. In the green area both the thickness and the amount of reinforcement is increased due to the weak area at the base.

12.2.3   Linear/Non-Linear Deflection Ratio

As it was the case for the dimensioning of the original geometry the ratio between the linear deflection and the non-linear deflection is determined to ease the following non-linear dimensioning process.
Table 12.10 lists the linear deflection, the non-linear deflection and the ratio between them. The deflections are found for the cross sections presented in section 12.2.2.3 exposed to characteristic dead load only.

Table 12.10: Linear deflection, non-linear deflection and deflection ratio.

Linear Deflection	Non-Linear deflection	r_u
14,5 mm	68,0 mm	4,69 height

Now that the ratio is determined the target deflection of the linear calculation can be de-

termined as:

$$\frac{u_{limit}}{ratio_u} = \frac{30mm}{4,69} = 6,40mm \tag{12.2}$$

The target deflection is therefore set to 6,40 mm for the linear deflection carried out before the non-linear dimensioning process is carried out.

12.2.4   Non-Linear Analysis Results

As for the original geometry the optimised geometry has been subdivided into different areas, enabling a ring beam at the 'belt'. However, as the structure contains no concave areas at the upper part there is no further need for subdividing the geometry. In figure 12.17 the subdivision can be seen.
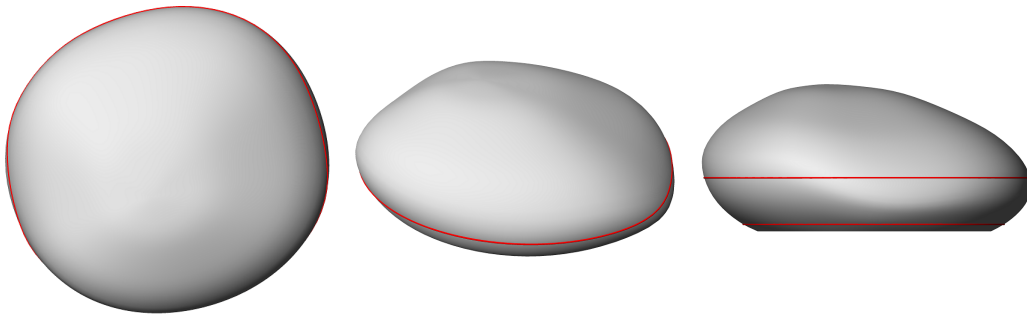
Figure 12.17: Subdivision of the original geometry.

The thickness of the cross sections are 1 meter for the base and the ring beam and 0,3 meter for the upper part. As for the original geometry the design requirements for the reinforcement are determined according to section 10.2. The deflection for the non-linear analysis can be seen in figure 12.18. Crack width, stresses and strains for both concrete and reinforcement steel can be seen in appendix E.2.
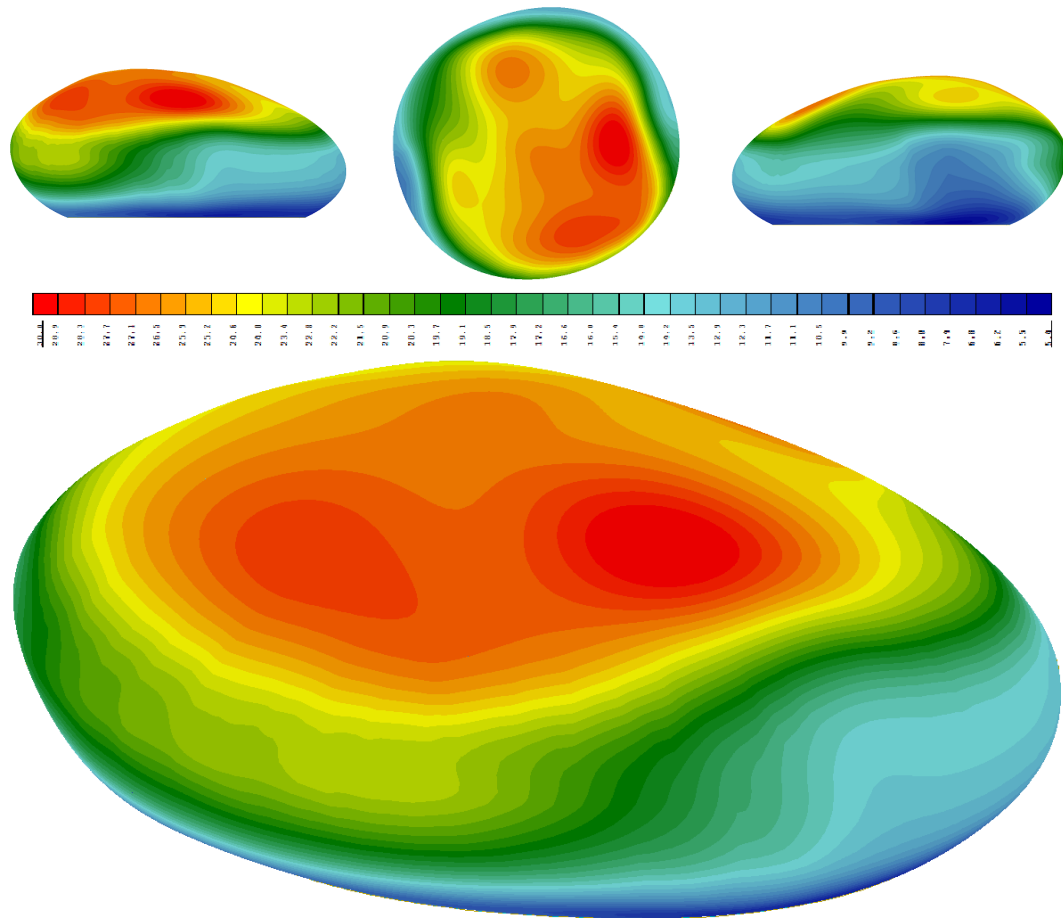
Figure 12.18: The non-linear deflection of the original geometry.

The largest deflection is located in the area with the largest positive bending moments in the upper part (figure 12.15). This is due to the cracked conditions in the lower part of the cross section forced by the bending moment. The deflection could be improved be increasing the thickness of the cross section but this improvement would also increase the bending moments an therefore, a gain would be minimal.

In the following table the results from the non-linear analysis of the optimised geometry have been summarised.

Table 12.11: Non-linear analysis results for the optimised geometry

Non-Linear Results	Value
Max Deflection	30 mm
Max Top Crack Width	0,422 mm
Max Bottom Crack Width	0,311 mm
Max Concrete Compressive Stress	8,19 MPa
Max Reinforcement Stress	324,2 MPa
Concrete Volume	1378,9 m^3
Reinforcement Volume	18 m^3

As for the original geometry the maximum crack width are not fulfilled. The utilisation of

materials are higher - indicating a more homogeneous structure. The material consumption is almost halved compared to the original geometry.

12.3   Results and Discussion of Structural Analysis

Two potential feasible designs of pebble B were investigated in the previous sections: The original geometry designed by Henning Larsen Architects and the optimised geometry designed by a the parametric model developed in this project. Both designs satisfy the overall design constraints regarding: Inclined base, highly curved, no inner columns and smooth interior surfaces. The results from the non-linear analysis can be seen in table 12.5 and 12.11 and it is clear that the optimised geometry satisfies the design criteria formulated in section 8.1: A reduction of the material consumption. Table 12.12 shows the concrete and reinforcement steel consumed for the optimised geometry compared to the original geometry.

Table 12.12: Comparison of material cunsumption. Non-Linear results.

	Concrete		Reinforcement steel	
	Original	Optimised	Original	Optimised
Volume	2132,5 m^3	1378,9 m^3	32,5 m^3m^3	18 m^3
Reduction	35,4 %		44,6 %	

A reduction in the concrete volume of more than 30% and the reinforcement steel volume of more than 40% are both significant amounts. These two observations indicate that the optimised structure is a more efficient shell structure only due to a reduction of the bending moments in the upper part which is indicated in figure 12.11 to 12.12. Generally the two geometries act as predicted in section 9.3 and 9.4 where areas with large curvature discontinuity or large principal radii are more exposed which verifies the potential gain of performing an geometric analysis before the final structural analysis.

In order to reduce the material consumption further different approaches can be used. An optimisation of the base and especially the weak area mentioned previously is one options and the most obvious in the perspective of this report. Additionally the concept of a bubble deck [3] can be applied for the upper part in order to reduce the weight and still maintain the moment of inertia. Furthermore, are plastic fibres mixed in the concrete a possible solution in order to reduce the crack width.

Besides the reduction in the material consumption the optimised geometry proved to be simpler to subdivide into different cross section areas. Having a more simple reinforcement mesh and as few cross section thicknesses as possible will ease the construction phase and possibly save time.

---

[3]By applying the bubble deck an reduction in the self weight around 40% is possible[22]

Part III

Part 3

CHAPTER 13

Structural Support to Pebble A

The upper pebble of The Batumi Aquarium, pebble A, is supported by the lower pebbles. This chapter investigates how the structural support to pebble A could be designed.

Section 13.1 aims to apply cross sections of sufficient stiffness to secondary frame structures to ensure a maximum deflection of 30 mm. Section 13.2 studies ring loads on shell structures and presents two different approaches to supporting pebble A through a ring load on pebble B[1].

According to Buro Happold a self weight of 7500 kN and an imposed load of 1500 kN from pebble A is to be supported by pebble B. Given a load combination of dominating imposed load the resulting load which will be the dimensioning load for this chapter becomes:

$$P_d = 7500kN + 1,5 \cdot 1500kN = 9750kN \tag{13.1}$$
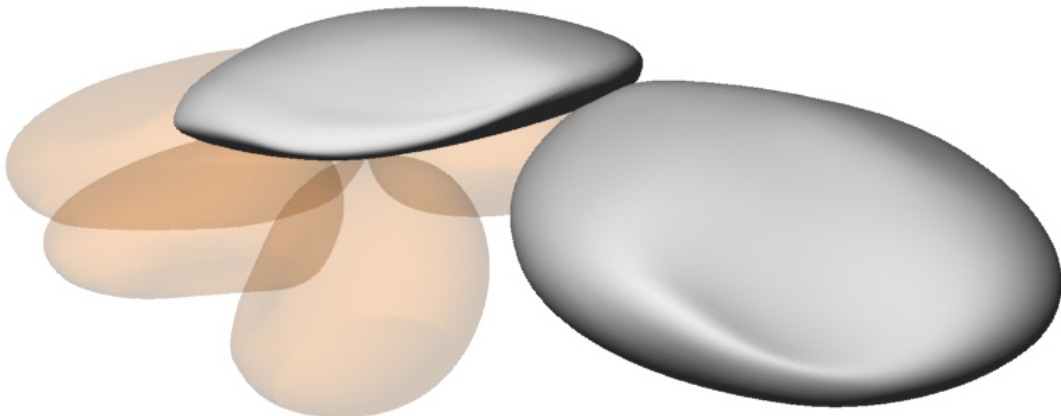
Figure 13.1 shows how pebble B supports pebble A.

Figure 13.1: Pebble B supporting pebble A.

---

[1]All investigations in part 3 are based on the original geometry of pebble B.

13.1   Secondary Structures

This section will briefly state examples of the necessary dimensions of welded beam sections and trusses in regards to obtaining the load from pebble A. The investigation is kept to a conceptual level and can only be justified in a magnitude based context.

Since the positioning of columns within the free space of pebble B was ruled out in the restrictions of the project in section 6.2 the only possible solution is to place the secondary structure in the perimeter of the shell geometry. For this purpose a parametric script have been developed in GH to place frame structures within the surface geometry of pebble B. The script offers the possibility to change the number of frames, apply any given standard steel profile and export the structure to Robot. The script can be seen in appendix F.2.

13.1.1   Structure Proposals

Numerous proposals to the geometry of the secondary structure could be developed and looked into. Two proposals can be seen from figure 13.2 with respectively 9 and 19 frames. Both might seem rather dense but as it can be seen from the calculations later on a very stiff structure is necessary to get an acceptable deflection.

(a) Structure A.   **(b)** Structure B.
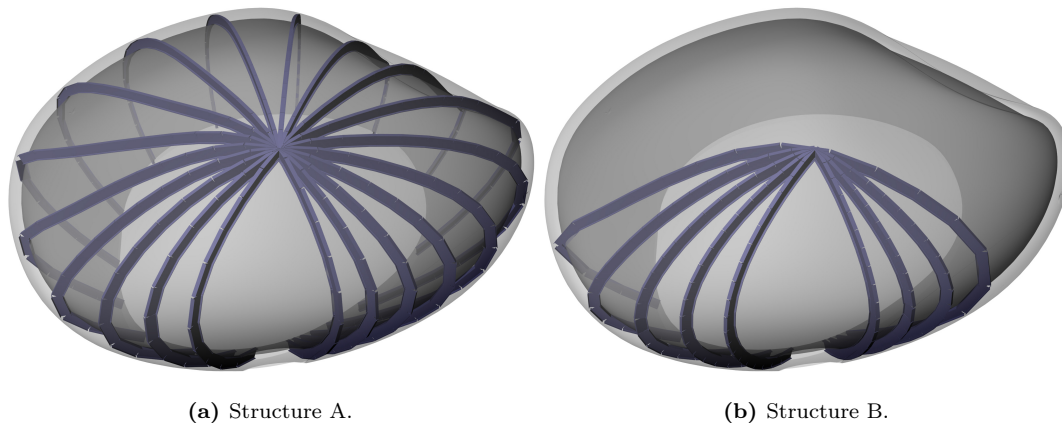
Figure 13.2: The two proposed secondary structures.

It can be predicted that structure A has a larger stiffness overall compared to structure B but the scale of structure A and hence the material applied might not be utilized as efficiently as for structure B.

As seen from figure 13.2 the spacing between frames changes in one end where three frames are left out. This is due to location of the entrance to the pebble B where the frames would interfere with the path of visitors in the aquarium.

13.1.2   Cross Section Proposals

Different cross sections are investigated to see how a reasonable deflection of the secondary structure canbe secured. In an attempt to make the scale of the calculated deflections more relatable the structure is investigated by the use of standard cross sections. It is clear that

the moments of inertia simply are not large enough to satisfy a deflection restriction of 30mm. Figure 13.3 shows the two structures exported to Robot with IPE600 profiles applied to the frames.

(a) Structure A - Robot.

(b) Structure B - Robot.
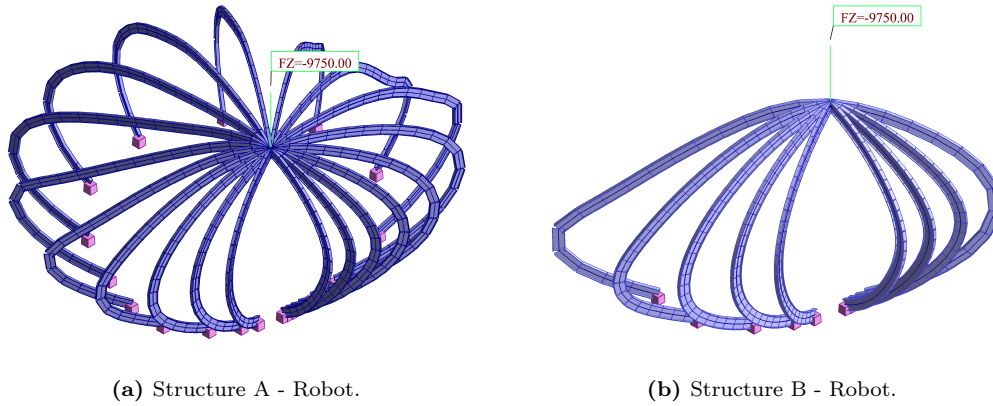
Figure 13.3: The two proposed secondary structures.

Table 13.1 and 13.2 confirm that the investigated cross sections do not satisfy the target deflection.

Table 13.1: Deflections - Structure A.

Profile	Moment of Inertia	Deflection	Steel Volume
IPE600	$920,8 \cdot 10^6 mm^4$	746mm	9,6 m^2
HEM1000	$7223 \cdot 10^6 mm^4$	103mm	27,2 m^2

Table 13.2: Deflections - Structure B.

Profile	Moment of Inertia	Deflection	Steel Volume
IPE600	$920,8 \cdot 10^6 mm^4$	1426mm	3,5 m^2
HEM1000	$7223 \cdot 10^6 mm^4$	187mm	9,9 m^2

Therefore the necessary moment of inertia for a given cross section is calculated to see what dimensions such a cross section could have:

$$I_{y,structureA} \quad = \frac{u_{reference}}{u_{target}} \cdot I_{reference} \tag{13.2}$$

$$I_{y,structureA} \quad = \frac{103mm}{30mm} \cdot 7223 \cdot 10^6 mm^4 = 24799 \cdot 10^6 mm^4 \tag{13.3}$$

$$I_{y,structureB} \quad = \frac{187mm}{30mm} \cdot 7223 \cdot 10^6 mm^4 = 45024 \cdot 10^6 mm^4 \tag{13.4}$$

The target moment of inertias correspond to cross sections - when kept in height/width scale of a HEM profile - seen from figure 13.4.

(a) Structure A.   **(b)** Structure B .
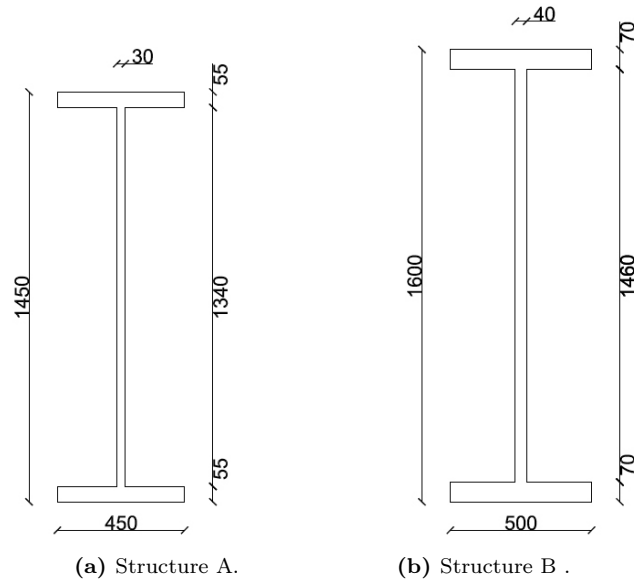
Figure 13.4: Proposals for cross sections with necessary moments of inertia. Measures in mm.

Table 13.3 shows the moments of inertia of the proposed cross sections from figure 13.4 along with the total steel volume for the frame structures.

Table 13.3: Resulting moments of inertia and total steel volumes.

Structure	Moment of Inertia	Deflection	Steel Volume
A	$3{,}0 \cdot 10^{10} mm^4$	30 mm	54,9 m^3
B	$5{,}0 \cdot 10^{10} mm^4$	30 mm	28,6 m^3

It is concluded that a welded I-profile frame structure is not an applicable solution in this case. The large vertical load combined with the inclination of the lower part of the frames makes the necessary stiffness of the cross section extremely large. Columns - steel or concrete - will always be preferable when a load of this size is to be transferred to the foundation. In this project however it was specifically stated in the restrictions that columns should not interfere with the interior space of pebble B. The suggested solution is then to transfer the loads through membrane forces in the shell structure which will be investigated in section 13.2.

13.2 Ring Load Support

Section 13.1 concluded that a secondary structure not consisting of vertical columns was not a suitable approach. This section seeks to clarify how the shell reacts if exposed to the given self weight from pebble A.

Since point loads on a shell structure are unfavourable, as observed in part I in this report, this section will investigate different approaches to transferring the load from pebble A to pebble B as a ring load. Another solution could be a line load through a hidden beam in the reinforced concrete cross section of the shell but the ring load approach is preferred here since the natural intersection geometry between two pebbles or spheres will have a circular geometry. The circular intersection between pebble A and pebble B is illustrated in figure 13.5.
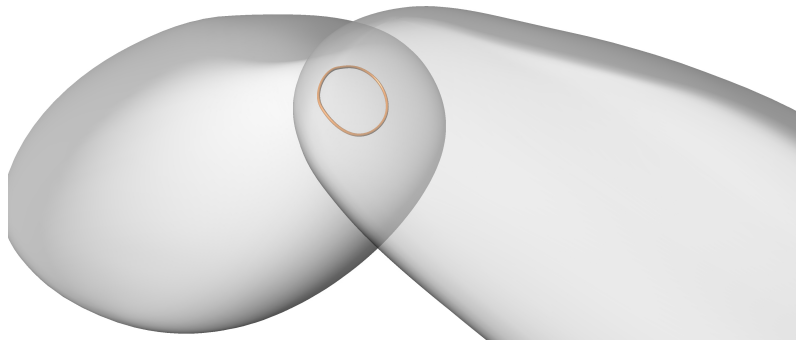

Figure 13.5: Circular intersection between pebble A and pebble B.

Before applying the ring load to the pebble B geometry a ring load study is carried out as a prerequisite to the optimisation of the structure later in this chapter.

13.2.1 Ring Load Study

This investigation of ring loads is based on a qualitative approach where various load and geometry setups will be investigated and evaluated. The qualitative approach is preferred as opposed to an analytical approach because of the parametric modelling process upon which this report is based. The parametric approach enhances the generation and alteration of models which is of great value for a qualitative investigation.

Eight load and geometry setups are investigated in continuation of the various investigations carried out in part I. All geometries are applied with similar cross sections and the boundary conditions presented in section 10. The structural analysis of pebble B applied the weakest cross section to the upper part of the structure. To reduce the maximum deflection in the upper part of the shell the target of this study is to reduce the bending moments especially locally around the ring load. The eight analysis setups illustrated in figure 13.6 is the combination of two geometries exposed to four different loads. The first geometry - setup 1, 3, 5 and 7 - is a truncated hemisphere with a radius of 7,5 m which is chosen in continuation of the investigations done for the hemisphere in chapter 4. The second geometry - setup 2, 4, 6 and 8 - is an axisymmetrical truncated shell structure with a circular plan (radius = 7,5 m) and a height of 9 m. The two different geometries are investigated in an attempt to clarify the importance of the angle between the applied load and shell but also to investigate how the section forces are influenced when the load is applied through a ring beam as opposed to a circular line load.
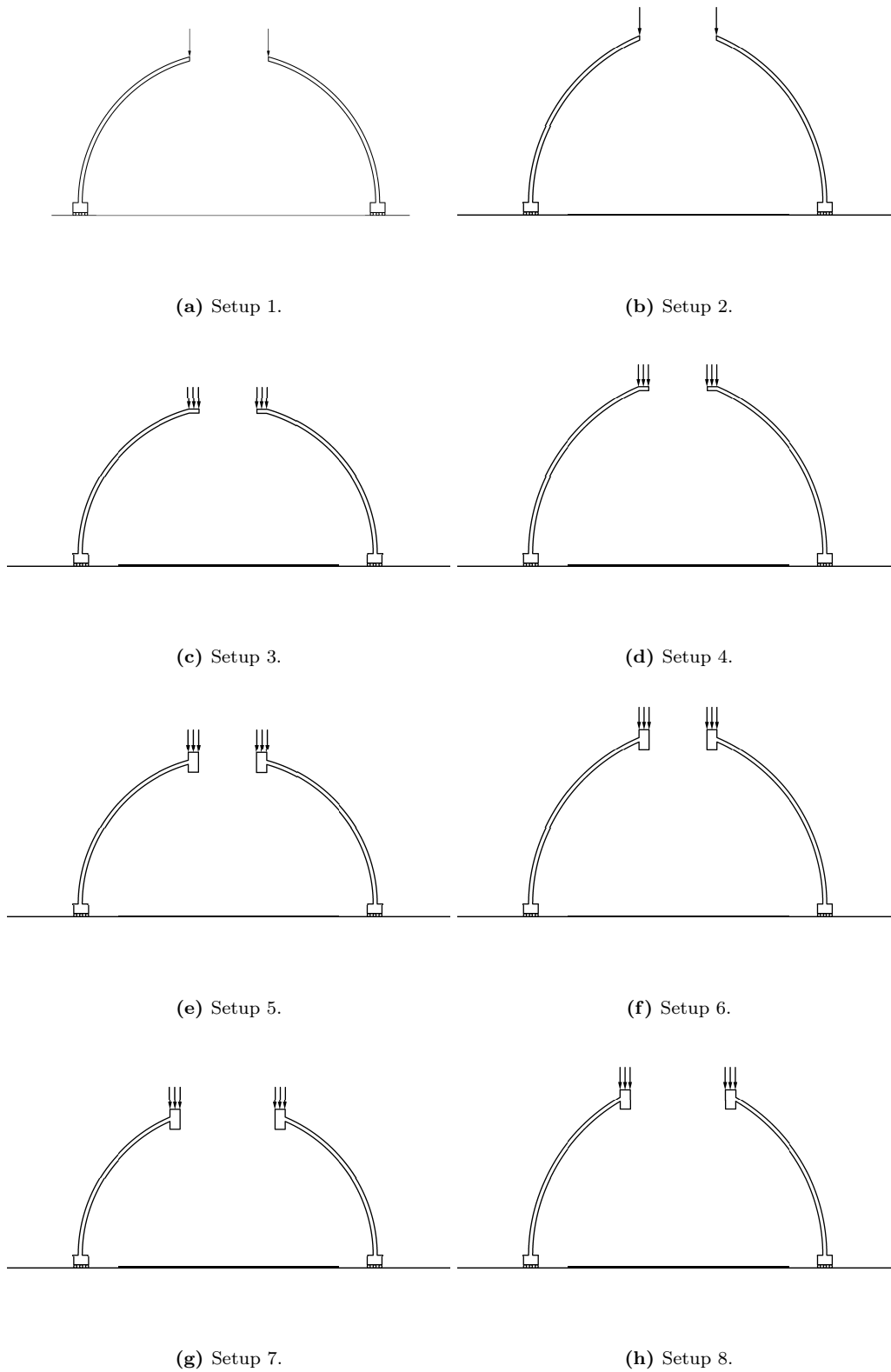
(a) Setup 1.

(b) Setup 2.

(c) Setup 3.

(d) Setup 4.

(e) Setup 5.

(f) Setup 6.

(g) Setup 7.

(h) Setup 8.

Figure 13.6: The analysis setups.

The two geometries are exposed to four different loads all with a magnitude of 6283 kN corresponding to a ring load of 500kN/m with a radius of 2 m. The parameters of the geometries and load setups are listed below. Alterations are highlighted in bold text.

- Line load. [Setup 1 and 2].
- A circular surface load. Radius: 2 m. Ring beam width: 1m. **Cross section height: 0,2 m**. [Setup 3 and 4].
- A circular surface load. Radius: 2 m. Ring beam width: 1m. **Cross section height: 2 m**. [Setup 5 and 6].
- A circular surface load. **Radius: 3 m**. Ring beam width: 1m. Cross section height: 2 m. [Setup 7 and 8].

The reason why the cross section of the ring beam in setup 5 to 8 is made stiffer by increasing the height is that a reduced bending of the ring itself will result in a smaller bending moment transferred to the shell structure from the ring. However, the bending moments are only reduced to a certain degree hence an infinitely stiff ring beam will still transfer bending moments to the shell.

13.2.1.1 Section Force Distributions

The extreme values of the section forces for all eight setups can be seen from table 13.4. The local coordinate systems are similar to the ones presented in section 10.1.1.

Table 13.4: Extreme section forces.

Setup	$M_x[kNm/m]$ Max	Min	$M_y[kNm/m]$ Max	Min	$N_x[kN/m]$ Max	Min	$N_y[kN/m]$ Max	Min
1	75	-5	3	-111	802	-5681	-133	-965
2	48	-4	2	-91	571	-4946	-133	-821
3	48	-5	3	-118	882	-2807	-133	-1205
4	25	-4	2	-107	653	-2233	-133	-1011
5	23	-1	72	-22	492	-780	-133	-994
6	14	-1	42	-14	331	-599	-133	-858
7	11	-1	29	-15	352	-557	-133	-557
8	8	-1	18	-11	258	-491	-133	-507

The extreme values of the bending moments have been plotted in figure 13.7. The diagram illustrates the span between maximum and minimum values of the bending moments. To verify the eight analyses carried out it is seen that the maximum section force in the local y-direction - the vertical reaction at the supporting boundary - approximately corresponds to the total vertical load of 6283 kN.[2]

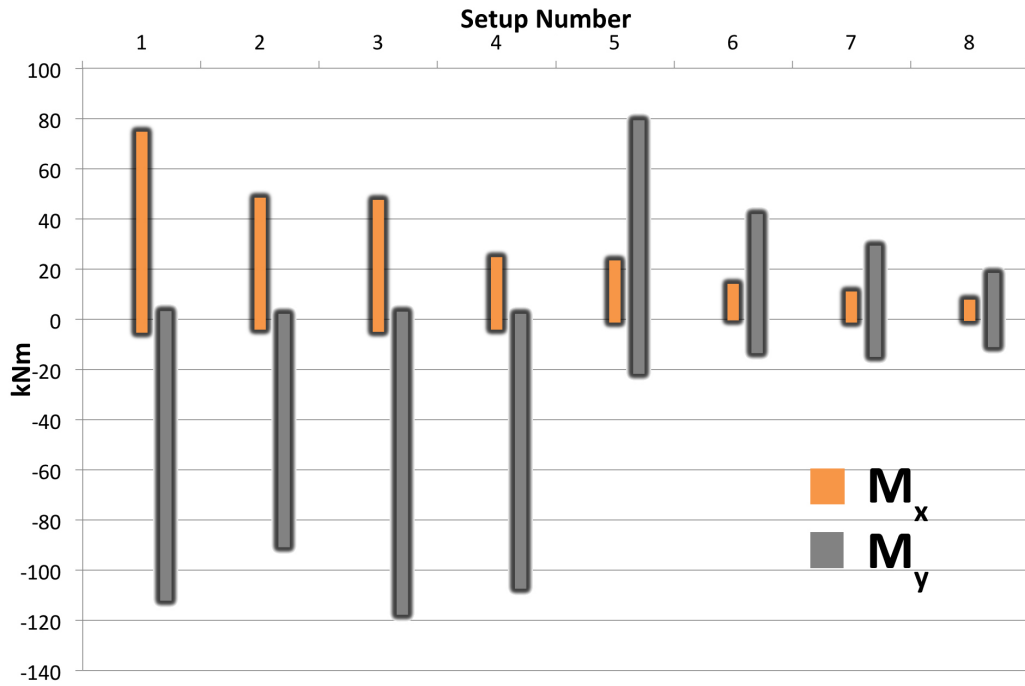[2]133kN/m $\cdot 15m \cdot \pi = 6267,5kN$.

Figure 13.7: Comparison of M_x and M_y values for the eight different geometries.

It can be concluded that the bending moments in the local x-direction is significantly reduced when the angle between the load direction and the shell structure is reduced. The stiffness of the ring beam also seems to have the desired effect. The bending moment in the local y-direction however acts differently for the geometries where the ring beam is introduced (setup 5 to 8). To clarify how the bending moment distribution changes when the ring beam is implemented the M_y distribution for setup 1 and setup 5 is presented in figure 13.8.
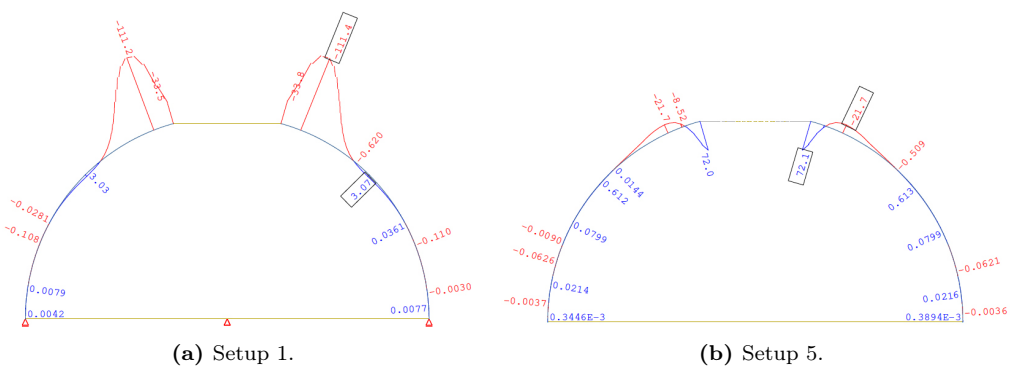
(a) Setup 1.

(b) Setup 5.

Figure 13.8: Comparison of M_y.

Figure 13.8 shows that relatively large negative bending moments are found in the area around the circular line load for setup 1 as opposed to the positive moment found at the edge of the ring beam in setup 5. It seems that for the line load in setup 1 the behaviour of the shell structure is comparable to a cantilevered beam while the stiffness of the ring beam introduced in setup 5 changes the operational sign of the bending moments at the edge of

the shell structure.

Figure 13.9 shows the span of the membrane forces in local directions for the eight setups.
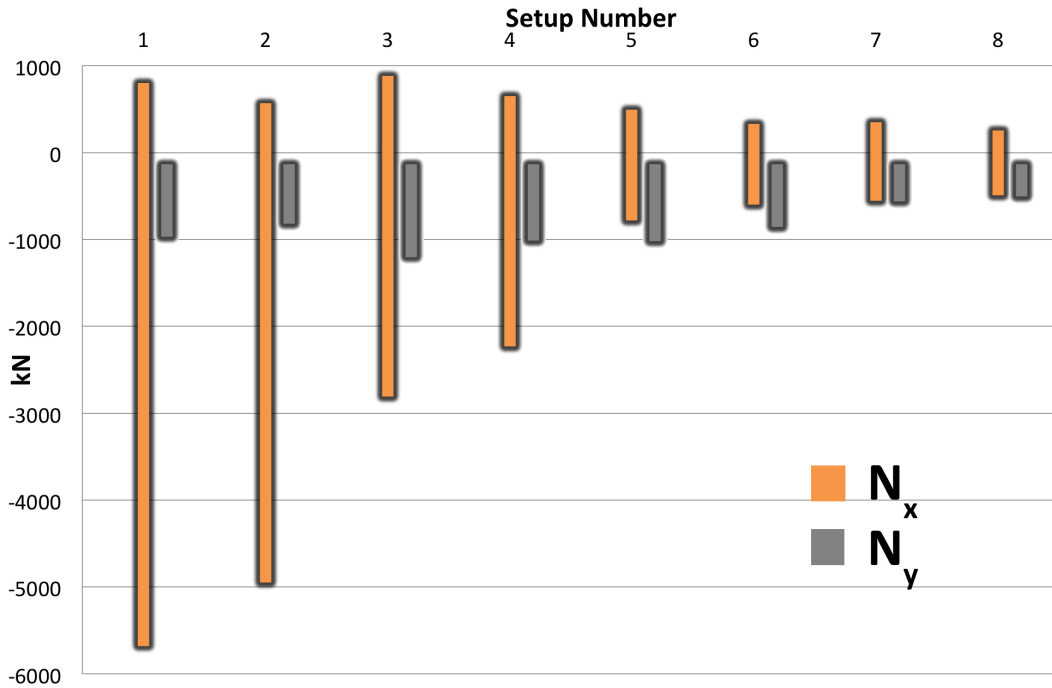
Figure 13.9: Comparison of N_x and N_y values for the eight different geometries.

It is seen that the membrane force in the local y-direction is reduced especially when the radius of the ring beam is increased (setup 7 and 8) but the remaining alterations does not seem to have much influence. Figure 13.10 show the nature of the membrane forces in the local y-direction for load setup 1 and 5.

(a) Setup 1.

(b) Setup 5.

Figure 13.10: Comparison of M_y.

It is seen that the membrane force distributions in the local y-direction for setup 1 and 5 are almost identical at that the vertical reaction at the base corresponds to before verified vertical reaction force.

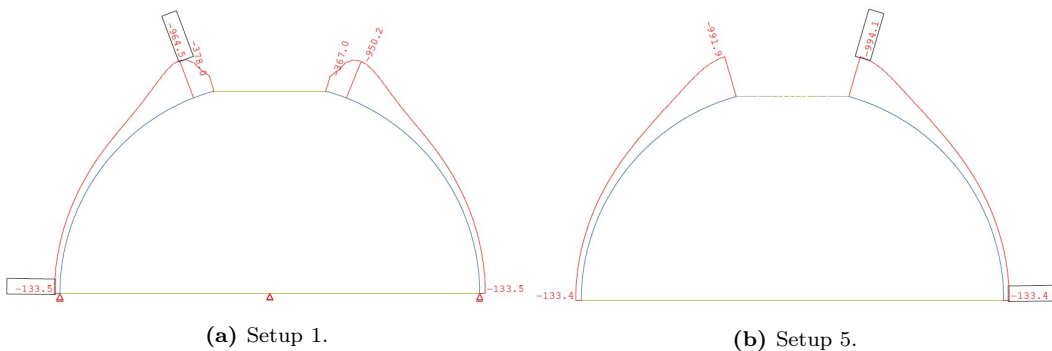The membrane force in the local x-direction, the circumferential direction, is heavily reduced through all alterations especially when the ring beam is introduced. This is probably due to the circumferential stiffness of the ring beam that acts as a compression ring.

It is interesting to see that the widening of the ring beam introduced in setup 7 and 8 has an insignificant effect on the extreme values of N_x.

13.2.2   Ring Load on Pebble B

From the ring load study above it was concluded that a ring beam with sufficient stiffness improves the distribution of section forces over the shell structure. This approach can be implemented on pebble B without interfering with the original geometry. A ring beam with a thickness of 1 m and a height of 2 m could be hidden within the large shells of pebble A and pebble B. This approach will be investigated in section 13.2.2.1.

The second approach investigated is a combination of a stiff ring beam and a conical geometry pointed towards the centre of the ring load which decreases the angle between the load direction and the shell geometry. The radius of the ring beam for the conical geometry has been increased by 1 m. This investigation is carried out in subsection 13.2.2.2. The two approaches are illustrated in figure 13.11.

(a) Ring beam approach.   (b) Conical geometry with ring beam approach.
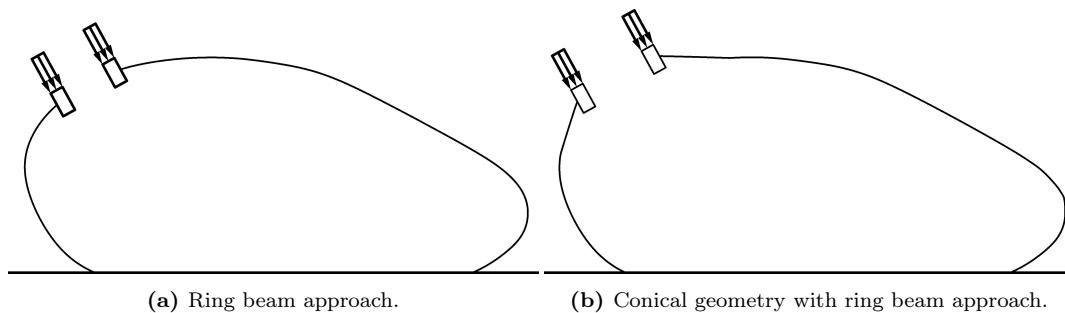
Figure 13.11: The two ring load approaches.

The ring beam is tilted approximately 30° from horisontal which increases the transverse total loading on the ring beam to:

$$p_d = 9750kN/cos(30) = 11250kN \tag{13.5}$$

13.2.2.1 Ring Beam Approach

The first approach applies the load to pebble B through a ring beam as seen in figure 13.12. The ring beam has a width of 1 m and a height of 2 m. The analysis is carried out in Sofistik with boundary conditions according to section 10.1.1.
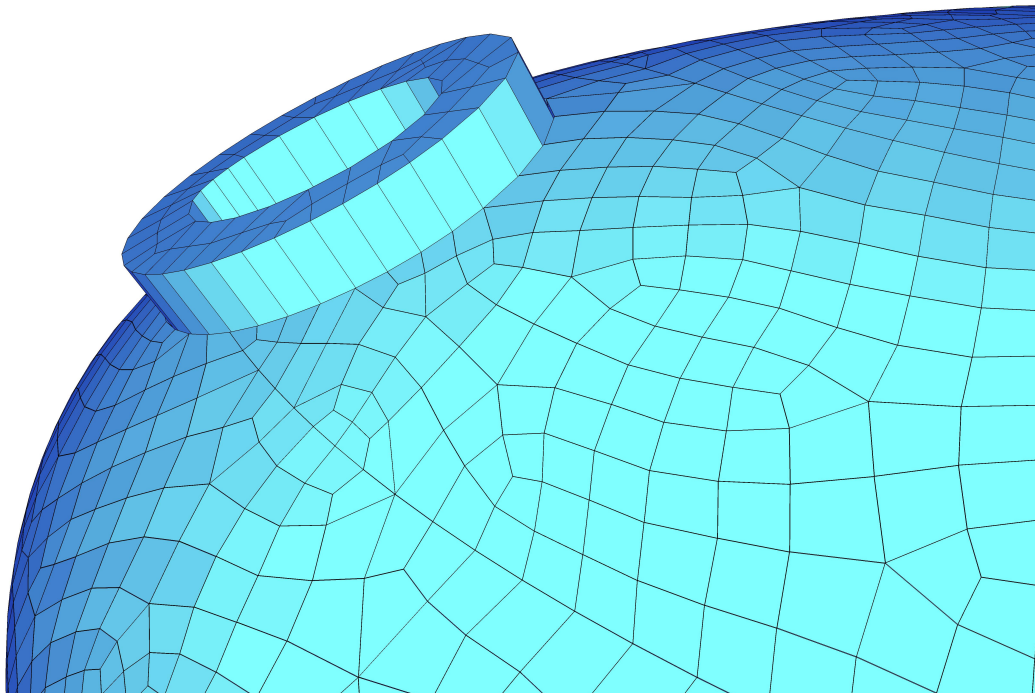

Figure 13.12: Sofistik FEA model of the ring beam approach.

The extremes of the principal section forces for the structure can be found in table 13.5. The section forces in the ring beam are not included in the table[3].

Table 13.5: Extremes of principal section forces.

$M_I[kNm/m]$		$M_{II}[kNm/m]$		$N_I[kN/m]$		$N_{II}[kN/m]$	
Max	Min	Max	Min	Max	Min	Max	Min
191	-31	46	-201	1857	-923	26	-7415

Figure 13.13 and 13.14 presents the principal moment distributions for the ring beam approach.

---

[3]Due to local coordinate inconsistencies between the two investigated models, principal section forces are used as the matter of comparison. Principal section forces does not act in local coordinate systems.
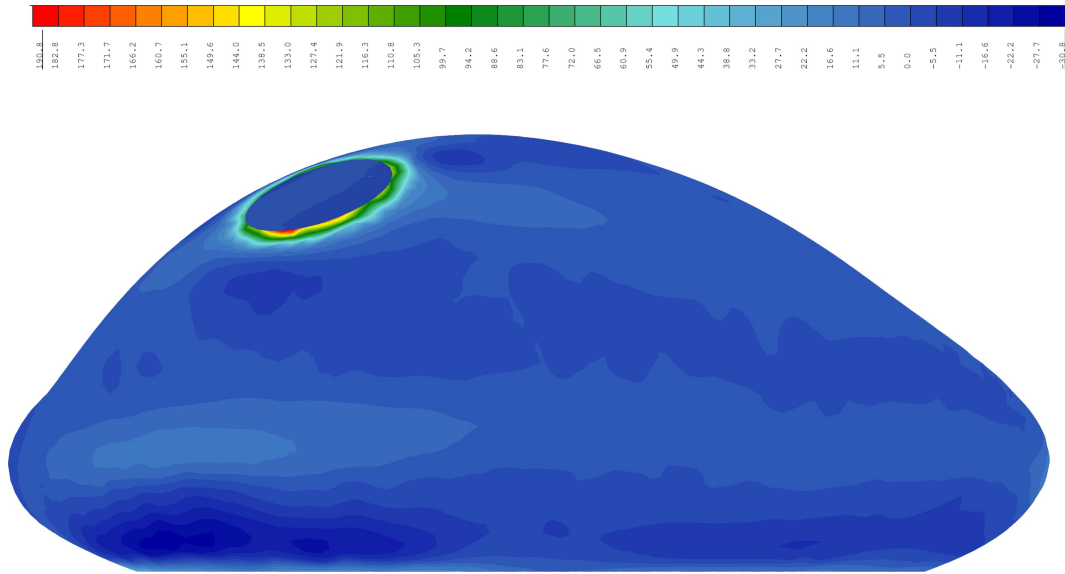
Figure 13.13: M_I distribution from Sofistik.
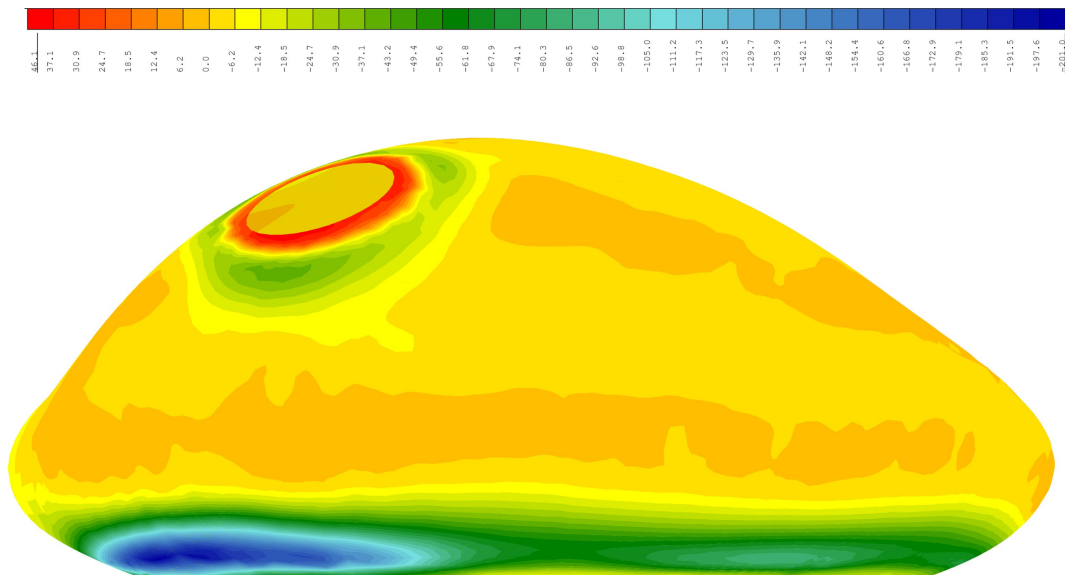
Figure 13.14: M_{II} distribution from Sofistik.

It is seen from the principal moment distributions that the largest negative moment is found directly underneath the ring beam while the largest positive moment is found at the edge of the ring beam.

It seems that the large negative bending moments are located at a relatively large distance[4] from the ring beam and it can be predicted that a local optimisation of the structure around the ring beam might not influence the size of the negative moment greatly.

The membrane forces are evaluated in terms of the principal stresses in the centre plane of the cross section as these are directly related to the principal membrane forces. The Principal Stress Trajectory Tool, section 7 is applied to the section force data from Sofistik

---

[4]Saint Venant's principal

and the principal stress trajectories are presented to assist the understanding of the principal membrane forces in the structure. The sizes of the stresses are not strictly relevant in this investigation since they are based on a uniform cross section with a thickness of 200 mm but the trajectories clearly show how the principal stresses are distributed over the geometry.

(a) σ_I distribution from Sofistik.

(b) σ_I stress trajectories.

(c) σ_{II} distribution from Sofistik.

(d) σ_{II} stress trajectories.
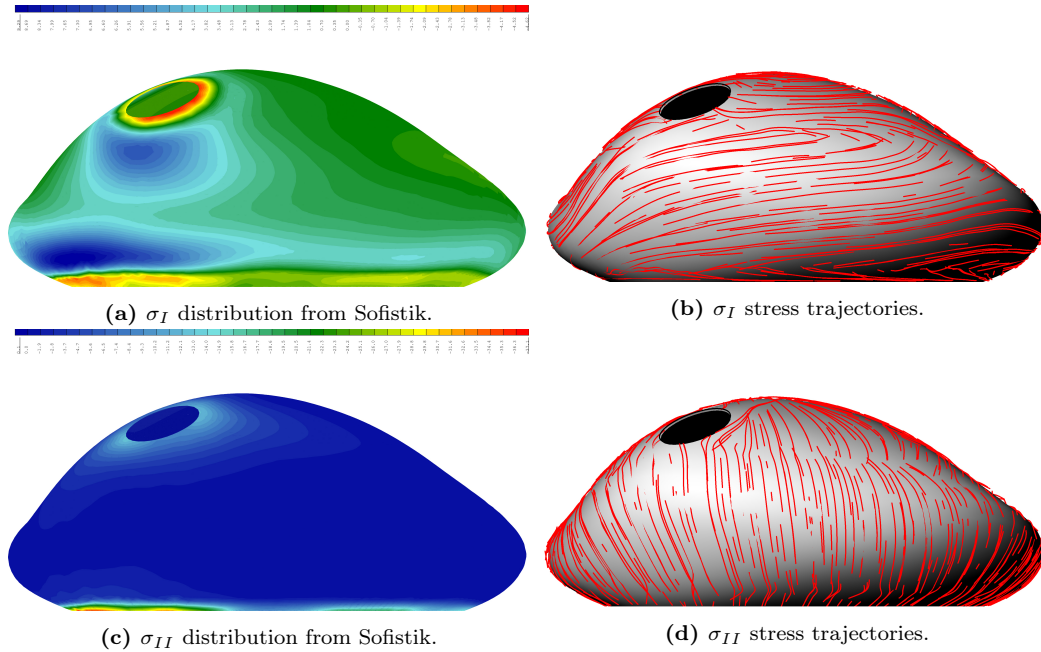
Figure 13.15: Principal stresses compared to the corrosponding stress trajectories.

It can be seen that the largest tension stresses act horizontally on the approximately vertical sides around the shell structure while the largest compression stresses, negative σ_{II}, are found directly under the ring load. The vertical supporting forces act from the supporting base line towards the ring beam.

The optimised pointed geometry towards the load direction, referred to as the conical geometry, is now investigated under similar circumstances to facilitate a comparison of the two investigated approaches.

13.2.2.2   Optimised Geometry with Ring Beam Approach

Again a ring beam approach is implemented but now with an optimised conical geometry in an attempt to reduce the bending moments in the area around the ring beam.
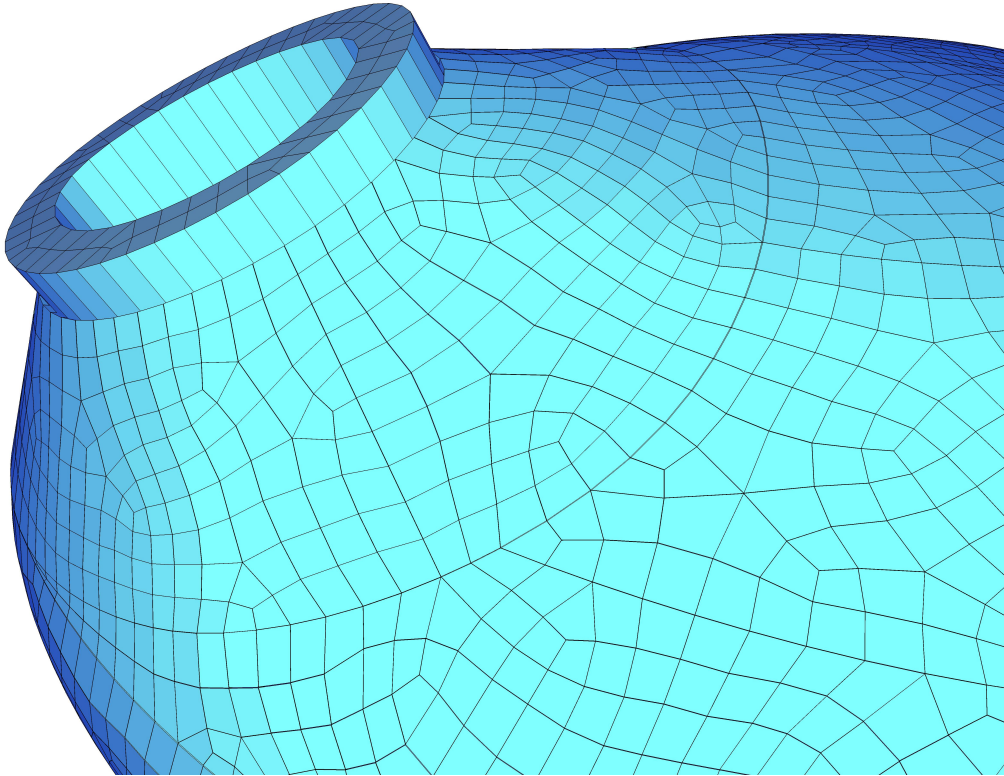

Figure 13.16: Sofistik model of the optimised conical geometry with ring beam approach.

The extremes of the principal section forces for the structure can be found in table 13.6.

Table 13.6: Extremes of principal section forces.

$M_I[kNm/m]$		$M_{II}[kNm/m]$		$N_I[kN/m]$		$N_{II}[kN/m]$	
Max	Min	Max	Min	Max	Min	Max	Min
38	-31	15	-205	1868	-729	65	-7591

It is seen that the maximum values of the principal bending moments have been reduced through the optimisation of the geometry but that the minimum principal bending moments have not been reduced. To understand the behaviour of the principal bending moments the distributions are shown in figure 13.17 and 13.18.
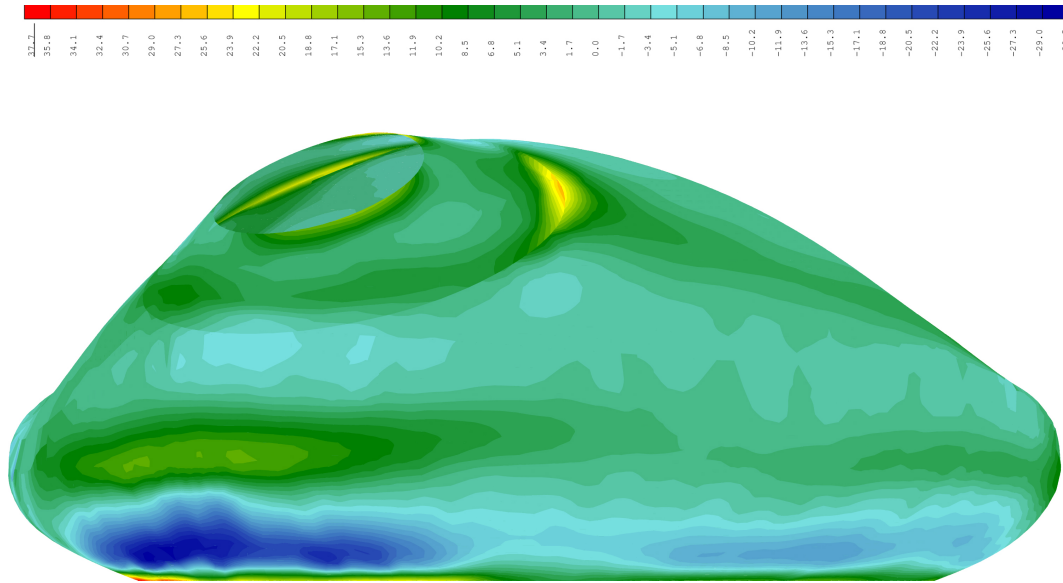
Figure 13.17: M_I distribution from Sofistik.
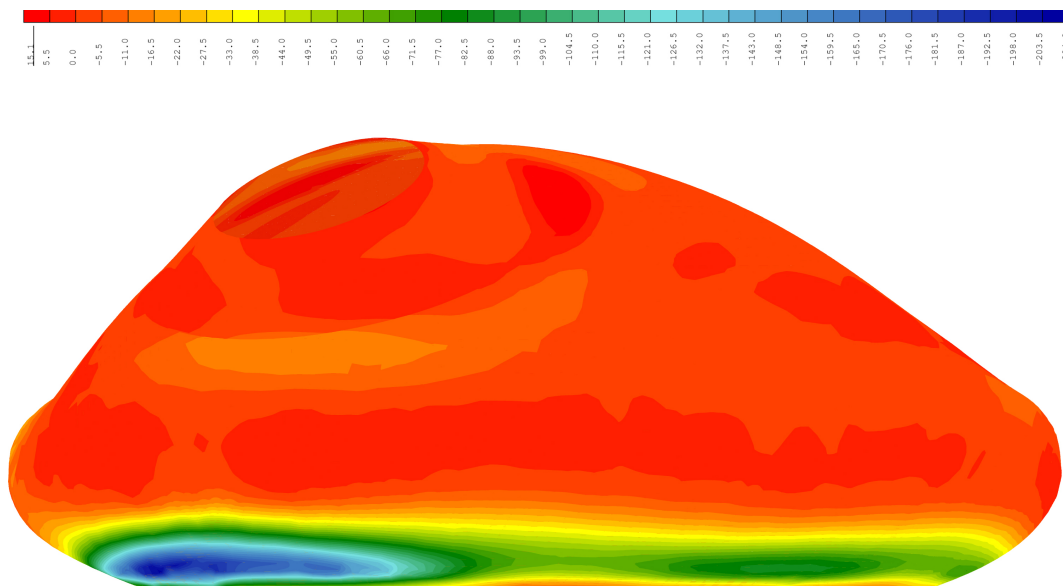
Figure 13.18: M_{II} distribution from Sofistik.

From figure 13.17 and 13.18 it is seen that the bending moments around the ring beam is reduced. The shell structure experiences a large bending moment at the support but as for the ring beam approach the bending moment can not be reduced by optimising the area around the ring beam. By comparing the bending moments to the ones observed in section 12.1.2 it is seen that the same weak area by the support results in large bending moments.

The principal stress distributions compared to the principal stress trajectories for the centre plane of the cross section can be seen from figure 13.19 to obtain a basic understanding of the behaviour of the membrane forces. Again the exact sizes of the principal stresses are not strictly relevant in an isolated perspective, but are useful in the comparison between the
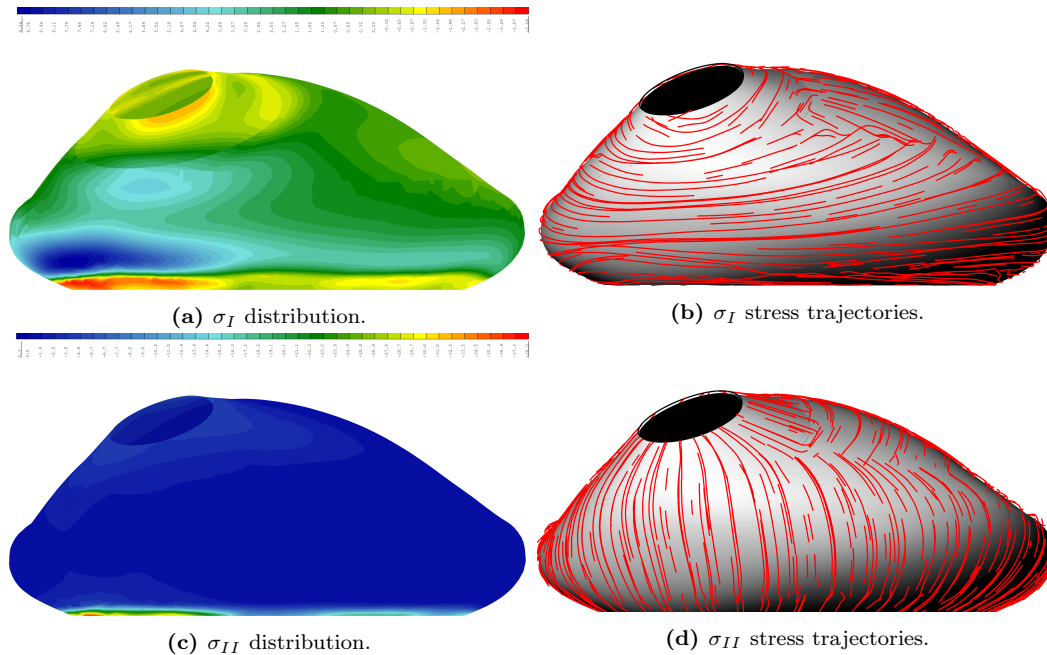
two geometries presented in this chapter.

(a) σ_I distribution.

(b) σ_I stress trajectories.

(c) σ_{II} distribution.

(d) σ_{II} stress trajectories.

Figure 13.19: Principal stresses compared to the corrosponding stress trajectories.

The principal stresses are seen to act in the same directions as for the structure in the ring beam approach but the values, except for the tension stress directly under the ring beam, are reduced.

13.2.3   Summary

It can be seen from the previous investigation that the bending moments can be significantly reduced if the geometry is optimised towards the given load. The maximum value of the first principal bending moment is in this investigation reduced from 190,8 kNm/m to 37,7 kNm/m. The maximum second principal bending moment is reduced by about 67 %. The minimum principal bending moments and the principal membrane forces however are not reduced significantly and actually increased in the case of the second principal membrane force.

The negative principal bending moment in the area underneath the ring load is not reduced and the value of -204,9 kNm/m is too large to be efficiently obtained by a reinforced concrete shell structure.

The optimisation of the geometry may result in the reduction of bending moments as wished but will not ensure a global reduction of all bending moments. In this case the bending moment in the local y-direction, which was also the largest of the moments for the structure before the geometry optimisation was implemented, is not reduced. As for part 2 it is observed that the lower part of pebble B should also have been the subject of a geometric optimisation in order to reduce the bending moments for the entire structure.

Finally for illustrative purposes the principal stress trajectories have for the two geometries are presented. The principal stress trajectories have been generated by use of the Principal Stress Trajectory Tool introduced in section 7. The trajectories shown are for the centre plane of the cross sections.
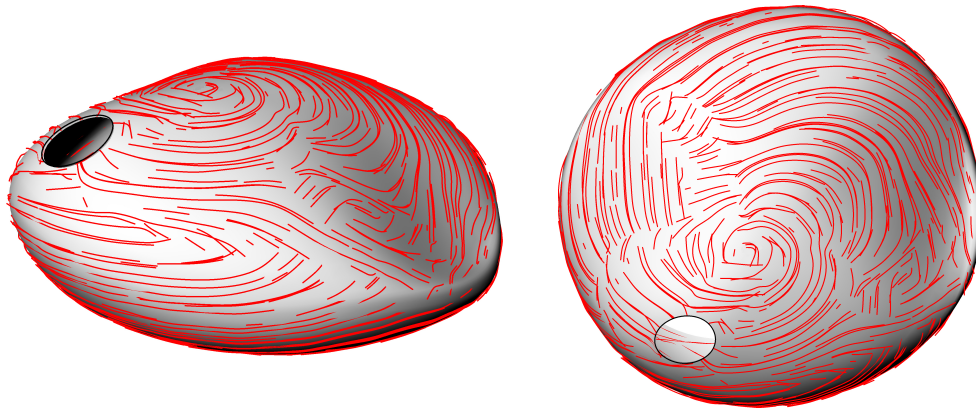

Figure 13.20: σ_I trajectories overview.
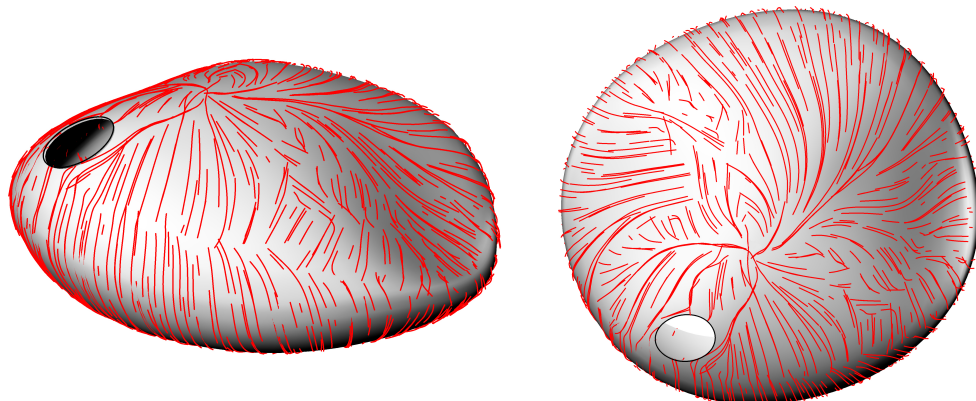
Figure 13.21: σ_{II} trajectories overview.

Figure 13.20 and figure 13.21 for the ring beam approach show that the first principal stresses, the numerically largest stresses, act circumferentially on the shell structure while the second principal stresses mainly act in the local y-direction. From this observation it can be expected that the cross section underneath the load ring will need a significantly large amount of reinforcement to cope with the large horisontal tension stresses found in this area.

Figure 13.22 and figure 13.23 gives an overview of the principal stress trajectories for the optimised conical geometry - again for the centre plane of the structure.
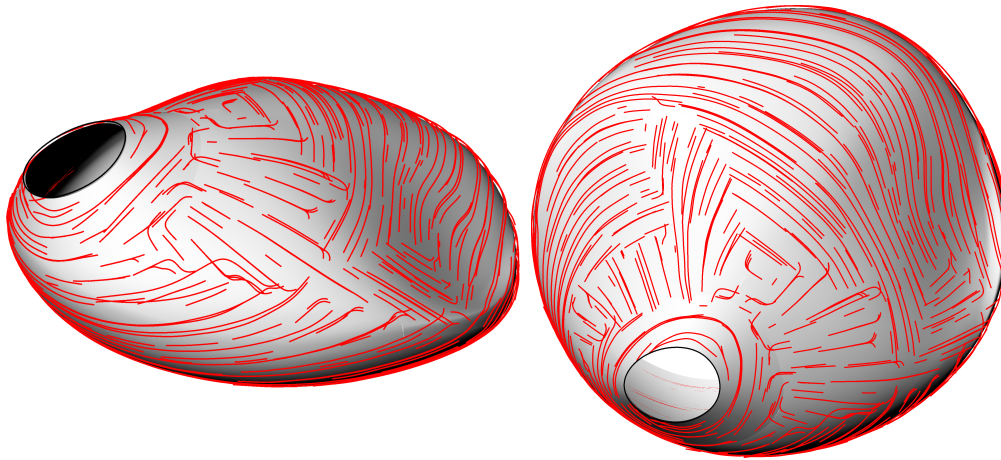
Figure 13.22: σ_I trajectories overview.
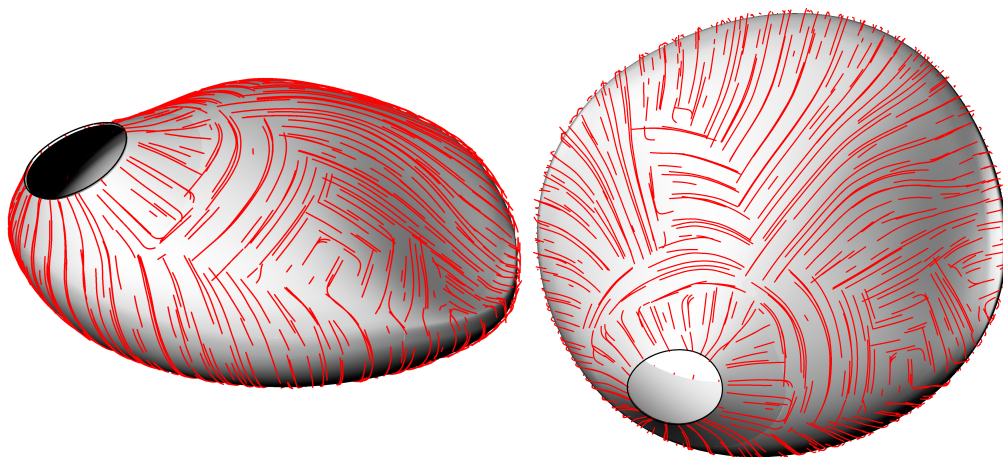
Figure 13.23: σ_{II} trajectories overview.

Again the largest compression stresses act in a circumferential direction but interestingly it is seen that the principal stress trajectories change direction compared to the geometry from the ring beam approach in the area around the introduced conical shape. The discontinuities around the edge of the introduced optimisation are most likely responsible for the change of behaviour for the principal stress trajectories.

CHAPTER 14

Conclusion

This chapter concludes whether or not the structural optimisation of pebble B has been successful and sums up the observations done throughout the report. Recommendations for future work and studies are given in section 14.1.

In chapter 3.2 the membrane theory of shells of revolution is presented. The theory is used to verify the finite element software, which is the base of further studies in this report. It is concluded that Robot and Sofistik has acceptable deviances compared to analytical results and these are chosen for the remaining quantitative finite element analyses in the project. The simple finite element plug-in Scan&Solve calculates non-conservative deflections and is only used for intuitive investigations of the deformation behaviour of simple shell structures.

Through a qualitative study of simple paper models, and similar finite element models in Scan&Solve, a basic understanding of double curved shell structures is achieved in chapter 4. It is concluded that facetted and smooth shell structures are comparable in terms of deformations. Furthermore, chapter 4 concludes that the deformation behaviour of the paper models compared to the computational models are similar and that the base geometry of axisymmetrical shell structures is of little importance in regards to deformations in comparison with the consequences of planar and concave areas in the upper part of the shell structures.

Chapter 5 presents a quantitative study of nine different axisymmetrical shell structures exposed to a vertical uniformly distributed load and a horizontal uniformly distributed load respectively. The nine geometries are chosen to represent the possible alterations of the pebble B geometry. Finally a detailed study of 22 variations of the upper curvature of a hemisphere is carried out. The chapter concludes that planar and concave areas perpendicular to the load direction are unfavourable regarding deformations but for different reasons: The planar areas experience large deformations because of large bending moments in the centre of the area while the concave areas experience the large deformation due to the curvature discontinuity at the edge of the areas. As in chapter 4 it is concluded that consequences of altering the base geometry of the shell structures are smaller than for the alteration of the geometry of the upper part of the structures.

Various parametric visualisation tools are presented in chapter 7. The tools are developed to assist the intuitive understanding of the curvatures, section forces and stresses in shell structures. Additionally, a tool that applies cross sections to a given shell geometry through a linear-elastic reinforced concrete calculation is developed.
All tools except for the Geometry Analysis Tool are based on data from linear analyses in Sofistik.

The original geometry of pebble B designed by Henning Larsen Architects is optimised geometrically in chapter 8 in accordance with the observations done in chapter 4 and 5. A parametric model where the geometry of the upper part of pebble B is the subject of the geometry alteration is developed. The chapter proposes an optimised geometry where the upper part is convex, however kept within the aesthetic frame of the proposal from Henning Larsen Architects.

Based on the observations done in chapter 9 a method is developed to discover planar areas on pebble B. Combining this method with a Gaussian curvature analysis it is possible to perform a geometrical analysis of the original and the optimised geometry. For the original geometry two large planar areas are discovered on the upper part. Furthermore, large curvature discontinuities are seen around the concave areas and on the *belt* of the geometry. Such areas will affect the overall efficiency of the structure. For the optimised geometry four planar areas are seen on the upper part. However, the discontinuity in curvature is clearly reduced for the upper part and the observations indicate that a more efficient shell has been generated.

A structural analysis of the original geometry and the optimised geometry is presented in chapter 12. A linear analysis is the base of the dimensioning process where cross sections are assigned in ultimate limit state. The maximum deflection of a thin shell structure with large spans as pebble B is found to be the dimensioning factor. The dimensions of the cross sections that ensure a maximum deflection below the target of 30 mm through a non-linear analysis in serviceability limit state confirms this assumption. The material consumption of the two different geometries of pebble B is the matter of comparison and it is seen that a reduction of 35,4% and 44,6% in the concrete and reinforcement steel volumes respectively is achieved by implementing the changes in the upper part of the geometry as presented in chapter 8. It is also concluded that the division of the two shell structures, into areas of different cross sections, is simpler for the optimised geometry, hence the buildability of the design is assumed to have increased.

Chapter 13 investigates the necessary dimensions of two proposed designs of a secondary frame structure to obtain the self-weight and imposed load from pebble A. The design restrictions ruled out the use of columns in section 6.2 and a structured kept in the perimeter of the shell surface is preferred. The investigation concludes that the implementation of frame structures to carry the upper pebble is not feasible given the sizes of the necessary cross sections to ensure a deflection below 30 mm. The necessary moments of inertia for the

proposed structures were calculated to be $25 \cdot 10^9 mm^4$ and $45 \cdot 10^9 mm^4$ respectively.

Finally chapter 13.2 applies the self-weight and imposed load from pebble A directly to the shell structure of pebble B through a ring load. Before doing so a study of ring loads on shell structures is carried out investigating eight different load setups. The load setups studied show that the angle between the applied load and the loaded area on the shell surfaces is of great importance in regards to the bending moments but also that by applying the load through a stiffened ring beam reduces the bending moments locally.

However, the chapter concludes that more than a local optimisation of the application of the load or the geometry is needed since the both structures investigated experience a very large bending moment by the supporting line below the ring load.

14.1 Further Studies

This section sums up issues for further study. Although several conclusions are made they do not indicate that research in these fields is final.

An obvious future task will be a structural optimisation of the base of pebble B by a parametric approach. Furthermore, a more comprehensive structural analysis of pebble B, taking additional design requirements such as seismic considerations, exposure to fire and robustness into account, is needed.

An extension of the qualitative study of shell structures with parameters such as: boundary conditions, different geometrical shapes and asymmetrical loadings could be carried out. Hereby, one could possibly develop more generic geometric analysis tools for predicting the structural behaviour of shell structures.

Finally a further development of the Principal Stress Trajectory tool in order to accommodate a structural model with flexural reinforcement placed in accordance to the trajectories could be an interesting addition to the tools developed in this project.

Throughout this project the parametric approach has been applied to both simple and very complex model generations which is one of the most important aspects of the parametric approach. The features can be applied to simple tasks as in Part 1 but also more complex tasks as in Part 2 and 3 of the project. Both minor and major alterations of design are applicable through the parametric approach and the interoperability of the tools simplifies visualisations various testings in the conceptual phase of a design process. Especially the automatisation of processes and the interoperability of software indicates that the parametric approach could be one of most powerful tools to reducing the gap between architects and engineers.

Bibliography

[1] http://www.rhino3d.com. Website visited 20.07.2012.

[2] http://www.grasshopper3d.com. Website visited 20.07.2012.

[3] http://ssi.wikidot.com. Website visited 20.07.2012.

[4] http://usa.autodesk.com/robot-structural-analysis-professional. Website visited 20.07.2012.

[5] http://www.scan-and-solve.com. Website visited 20.07.2012.

[6] Eduard Ventsel and Theodor Krauthammer. *Thin Plates and Shells - Theory, Analysis and Applications.*. Marcel Dekker Inc, 2001.

[7] Jørgen Juncher Jensen and Marie Lützen. *Introduction to Analysis and Design of Plate Panels.* DTU, 2006.

[8] Henrik Almegaard. *Skalkonstruktioner. Metoder til afklaring af sammenhænge mellem form, stabilitet, stivhed og understøtninger.* PhD Thesis, By og Byg - Statens Bygge-forskningsinstitut, 2003.

[9] Anne Bagger. *Plate shell structures of glass. Studies leading to guidelines for structural design.* PhD Thesis, Department of Civil Engineering, Technical University of Denmark, 2010.

[10] *Teknisk Ståbi.* 20. udgave, Nyt Teknisk Forlag, 2009.

[11] Stephen P. Timoshenko and S. Woinowsky-Krieger. *Theory of Plates and Shells.* McGraw-Hill Book Company, 1959.

[12] W.H. Mosley, J.H. Bungey and R. Hulse. *Reinforced Concrete Design.* 5. edition, Macmillan Press, 1999.

[13] Jasbir S. Arora. *Guide to Structural Optimization.* American Society of Civil Engineers, 1997.

[14] Eurocode 0. EN 1990: Basis of structural design.

[15] Eurocode 1. EN 1991: Actions on structures.

[16] Eurocode 2. EN 1992: Design of concrete structures.

[17] N. G. R. Iyengar. *Structural Design Optimization.* Oscar Publications, Delhi, India, 1997.

[18] U.S. Army Corps of Engineers. *Standard Practice For Shotcrete.* Department of the Army, Washington, DC, 1993.

[19] http://courses.umass.edu/latour/Italy/Pantheon/index.htm. Website visited 20.07.2012.

[20] http://www.romasparita.eu. Website visited 20.07.2012.

[21] http://en.wikipedia.org/wiki/File:Auditorio$_d$e$_T$eneri$f$e$_P$ano.jpg.$Websitevisited$20.07.2012.

[22] http://www.bubbledeck.com/ Website visited 20.07.2012.

[23] Kenneth Leet *Reinforced Concrete Design.* 2. edition, McGraw-Hill, Inc., 1991.

[24] C.B.Wilby *Concrete Dome Roofs.* Longman Scientific Technical, 1993.

[25] http://imageobjecttext.com/2012/04/22/collecting-the-set/ Website visited 20.07.2012.

[26] http://www.autoatlanta.com/ Website visited 20.07.2012.